CIRAD

CTBA

Research into non-destructive compression crack detection methods for wood structures

Final Report

Revised version, dated 21 February 2008

Table of Contents

1. Introduction

This document constitutes the final report of study no. 06/084/MQ/FIN, the purpose of which is to identify non-destructive testing methods for crack detection in structures made of rough sawn wood, excluding plywood. These structures, and in particular spars, are structural components of wood-built light aircraft, and especially acrobatic aircraft such as the CAP10. This aircraft constitutes the reference of the study because of the availability of used wings with compression cracks (compression failures). Furthermore, this aircraft is of importance compared with aircraft amateur construction because it was built in many units and the CAP 10 fleet is significant.

The term compression crack refers to a structural anomaly existing in the form of a fine fracture perpendicular to the wood fibres. A crack results from significant deformation followed by compression failure of the wood cells. Crack formation is accompanied by several transverse fissures appearing in the material.

Irrespective of the type of aircraft, all aircraft are inspected regularly. These inspections are mainly visual and external. Other checks such as "major inspections" or "general overhauls" are more in-depth and require dismantling of some aircraft components. The inspection however remains visual and subjective. Moreover, some parts of the aircraft are more difficult to access and hence more difficult to inspect.

The detection methods used must enable a thorough inspection either during initial construction, or during airworthiness testing procedures for all aircraft manufactured using wood, including those produced commercially as well as those built by amateurs. The aim of this feasibility study is to propose one or more methods that are effective, non-subjective and as economic as possible.

The study was undertaken in four phases:

- Phase 1: Collection of existing data.

    o Definition of the problem of non-destructive testing and development of a compression crack typology as observed on the CAP10.

    o Analysis of specialized published articles related to compression cracks in wood.

    o Inventory of inspection methods applicable to crack detection.

- Phase 2: Selection of inspection methods and techniques for manufacturing test specimens.

    o Elimination of inspection methods not applicable to crack detection in wood. The inspection methods retained were then analysed by laboratories and partner organisations.

    o Manufacture of test specimens. This involved causing deliberate damage to wood specimens to "artificially" create compression cracks representative of the cracks actually observed on the CAP10. From these damaged specimens, test specimens, fully

representative of an actual spar chord, were developed for testing inspection methods.

–   Phase 3: Tests for validating the selected inspection methods

o   Testing the inspection methods on test specimens. These tests were used to study both the fundamental research aspects as well as industrial development feasibility.

o   Testing the methods on a CAP10 spar and wing element. These tests enabled the feasibility aspect to be examined on two actual cases.

–   Phase 4: Analysis of the validation tests and recommendations.

o   Evaluation of the effectiveness of each inspection method in addressing the problem.

o   Recommendations regarding the most effective methods for developing an industrial inspection procedure. Financial aspects and development time were both taken into consideration.

CAP 10 (Source: http://rafaero.free.fr/cap10.html).
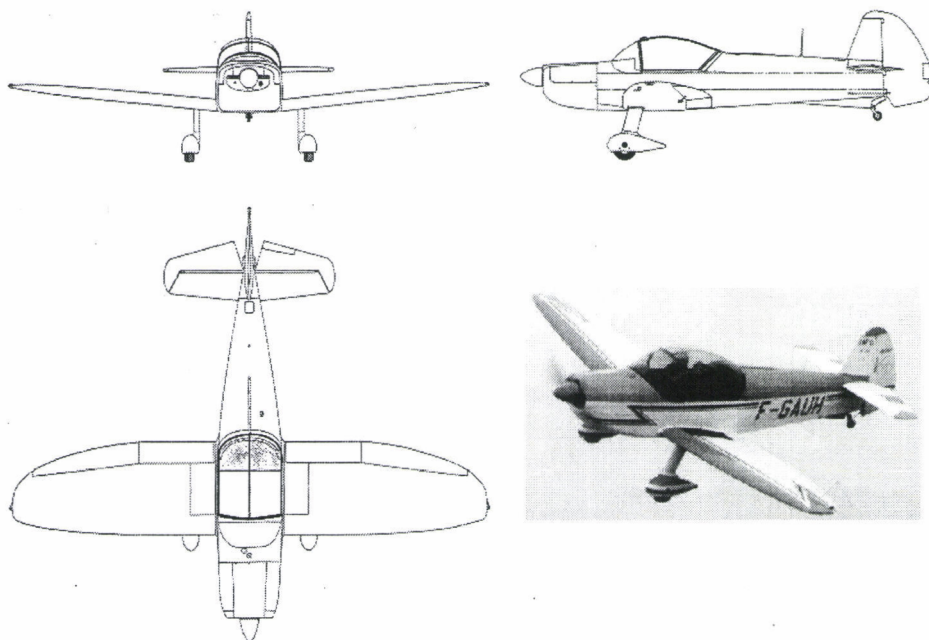
2. Crack typology in light aircraft spars

2.1.   Wings and spars
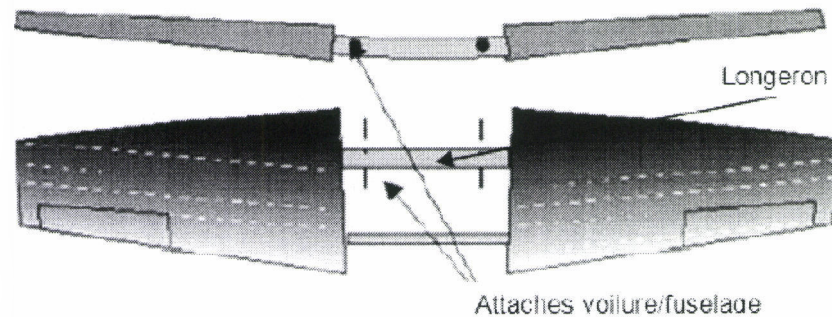
Fig.1: Diagram of a single-block wing (as in the CAP10).

The wings are an airframe component (Fig.1); they support the aircraft's weight by generating a force also referred to as lift. In a monoplane, there are two wings, with each wing having one (or more) spars attached to the fuselage (one main spar with a secondary spar in the case of the CAP10). The ribs support the top skin or upper surface and the bottom skin or lower surface. The front and back edges of the wing are known as the leading edge and the trailing edge.
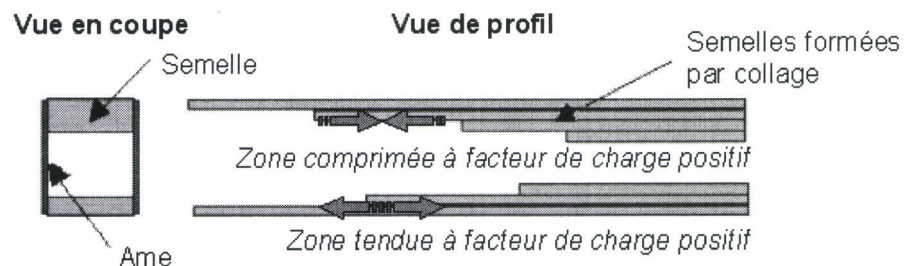
Fig.2: Principles of spar construction taking up only the bending stresses (as in the CAP10).

In the specific case of the CAP10, the spar consists of two chords in Sitka Spruce (*Picea sitchensis*) and two webs in birch plywood (*Betula pendula*) 5 mm *thick* (Fig.2 *and* Fig.3- a, b). The chords are obtained by lengthwise (mitre) joints, transverse joints (see Fig.3 - b) and by bonding 12mm thick planks - 5 for the upper chord (upper surface) and 3 for the lower chord (lower surface). The cross-section of the chords is not constant along the length (Fig.2).
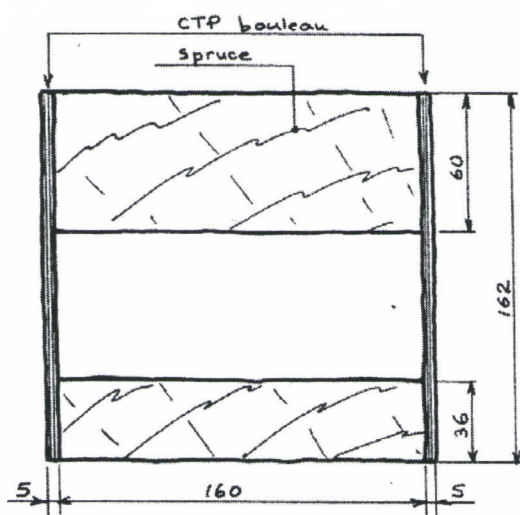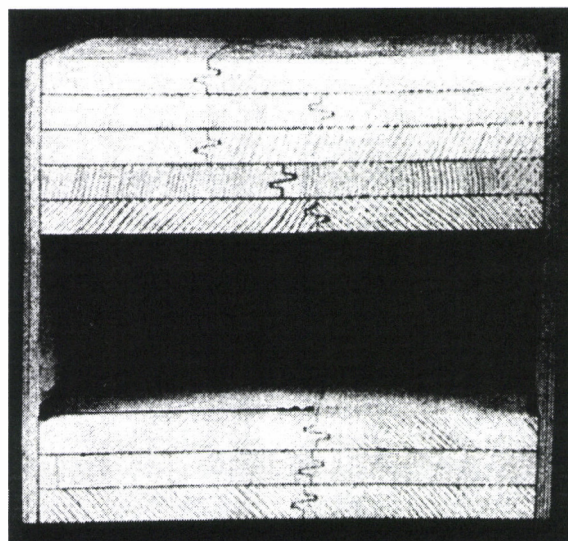
(a)   (b)

Fig.3: Sketch (a) and photograph (b) of a section of a CAP10 spar (Klinka, 1988).

2.2.   Mechanical stress exerted on the spar

Spars as defined in Fig.2 absorb only bending stresses (in contrast with other types, which take up both bending and torsional stresses as in the case of the DR400 for example). (Source: www.aviation-fr.info).

It is generally considered that, when an in-plane bending moment is applied to a spar, the chords experience both tensile and compressive stress (Fig. 4), and the shear stress is taken up by the two plywood webs subjected to shearing (Klinka, 1988; Vallat, 1945).
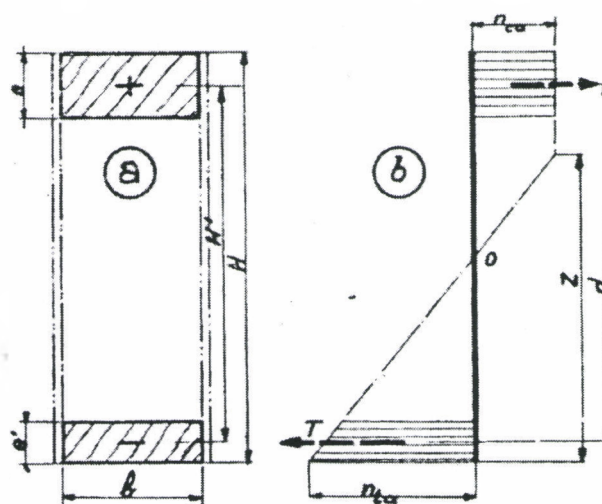
Fig. 4: Distribution of normal stress in the section of a spar (a) cross-section of the spar, (b) associated distribution (Vallat, 1945).

In the case of the CAP10, the load factor limit of the spar is +6g and -4.5g (the total permitted weight in service is 760 kg). This asymmetry in the positive/negative admissible load factor explains the difference in thickness of the spar chords on the upper/lower surface. At limit load, the bending moment is

24000 N.m (the limit moment is 36000 N.m. Klinka, 1988). The longitudinal stresses, which are functions of the bending moment are maximum at the wing root (Fig. 5).
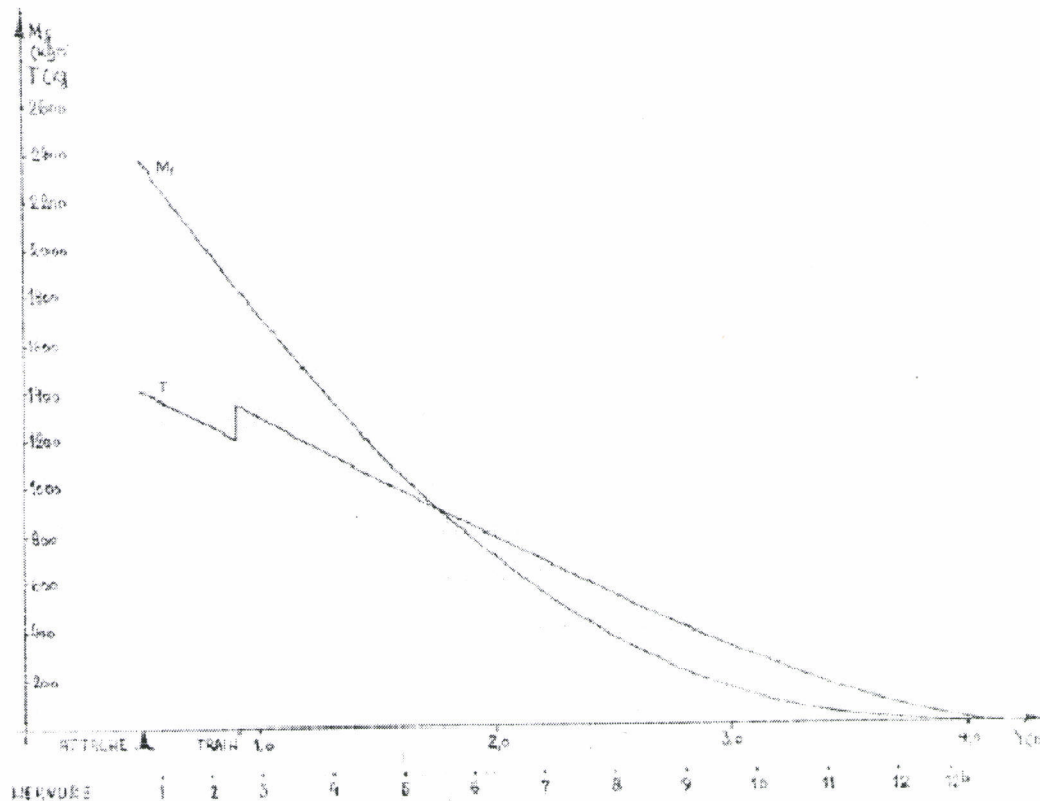
Fig. 5: Shearing stress and bending moment in a fixed-free beam.

2.3.   Definition of a crack

Fig. 6: Compression crack visible on the wood surface (Bruce H, 2000).

The term compression crack refers to a structural anomaly existing in the form of a narrow fracture perpendicular to the wood fibre, whose microscopic appearance results from a compression failure combined with significant distortion of the cells accompanied by several transverse fissures in the walls. This results in the appearance of ripples on the surface of the material (Fig. 6) in a direction that is perpendicular to the fibre direction (compressive stress oriented along the fibres). (Bruce H, 2000).

It generates in most cases a very low ultimate value of longitudinal tensile strength. It is also referred to as compression failure and originates from a strain in the fibres stemming from an excessive compressive stress, beyond the tensile strength, along the grain either under pure compression or under flexure. Local buckling (micro-buckling) of the fibres and other elements of the wood takes

place. The compression cracks indicate a permanent failure of the material caused by an excessive load or impact in the direction of the wood fibres.

2.4. Observation of cracks in wings under repair

Examinations were carried out on CAP10 spars. These aircraft had been sent for repair at "Air Menuiserie" – a Company located close to the town of Bernay (27230 Thiberville). These observations help to define the inspection problem stated below. The photographs that illustrate the problem can be found in later pages for better readability; they constitute the fault typological classification.

- Inspection is first and foremost necessary to ensure airworthiness testing of all aircraft built in wood, for commercially-produced aircraft as well as those made by amateurs.
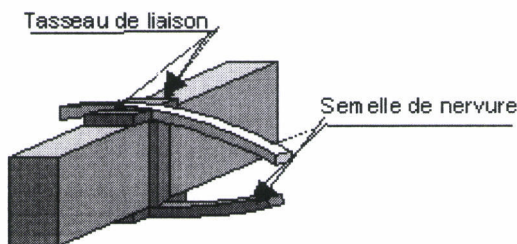
Fig.7: Example of a joint between the ribs and the spar.
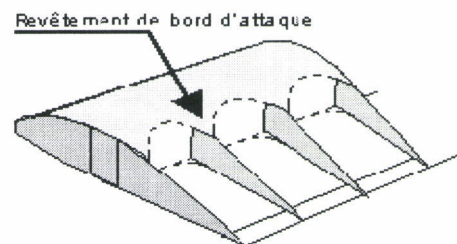
Fig. 8: Example of a joint between the ribs and the wing skin.

- The inspection of in-service aircraft implies the promotion of inspection methods capable of surveying structural elements without direct access to them (like the existence of a skin element of Okoumé plywood 5mm thick connected to the ribs as in Fig.7 and Fig. 8). It is advisable to take into consideration direct access testing of the structure in case indirect access testing is not possible for technical or financial reasons.

- The aim of this inspection is firstly to detect the presence of cracks in spars of aircraft of type CAP10: do cracks exist? Where are they located? The size of the crack forms component of the secondary data (surface area as well as depth).

Fig. 9: Crack appearance zones.

- Cracks can be found on both the upper and lower surfaces of the wing. There are specific areas where these cracks may form. These areas are found very close to the wing / fuselage joint and extend up to the landing gear joint: i.e. approximately 0.5 m (Fig. 9). These zones correspond to the maximum bending moment. It must be possible however to inspect the whole spar.

- Another type of damage has been observed showing incipient tensile cracks. This type of damage is found in the same zones as the cracks. During aerobatics, alternating between positive and negative load factors leads to the observation of tensile and compression failure on the same area.

Wing / fuselage attachment detail.

Rear view.

CAP232 (Photo CIRAD / FCBA).
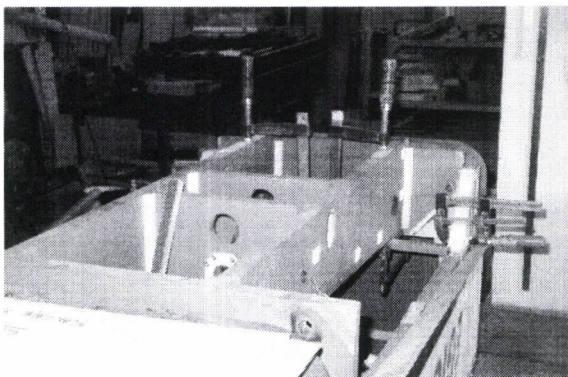
Wing / fuselage attachment detail.

Front view.

CAP232 (Photo CIRAD / FCBA).
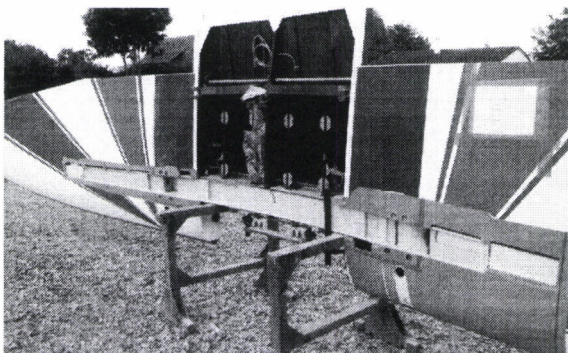
Wing under repair.

Plywood skin cut.

Spar visible, top skin view.

CAP10 (Photo CIRAD / FCBA).
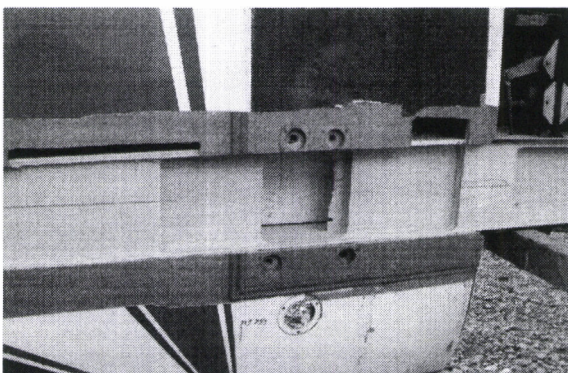
Spar detail, top skin view.

The parts removed correspond to the damage areas. A section is then bonded in to recreate a fault free chord.

CAP10 (Photo CIRAD / FCBA).
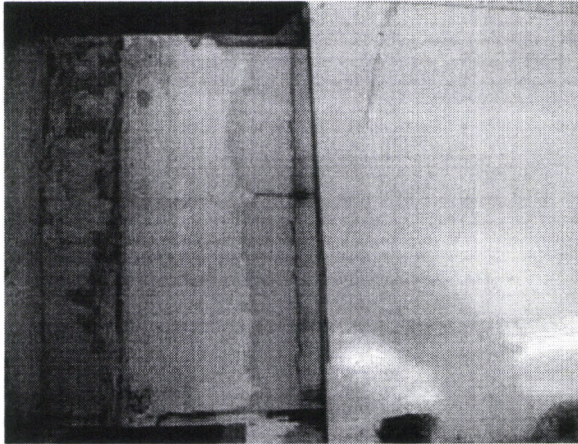
Crack detail on a spar.

Cracking is visible since blackened by impurities. This cracking is caused by compression failure followed by load reversal and enlargement of the existing damage.

Traces of moisture were also detected.

CAP231 (Photo Air Menuiserie).
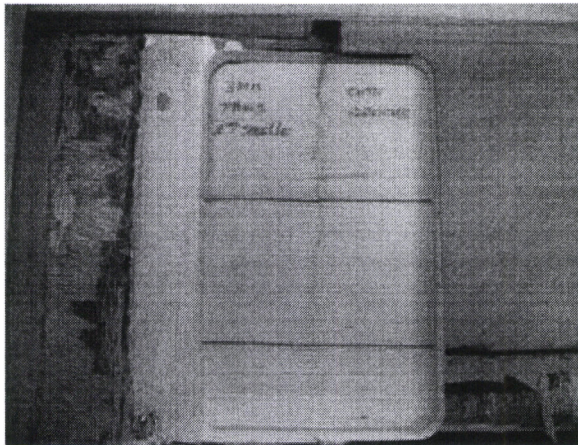
Same detail after having removed a component of the spar thickness (depth approximately 12 mm). The width of the crack is of the order of 0.1 mm at the start of compression failure (up to 1 mm after cracking).

CAP231 (Photo Air Menuiserie).
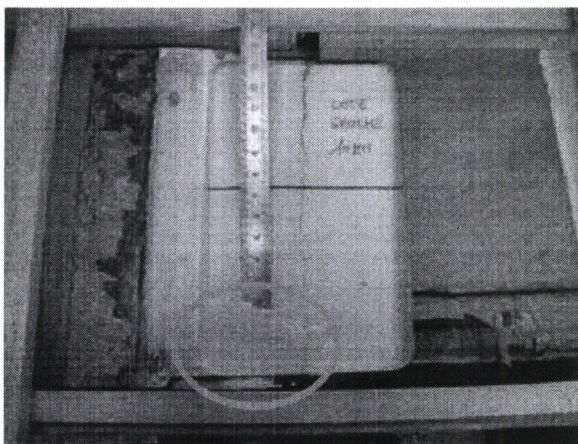
Another view of the crack with tensile failure on the left side (circled in red).

CAP231 (Photo Air Menuiserie).

3. Characteristics and detectability of cracks in wood structures

3.1. General information on wood

Wood is a solid, cellular, organic and natural body. It is a composite material made of a group of chemical elements, mainly cellulose, hemicelluloses and lignin. Wood is strongly anisotropic on account of the elongated shape of its cells and the oriented structure of its cell walls (Racher, 1996). The mechanical behaviour of wood is highly conditional on its physical state; the main physical factors being its density, moisture content, temperature and duration of application of stresses (Guitard, 1997; Racher, 1996).

3.2. Mechanical behaviour under traction-compression
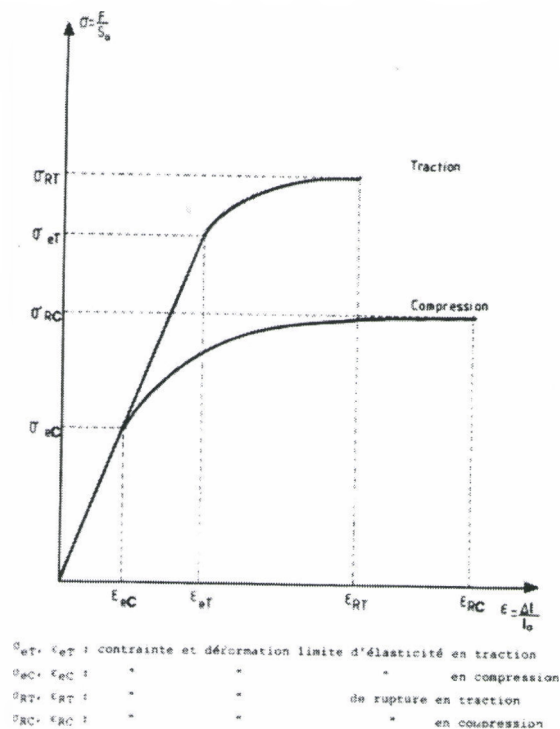
Fig. 10: Schematic figure of stress-strain (traction and compression) diagram for solid wood in the longitudinal direction (Guitard, 1997).

The difference in the mechanical behaviour of wood under traction and compression in the longitudinal direction is illustrated in Fig. 10. The tensile curve shows an approximately linear zone referred to as the elastic zone followed by a non-linear zone referred to as plastic zone, which leads to tensile failure. The tensile failure of wood accounts for its "brittle" nature. The compression curve shows the same type of pattern as the tensile curve but with the plastic zone being more marked. The compression failure of the material accounts for its "ductile" nature. (Guitard, 1997). The tensile failure limit is greater than the compression

failure limit; with the ratio of tensile to compression being approximately 2 (Pluvinage, 1992).
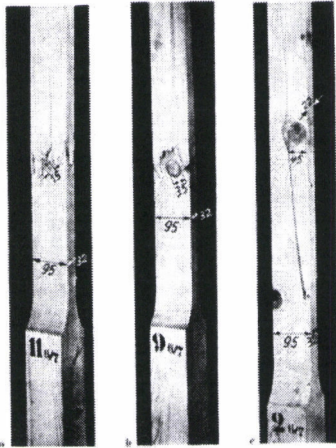
Fig. 11: Tensile failure stress pattern (Kollmann, 1967).
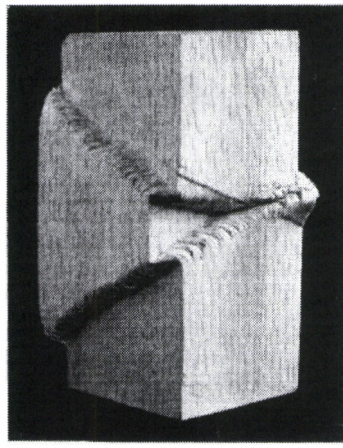
Fig.12: Compression failure stress pattern (Kollmann, 1967).
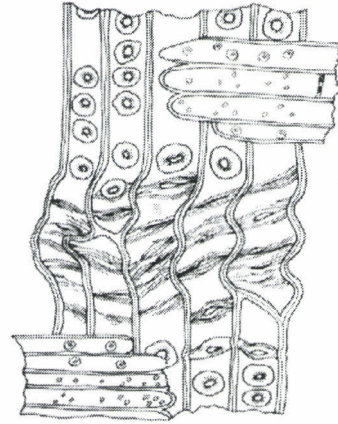
Fig.13: Sketch showing sections of compression failure (Kollmann, 1967).

The analysis of failure facies shows clear differences between the tensile and compression failure modes (Guitard, 1997; Pluvinage, 1992). Under traction, fibre breakage occurs (Fig. 11); while under compression fibre buckling takes place (Fig.12 and Fig.13). (Guitard, 1997; Kollmann 1967).

3.3.   Mechanical behaviour in flexure
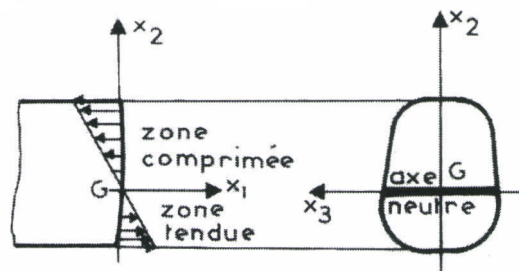
Fig. 14: Distribution of normal stresses for a negative bending moment (Kerguignas, 1977).

Under pure plane bending, the normal stresses – collinear along the wood grain – are linearly distributed in the cross section, and reach the maximum for points that are furthest away from the bending axis, the neutral stress axis (Fig. 14). (Kerguignas, 1977). Stress distribution in Fig. 14 is valid in the material's elastic range. This distribution displays a compression stress gradient on the upper surface and tensile stress gradient on the lower surface of the beam in flexure. The behavioural differences observed under traction and compression then determine the behaviour of the material in flexure (Kollmann, 1967).
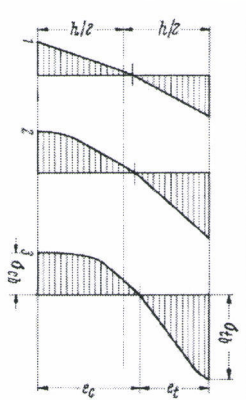
Fig. 15: Normal bending stress pattern (Kollmann, 1968).
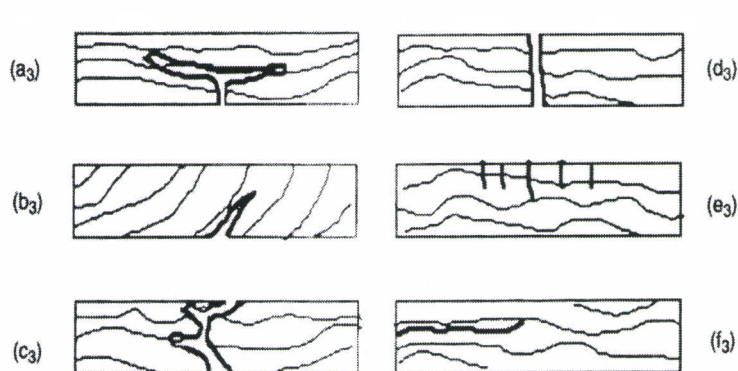
Fig. 16: Morphology of bending failure facies. Brittle failure in tension (d_3), compression failure (e_3), shearing failure of axial plans (f_3), multi modal failure (a_3, b_3, c_3). (Pluvinage, 1992).

Fig. 15 shows the pattern of normal stresses when they increase (during a bend test). The plastic zone is first attained in the compressed zone; this leads to material damage in this zone. The end of the bend test resulted in damage to the material under traction. (Kollmann, 1968; Pluvinage, 1992).

It is important to mention that the morphological analysis of wood failure reveals several failure modes under compression, traction as well as in flexure, depending on the type of stresses and strains, the existence of defects or planes of weakness in the material (Pluvinage, 1992). In the case of flexure, the different facies are given in Fig. 16. These different facies obtained show that it is very difficult to artificially create a crack by bending a test specimen (the e_3 case is then the only desired case amongst the 6 possible cases).

3.4. Scientific results obtained on compression failure

Characterisation at the macro-structural level

An analysis of failure profiles obtained through compression tests along the grain of conifers, deciduous trees and standard specimens made from wood has been undertaken by Bariska (1985). It was noted in particular that failure development depended not only on the main zone of weakness but also on the sequencing of loads applied to the specimen. The manner in which these loads are applied is also a dominant factor.

It was found that under axial compression and in the case of standard specimens (Fig. 17), shear cracks were generated along the axial structural elements and by analogy between the growth rings for solid wood. Mechanically unstable lamellae are thus formed and these tend to buckle. This deformation mechanism is similar between standard specimens and solid wood specimens.

Fig. 17: Failure pattern under axial compression of a standard specimen (Bariska et al., 1985).

Ellis (2002) has characterized the longitudinal compressive behaviour of five species of wood (*Fraxinus latifolia; Shorea spp.; Pseudotsuga menziesii; Thuja plicata; Populus tremuloides*). This study showed that under longitudinal compression, failure occurred by fracturing the material plane at the interfaces between successive cell layers (growth rings). This observation is in agreement with the results of Bariska (1985).

Characterisation at structural level

The initiation and propagation of compression failure in pine wood were studied at microscopic level by Choi (1996). The strain cross sections of the wood appeared as non-uniform but closely linked to its morphology. The zone where stress was concentrated lay mostly around the radii. These zones seemed to expand based on the size and the arrangement of radii.

Characterisation at micro-structural level

The study of compression failure at micro-structural level was mainly carried out by Gong (2004). This study showed that compression damage in wood first appears in the form of wrinkles or buckling of cells. A wrinkle corresponds to a permanent micro-structural change of the cell wall and results in a re-orientation of the micro-fibrils in the middle lamella of the wall S2.

It is important to mention the works of Bodner (1997) on the initiation and propagation phenomena of *tensile failure* along the wood grain under compression for spruce.
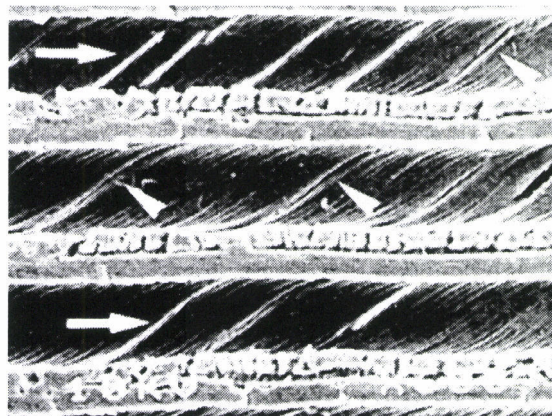
Fig. 18: Compression wood tracheids after longitudinal tensile test. The arrows indicate the lateral dislocations between micro-fibrils. (Bodner et al., 1997).

Bodner (1997) particularly mentions that micro-fibrils tend to split up laterally before breaking (Fig.18), and also, that the extent of lateral dislocation due to matrix degradation before micro-fibril failure increases with the increase of the micro-fibril angle. (Bodner *et al.*, 1997).

Damage under cyclic tests
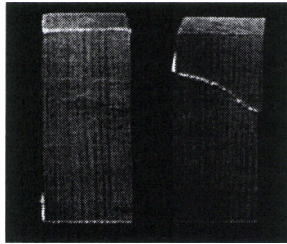
(1)   (2)

Fig. 19: Failure patterns obtained through compression cyclic tests, diffused compression failure (1), localised compression failure (2). (Clorius et al., 2000).

Clorius (2000) carried out fatigue tests on wood specimens subjected to load and off-load cycles under longitudinal compression. Small specimens of spruce free from defects were subjected to cyclic tests of square loads corresponding to 80% of the breaking force estimated from static tests. Four frequencies ranging from 0.01 hertz to 10 hertz were used. The analysis of failure sections showed (1) diffused compression failure or (2) compression failure that is localised and materialised in the form of a penetrating ripple (Fig. 19). The patterns observed expanded in the very last loading and off-loading cycles. The proportion of diffused failure increases when frequency decreases and when the moisture content increases. The results also show that the time to failure decreases when the frequency increases. (Clorius *et al.*, 2000).

Effect of compression damage on mechanical strength

Compression damage does not significantly affect the compressive strength. Fibre buckling, which distinguishes compression failure can however seriously affect tensile strength and consequently the bending strength of wood. (USDA, 1961).

Static bending strength is in fact greatly affected by compression failure, with an average force reduction of 20% (for spruce wood). The modulus of elasticity is nevertheless very less affected on account of this type of damage (in the dry state). (Sonderegger *et al.*, 2004).

Compression crack detectibility

The fact that the modulus of elasticity is hardly affected by the existence of compression damage explains why this type of defect could not be detected by using acoustic vibration analysis (velocity of propagation or natural frequency of vibration). (Sonderegger *et al.*, 2004). The acoustic vibration analysis techniques will not be investigated in the study.

The detection of this type of defect is however possible through visual examination followed by microscopic examination (USDA, 1961). It is also possible to detect compression failure using X-ray tomography (Sonderegger *et al.*, 2004). This last result highlights the importance of the X-ray technique for the detection of compression cracks. In the following X-rays will be used in transmission and in Compton diffusion.

4. Principal non-destructive testing techniques

4.1.   Definition of non-destructive testing

Non-destructive testing helps to ensure quality and safety of goods and hence safety of people as well.

Many methods are used for detecting internal or surface anomalies, for determining the composition or the structure of materials or even for measuring certain physical properties. The anomalies likely to be detected are:

1) Anomalies introduced during raw material development.

2) Anomalies introduced during the manufacturing process.

3) Anomalies of in-service installations (fatigue, corrosion, cracks).

These methods are used during on-site commissioning, production or maintenance, on materials, assemblies, equipment as well as on installations. (Kouzoubachian, 2006).

4.2.   Visual methods: visual, optical or video endoscope

Visual inspection is the oldest non-destructive test. It is the most commonly used method worldwide since it is the most economical. However, visual inspection undoubtedly does require a certain skill to recognize the type of defects observed. (Hellier, 2001).

The first inspection is normally a visual inspection and this can serve as an indicator for the other inspection methods considered. It can in fact detect emerging defects (fissure, surface cracks, cracks, delamination, etc.) as well as damage and deterioration caused by operating or environmental conditions (corrosion, blue staining, fatigue crack etc.). (Kouzoubachian, 2006).
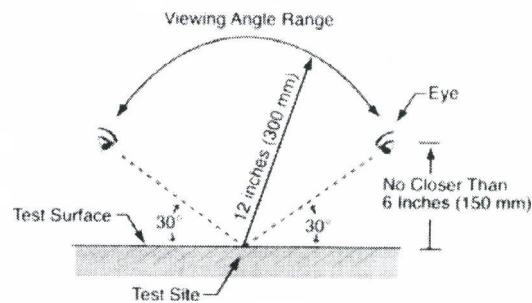
Fig. 20: Orientation of the viewing angle for a standard visual inspection (Hellier, 2001).

During visual inspection, special attention should be paid to the lighting intensity as well as its orientation (Fig. 20). A distinction is made between a direct visual inspection (using a mirror or a lens if required) and an indirect visual inspection (using devices like endoscopes, optical fibres connected to cameras or any other appropriate instrument, Fig. 21 and Fig.22). (Hellier, 2001; Kouzoubachian, 2006).
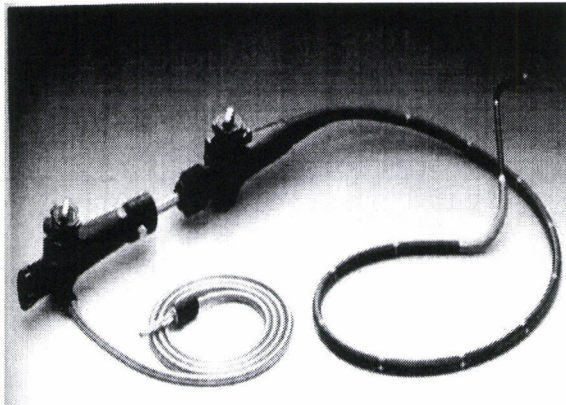
Fig. 21: Optical fibre endoscope (Hellier, 2001).
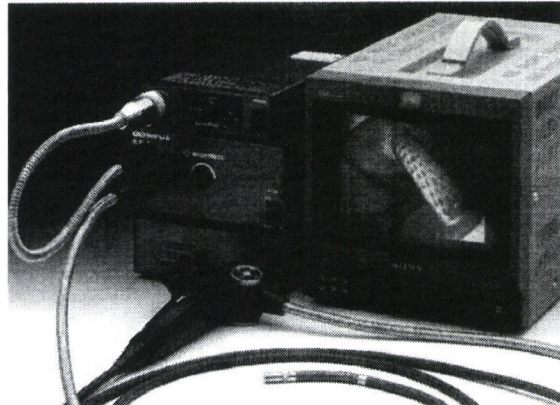
Fig. 22: Video endoscope (Hellier, 2001).

The endoscope is one of the most commonly used devices for inaccessible areas: like in human medicine, it is a rigid or flexible system which helps to inspect internal cavities (Fig. 21). It includes devices which can light up the cavity, generate an image and transport this image (electronically, or using lenses or optical fibres) and finally restore the image to make it observable. (Hellier, 2001).

4.3. Liquid penetrant method

This method supplements visual inspection by making very fine surface defects appear in a coloured or fluorescent contrast. It is commonly used on non porous materials like steel or aluminium. It is based on a relatively simple principle and takes place in several stages. (Kouzoubachian, 2006).
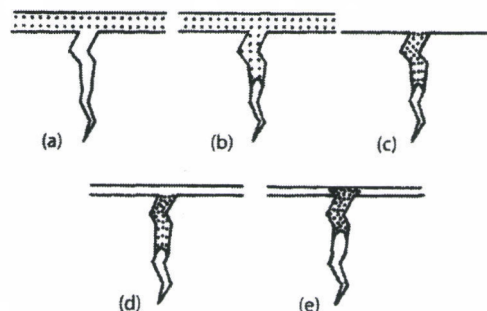
Fig. 23: Schematic diagram of the liquid penetrant method (a) liquid application on a cleaned surface, (b)liquid infiltration into the anomaly, (c)removal of excess liquid, (d) application of the developer, (e) interpretation (Shull, 2002).

The first stage involves carefully cleaning the component to be checked. A coloured or fluorescent liquid known as a "penetrant" is then applied to the surface to be checked (Fig. 23). This will infiltrate into anomalies through capillary action (cracks, fissures, porosities etc.) and hence requires some waiting time before the next stage. Excess penetrant is then removed by appropriate washing. The surface is then covered by a fine layer of developer, which acts like blotting paper to absorb the penetrant contained in the anomalies, generating on the surface a coloured stain larger than the anomaly to assist detection. Thus the developer bleeds out the penetrant. The developer also provides good visual contrast with the penetrant thereby facilitating visual inspection. (Shull, 2002).
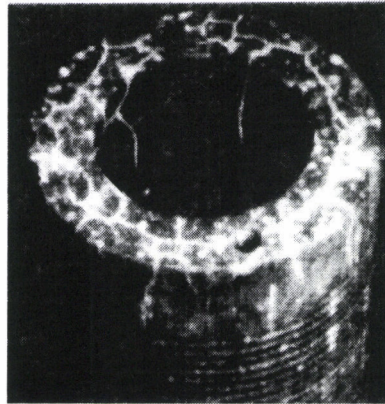
Fig.24: Ceramic material with fissures (Shull, 2002).

These marks are then visible to the naked eye (Fig.24). In certain industries, a fluorescent penetrant is used which is visible under UV lighting. Liquid penetrant testing can be easily introduced into automatic machining lines by dousing or spraying the parts with penetrant, wash and developer contained in successive tanks. The final inspection can even be made using the "intelligent" pattern recognition cameras now available thanks to recent developments in electro-optics and image processing. (Hellier, 2001; Kouzoubachian, 2006; Shull, 2002).

4.4. Permeability testing

Permeability testing is used to detect or locate gas movement from one side of a wall to another. These tests complement other techniques, which mostly highlight defects coming through only on one side, or blind defects located near the surface of the component or deep in the material but which do not enable conclusions to be drawn on defects that traverse the component. Today, there are several test categories in existence: those that detect that there are leaks in the "equipment", those that locate the leak(s) on this same equipment, and those that simultaneously detect and locate the leak(s). (Bray, 1992; Kouzoubachian, 2006).

To perform these tests, leaks need to be created intentionally by applying a differential pressure upstream and downstream in order to provoke gas flow. This difference in pressure can be obtained in most cases through a positive or negative pressure with respect to atmospheric pressure. (Kouzoubachian, 2006). This leak then needs to be detected and/or quantified by one of the methods available (Bray, 1992):

-   Methods "without gas tracer": these use air as test gas (bubble test or through

pressure variation).

– Methods "with gas tracer": these use gases other than air, hence called "gas tracer". These require special precautions. The gases used are: ammonia (a developer paint, yellow in colour, reacts in the presence of ammonia and turns blue at the leak location), halogens or helium.

4.5.   Magnetic method: Magnetic particle testing

This is a technique that detects surface or sub-surface defects, even if blind. However it can be used only for ferromagnetic materials and alloys (iron, steel, cast iron, chromium alloys etc.). (Bray, 1992; Kouzoubachian, 2006). Magnetic particle testing makes use of the fact that any discontinuity existing in a metal component disturbs the path of magnetic field lines in which the component was previously placed. Maximum disturbance will occur when field lines are perpendicular to the anomaly. (Shull, 2002).

One of the following 2 magnetization techniques will be used based on the known orientation of the anomalies as well as the shape of the component (Fig. 25):

- By magnetic flux: this technique produces a magnetization that is longitudinal to the component axis. Here, the transversal anomalies (perpendicular) will disturb the field lines.

- By current: this second technique consists in transmitting a current through the component thereby creating a magnetic field that is transversal to the component axis. This field will be disturbed by longitudinal defects (parallel).

(Hellier, 2001; Kouzoubachian, 2006).
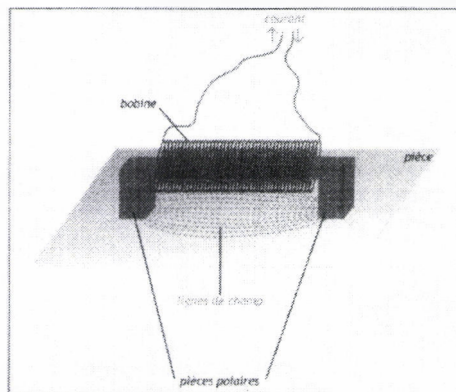
*Schéma de principe de
la technique par flux magnétique.*
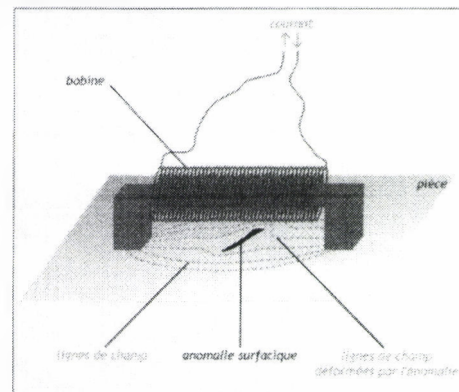
*Déformations du champ
par les anomalies transversales.*
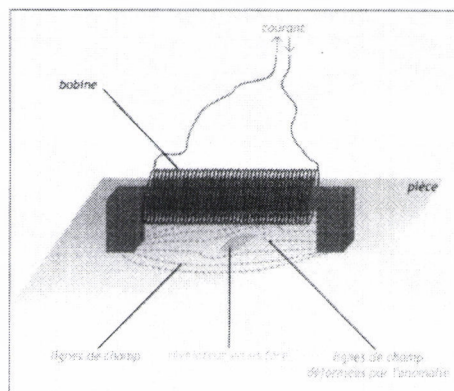
Observation du phénomène en surface.
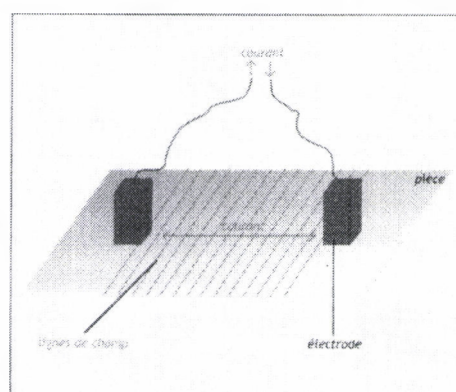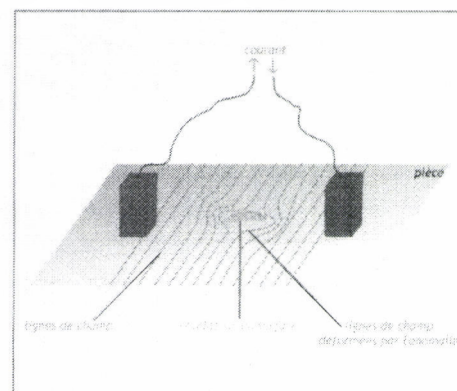
*Schéma de principe
de la technique par courant.*
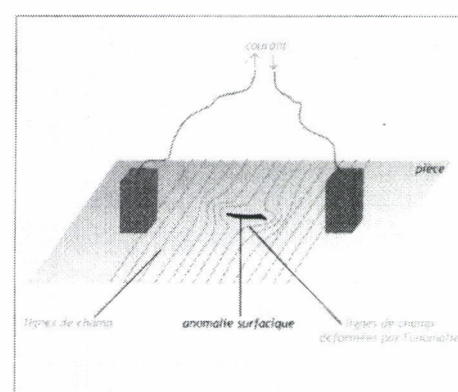
*Déformations du champ
par les défauts longitudinaux.*

Fig. 25: Principles of magnetic particle testing (Kouzoubachian, 2006).

A magnetic powder (dry or in suspension in a neutral liquid) sprayed at the surface will get distributed in a homogeneous manner, if the component is sound. When an anomaly exists in the component near the surface, the orientation of the magnetic flux is locally modified and its intensity at the surface increases. Then at the base of the defect a collection of magnetic particles appears, thereby detecting the defect. The use of direct current for magnetization allows detection up to a depth of a few millimetres. The test can be performed in white light with contrasting backgrounds and coloured tracers (magnetic developers) or in ultraviolet light with fluorescent tracers. (Kouzoubachian, 2006).

4.6. Electromagnetic method: Eddy current

This method can be applied to all materials that conduct electricity. Here, the component is placed in a fluctuating magnetic field. An induced current known as an "Eddy current" runs through the component, with the current distribution depending on component characteristics. This field is measured by a "sensor".
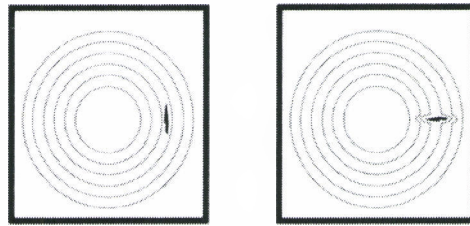
Fig. 26: Discontinuity of Eddy current circulation, (a) discontinuity parallel to the flux, (b) discontinuity perpendicular to the flux (Hellier, 2001).

Any discontinuity in the subject component disturbs the Eddy current circulation leading to a variation in sensor impedance. This variation depends on the orientation of the discontinuity with respect to the current flux (Fig. 26). (Hellier, 2001).
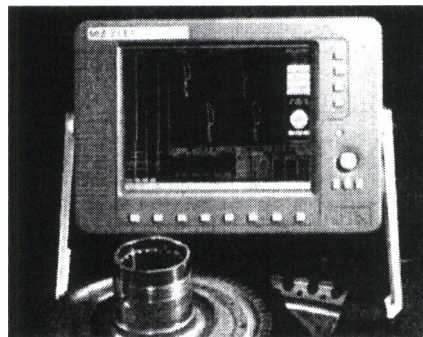
Fig. 27: Inspection of a turbine disk using Eddy current, 4 sensors with 4 Lissajous curves (Shull, 2002).

Its amplitude and phases are displayed on a screen in the form of curves referred to as "Lissajous" curves (Fig. 27). The recorded signals are interpreted by comparing them with those obtained from a reference component with anomalies that are representative of the phenomena studied. (Bray, 1992; Shull, 2002).

4.7.   Thermal method: Thermal infrared testing
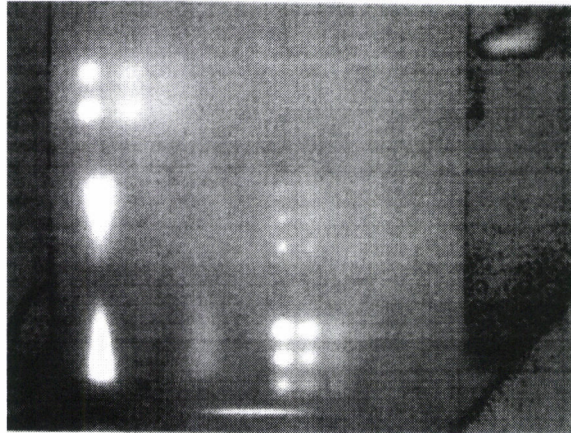
Fig. 28: Example of a thermal image showing differences in heat transfer with the surroundings (Hellier, 2001).

Non-intrusive inspection procedure, non-contact and very quick, based on the interpretation of thermal maps (thermograms) of the surfaces examined. (Hellier, 2001). A distinction is made between "passive infrared testing", which results from the simple observation of thermal gradients on a component or a system, and the "active infrared testing" wherein a thermal disturbance has been voluntarily created for testing (through a laser source for example) (Shull, 2002). Discontinuities in the component result in temperature differences (cold points) on the image (Fig. 28). Thermal image acquisition is achieved using a thermal imager connected to a computer. (Hellier, 2001; Kouzoubachian, 2006).

This method can detect obvious defects (delaminating, detachment) in thin parts and in relatively simple geometries. It can be applied to a wide variety of materials (plastics, composites, metal interfaces etc.) without however being able to detect deep-seated defects, due to its lack of sensitivity at significant depth. (Kouzoubachian, 2006).

4.8.   Acoustic methods: Ultrasound and Acoustic emission testing

Ultrasounds are mechanical vibrations, generated electrically, which propagate in a solid or liquid medium. It is based on the principle of the emission of an ultrasonic wave, which gets propagated in the component to be tested and is reflected from the obstacles encountered (anomalies, component boundaries). These waves are emitted by one or more "transducers" positioned by an operator or an automatic system. It is often necessary to use a couplant, generally in the form of an aqueous gel, between the probe and the component to ensure good wave transmission. (Hellier, 2001; Kouzoubachian, 2006).

(a) B-scan instrument   (b) B-scan

(b)

"C"—Scan image of block

C-scan
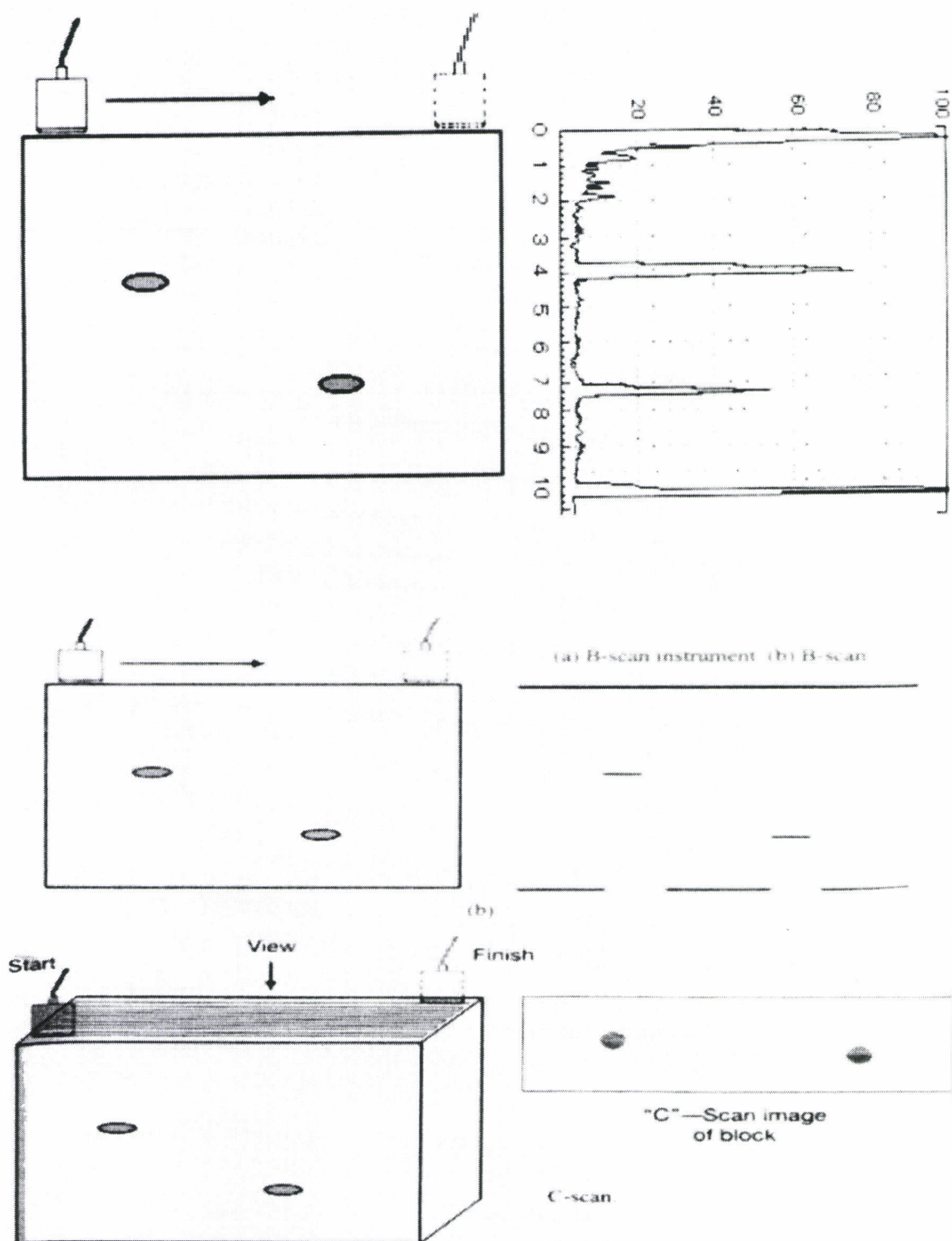
Fig. 29: Ultrasound information (Hellier, 2001).
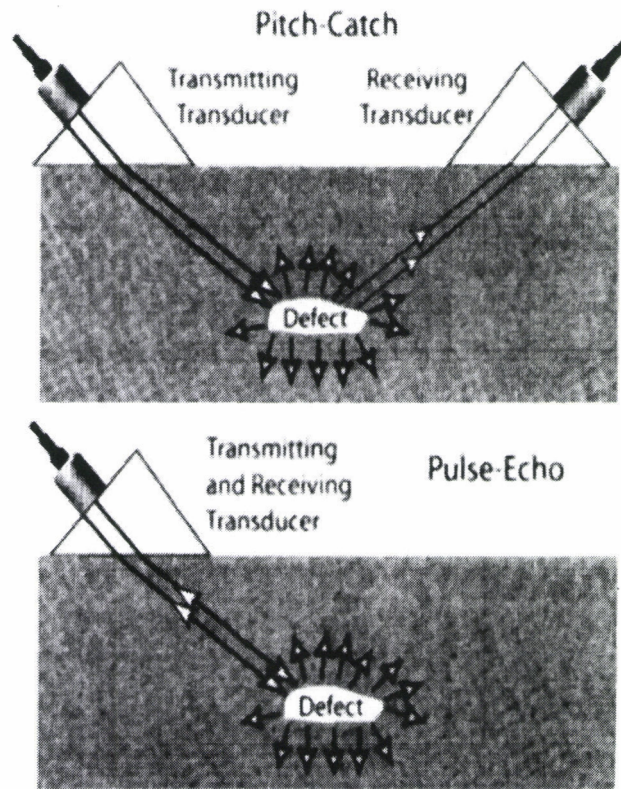
Fig.30: Transmitting and receiving transducers directed for a test (Shull, 2002).

The echoes are analysed on a screen by the inspector or processed in a measurement system for automatic installations. This method highlights discontinuities in mechanical properties found inside the material. There are several methods available for viewing the information obtained (Fig. 29). Typically the A Scan gives a direct view of the energy received; the B Scan gives a cross section of the tested component; the C Scan gives a map of the tested object. (Hellier, 2001). There are also several methods available for testing the component - transmission or reflection (Fig.30). (Shull, 2002).

Acoustic emission also uses wave propagation in the material: when the material changes, gets deformed, cracks under the action of an external stress (mechanical, thermal, chemical etc.), "elastic" waves are created spontaneously (Fig. 31). (Hellier, 2001; Kouzoubachian, 2006).

FRICTION SOURCES

CRACK FACE
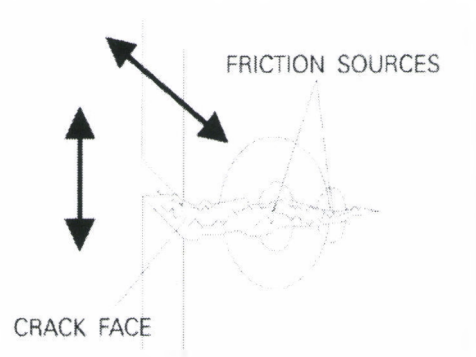
Fig. 31: Principle of elastic wave formation through cracking under acoustic emission (Hellier, 2001).

The intermittent release of energy in the form of a mechanical wave train takes place for each modification of the material condition. These wave trains get propagated in the material based on its acoustic properties and its geometry and reach the sensors installed on the equipment to be examined (Fig. 32). (Shull, 2002).
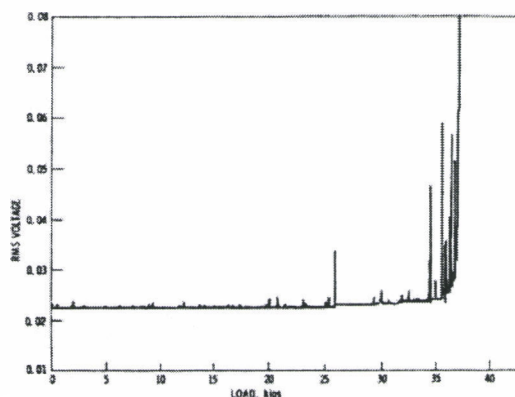
Fig. 32: Amplitude of signals emitted until material failure (Bray, 1992).

The signals collected in this manner and processed by a measuring chain help to locate the degradation area (map creation) and to evaluate its intensity based on the stress applied. The measurement quality therefore relies partly on the judicious selection and positioning of the sensors. (Bray, 1992; Hellier, 2001; Kouzoubachian, 2006).

4.9. Ionizing radiation methods: Radiology and tomography
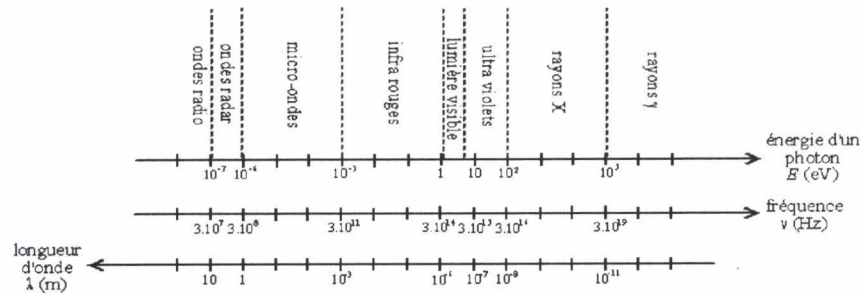
Fig.33: Range of electromagnetic spectrum as a function of the wavelength, frequency or photon energy (Source: Wikipedia).

Radiography makes use of the absorption of electromagnetic X or gamma rays by the material (Fig.33). (Shull, 2002). The distinction between X-rays and gamma rays (which are of the same nature and of similar energy) comes from the way they are produced: X-rays are photons produced by electrons of atoms while gamma rays are generated by atomic nuclei. (Bray, 1992). X-rays are a form of high frequency electromagnetic radiation, the wavelength of which is approximately between 1 picometre and 10 nanometre (Fig.33). Gamma rays possess a very small wavelength less than 1 picometre.
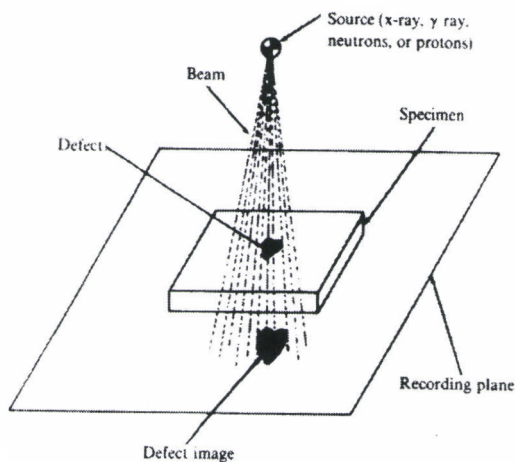
Fig. 34: Principle of radiography testing (Bray, 1992).
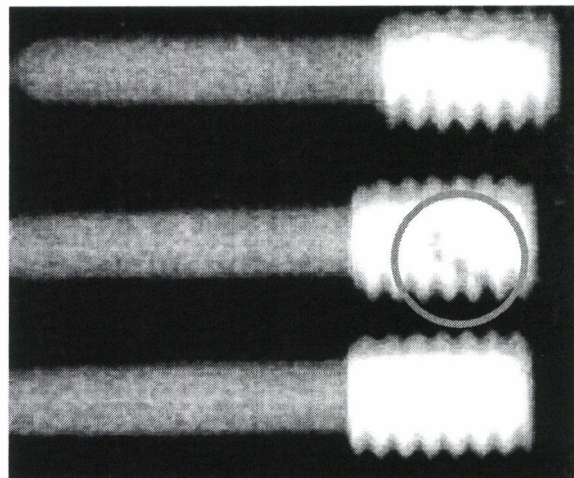
Fig. 35: Example of a radiogram on three screw-type metal products. The central screw shows an anomaly – dark zone circled in red – (Shull, 2002).

The non-absorbed radiation that remains after passing through the object is viewed with the help of either photographic films, fluorescent screens or other sensors (Fig. 34 and Fig. 35). Radiography essentially helps to detect internal defects (lack of material). Almost all materials can be examined using radiography and significant thicknesses can be tested. (Kouzoubachian, 2006). Gamma rays help to penetrate even greater thicknesses (Fig. 36).
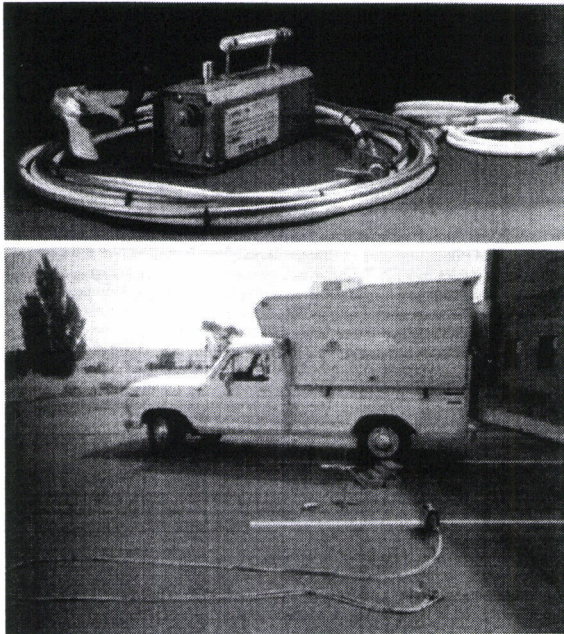
Fig. 36: Example of a device using gamma rays (Hellier, 2001).
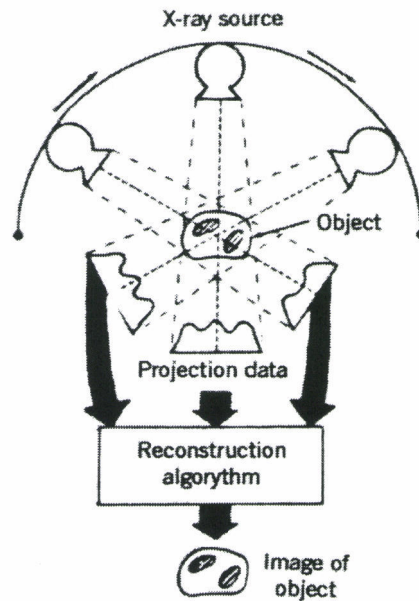
Fig. 37: Principle of image reconstruction under tomography (Bray, 1992).

Tomography, using X-rays, is one of the most recent methods applied in the industry. It is based on the same principle as the medical scanner. In fact, it deals with the reconstruction of successive 2D sections using the measurements made (Fig. 37). By amalgamation, a full 3D virtual image of the object can thus be obtained. It can be used to measure densities, dimensions, and to search for anomalies inside objects or even to examine in real time materials subjected to stresses. This method has developed mainly through advances in software and increases in processing capacities, in both the medical and industrial fields. (Bray, 1992; Kouzoubachian, 2006).

Neutronography is another radiation method (Shull, 2002). A neutron is a subatomic particle, without electrical charge. Neutrons, along with protons, are constituents of the atomic nucleus. This penetrating radiation can be used to image the inside of solid bodies, such as metals, minerals, fluids etc., and enables an analysis of their structure at atomic level by diffraction. Neutron spectroscopy is a unique tool for the study of body excitation forces, such as phonons and atomic vibrations. Another advantage of neutrons is their magnetic sensitivity. Since radiations interact very differently with objects, the images resulting from the 2 techniques (X-rays and neutrons) are in fact complementary. Neutrons in particular possess the capacity of viewing elements containing hydrogen atoms through a metal casing. (Kouzoubachian, 2006 and Wikipedia).

4.10. Optical methods

Interferometric and holographic techniques:

Optical holographic techniques measure surface deformation of the tested objects. Deformation is measured by comparing the wave front of a light beam after it reflects from the tested object with the wave front of this same object recorded previously on a hologram, in a reference configuration (Fig. 38). The light used to illuminate the surface of the specimen must be coherent and monochromatic. Hence a laser is generally used as the light source. High resolution film is another requirement for holography. A defect can be detected if an abnormal surface deformation is created around it, when the object is subjected to a strain (Fig. 39). (Brun, 2006; Diederichs, 2006).
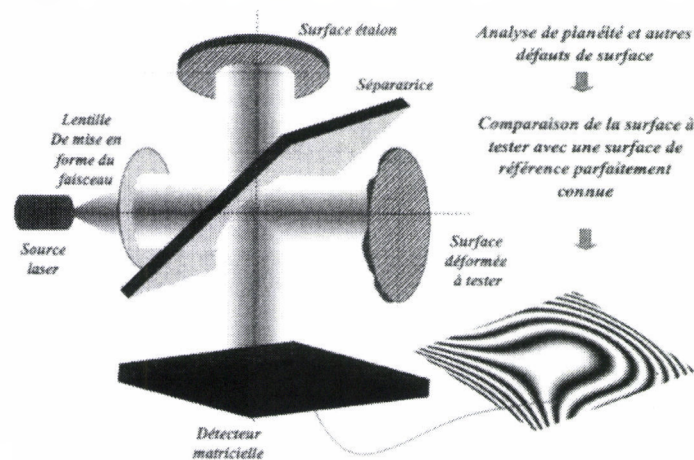
Fig. 38: Principle of interferometry as per Brun (2006).
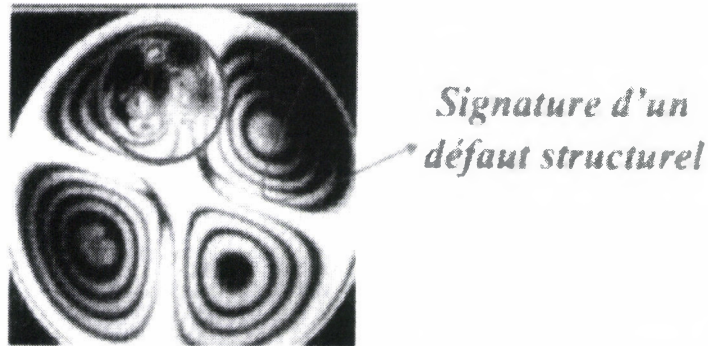
Fig. 39: Structural defect through modification of the signature of the mode of vibration (Brun, 2006).

Speckle interferometry has been invented to overcome the deficiencies of holography in the interferometry field with respect to the recording medium (halide plates and films, followed by thermoplastic films). Unlike the standard holographic interferometry, *speckle* interferometry makes use of CCD cameras to calculate and view the displacement fields of an object (Fig. 40). (Diederichs, 2006).
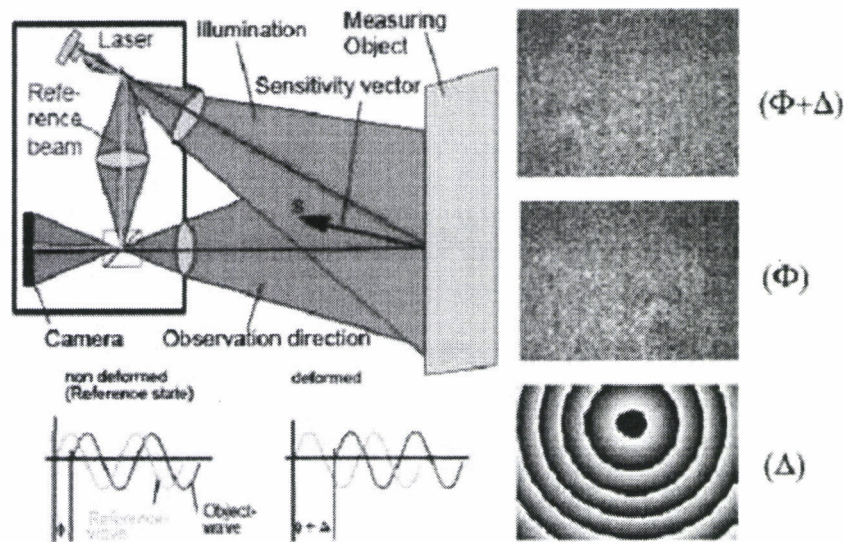
Fig. 40: Principle of holographic TV (ESPI) as per Ettemeyer (2004).

Fig. 41: Example of an industrial application for shearographic technique (Huber, 2006).

Speckle interferometry is highly suitable for industrial applications (more compact and more easily transportable instruments, less expensive, almost real time digital processing of data etc.) and has therefore developed very rapidly during the last few years and is progressively replacing existing holographic non-destructive testing systems (Fig. 41). Shearography and holographic TV (ESPI) are component elements of the several *speckle* interferometry techniques used. These techniques which are without contact, full field and almost real time, can measure displacements of the order of a few nanometres between two successive states of an object. (Ettemeyer, 2004; Huber, 2006).
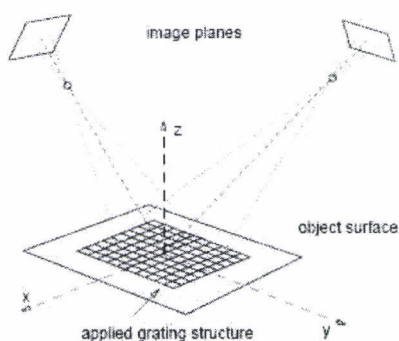
Fig. 42: Principle of image inter-correlation in 2 dimensions as per Ettemeyer (2004).
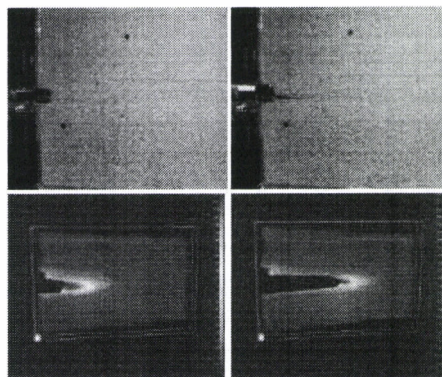
Fig. 43: Example of a breaking test on a large sized specimen (Ettemeyer, 2004).

Image inter-correlation:

The digital image correlation technique uses high resolution cameras to observe the surface of the tested object. The principle is illustrated in Fig. 42. If a structure is observed using two cameras, each point is associated with a discrete pixel in the image plane of each camera. Once the exact position of the cameras with respect to each other is known, the position of the structure point can be identified in the same system of coordinates. When the object is deformed, images can be recorded by both cameras and the same correlation procedures used to determine the dimensional offset of the object points (Fig. 43). Modern correlation algorithms can achieve displacement resolutions up to $1/100^{th}$ pixel, resulting in similar levels for deformation - stress. This corresponds to a factor that is 10 to 50 times less sensitive than the ESPI technique (Ettemeyer, 2004). Image analysis can be carried out in 2 or 3 dimensions.

Fig. 44 gives an example of an industrial application of image inter-correlation. The visual data is used to analyse shape imperfections in the tested surface such as dents. Primary system characteristics are autonomy and portability (spatial resolution: 5 millimetres). (Fournier, 2006).
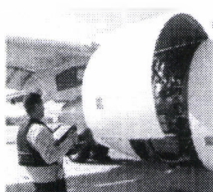
Fig. 44: " Shape View" device as per Fournier (2006).

4.11. Summary of advantages and disadvantages

Advantages	*Disadvantages*
Visual examination, Endoscopy (Hellier, 2001) – Rapidity of technique. – Apparent ease. – Requires only limited equipment. – Large area of application.	**Visual examination, Endoscopy** (Hellier, 2001) – Requires an experienced operator. – Subjective interpretation. – Detection of surface defects.
Liquid penetrant method (Source: http://www.cofrend.com) – Good crack detection sensitivity. – Orientation of defects immaterial. – Large area of application.	**Liquid penetrant method** (Source: http://www.cofrend.com) – Through and non-obstructed cracks. – Requires an experienced operator. – Disposal of chemical products.
Permeability method (Bray, 1992) – Range of techniques available. – Large area of application (materials).	**Permeability method** (Bray, 1992) – Very specific techniques. – Sensitivity depends on the technique used.
Magnetic particle method (Source: http://www.cofrend.com) – Detectability of 1 to 2 mm below surface. – Several magnetization methods. – Defects may be hidden.	**Magnetic particle method** (Source: http://www.cofrend.com) – Demagnetizable metals. Not applicable to wood. – Difficult for large parts. – Risk of arcing. – After which parts to be demagnetize and cleaned.
Eddy current (Source: http://www.cofrend.com) – Through defects (even obstructed). – Located at shallow depths (mm). – Distinction of types of anomaly. – Automatic measurements possible. – High temperature measurements possible.	**Eddy current** (Source: http://www.cofrend.com) – Materials that conduct electricity. Not applicable to wood. – Sensitive to a large number of parameters the variation of which must be understood. – Difficult for parts with complex shapes. – Local measurements.
Thermal infrared – Rapidity of technique. – Good quality portable devices. – Large area of application.	**Thermal infrared** – Surface inspection. – Image interpretation difficult. – Heat transfer sometimes difficult to generate.
Ultrasound (Source: http://www.cofrend.com) – Good penetration power. – Variable sensitivities, high accuracy possible. – Determination of position and size of defect. – Quick to implement and easy to transport. **Acoustic emission** (Hellier, 2001) – In-service inspection possible, large area of application. – Global testing method. – Real time testing.	**Ultrasound** (Source: http://www.cofrend.com) – Experienced operator. – Sensitive to structural / anisotropic effects and geometry. – Component / transducer connection. **Acoustic emission** (Hellier, 2001) – Sensitive to outside disturbances. – Measurement repeatability problem. – Difficult if absorbent material.
X-ray or gamma ray radiography (Source: http://www.cofrend.com) – Real time analysis possible. – Variable sensitivities, high accuracy possible – Deep penetration – Transportability (low energy X-ray generators, portable equipment for gamma of around 20 kg).	**X-ray or gamma ray adiography** (Source: http://www.cofrend.com) – High operating costs. – Experienced operator. – Dangerous radiations. – Often restrictive regulations.
Optical method – Rapid inspection. – Large zone of inspection. – No contact.	**Optical method** – Detection of surface defects. – Requires an experienced operator. – Importance of the quality of the texture sprayed and calibration.

5. Selection of inspection methods

5.1. Selection criteria

The selection criteria are defined in Table 1.

Denomination	Definition
Material	Method usable on wood.
Applicable	Method applicable to the testing objective.
Interpretation	Non subjective method.
Depth	Method capable of penetrating the material in depth [1].
Accessibility	Sounding with or without direct access[2].
Resolution	Width 0.1 mm; depth 10 mm[3].

Table 1: Definition of selection criteria.

(1): A crack is visible on the material surface but must not be considered as a surface defect. Deep damage of the material very significantly increases the risk of total structural failure.

(2): Methods capable of penetrating the structure without direct access are preferred.

(3): If the depth is greater than 10 mm, then the crack is detected. The resolution selected corresponds to the estimated upper limit. Non-destructive techniques must have a resolution value smaller than the value given in Table 1.

5.2. Scoring of methods based on criteria

The grading system given below is used to select the inspection methods (Table 2). If the criterion is negative or there is imbalance between the scores given by different methods, the scoring needs to be justified.

Denomination	Definition
-	Negative criterion; disqualifying score.
+	Acceptable; average.
++	Acceptable; good.
+++	Acceptable; very good.

Table 2: Definition of grading system.

5.3. Application of criteria

– Visual methods: Visual, optical or video endoscope

Visual inspection undoubtedly requires a certain skill to recognize the type of defects found.

⇨ Interpretation of the observation is subjective.

– Liquid penetrant method

This method completes the visual inspection by making very fine surface defects appear in a coloured or fluorescent contrast. These marks are then visible to the naked eye.

⇨ This method helps to detect opening fissure type surface defects. A crack is not characterized by material fissuring but by a deformation comparable to a wrinkle. Furthermore, wood is a porous material and problems can occurred while testing (diffusion and elimination of liquid).

‒   Permeability testing method

Permeability testing is used to identify or detect gas movement from one side of a wall to another. Leaks need to be created intentionally by applying differential pressure upstream and downstream in order to provoke gas flow.

⇨ Permeability testing is a very specific technique and cannot be applied to the testing objective defined in phase 1.

‒   Magnetic method: Magnetic particle testing

This technique can be applied only for ferromagnetic materials and alloys (iron, steel, cast iron, chromium alloys etc.).

⇨ Wood cannot be tested using this method.

‒   Electromagnetic method: Eddy current

This method can be applied to all materials that conduct electricity.

⇨ Wood cannot be tested using this method.

‒   Thermal method: Thermal infrared testing

Non-intrusive inspection procedure, without contact and very quick, based on the interpretation of thermal diagrams (thermograms) of the surfaces examined (heat exchange must take place between the tested object and the outside). This method can detect well-defined defects without being capable of detecting deep defects.

⇨ Infrared thermography can detect surface defects or not very deep defects. Direct access to the tested surface is required.

‒   Acoustic methods: Ultrasound and Acoustic emission

Ultrasound: It is often necessary to use a couplant between the probe and the component. Defects can be detected inside the material. There are also several methods for testing the component: primarily by transmission or by reflection.

Acoustic emission: Location of the degradation zone (zone mapping) and evaluation of its intensity based on the subjected stress and strain (the object must be deformed).

⇨ These two methods enable a material to be tested in depth. In some cases of material continuity, direct access is necessary. Reflection sounding is suitable for this testing objective.

- Ionizing radiation method: Radiology and tomography

X-rays (with wavelength between 1 picometre and 10 nanometres) and gamma rays (wavelength less than 1 picometre) can detect internal defects (voids in the material). Gamma radiation can penetrate large thicknesses.

⇨ Radiology can be used to image a material in depth. Direct access to the concerned area is not required. Furthermore, this sounding method has very good spatial resolution (Fig. 1).

- Optical methods

Interferometry and holographic techniques measure surface deformation of the tested object (the object must be deformed). These no-contact techniques can measure displacements of the order of a few nanometres between two successive states of an object.

Image inter-correlation: This technique measures deformations on the surface of the tested object (the object must be deformed). It possesses a sensitivity which is 10 to 50 times less than interferometry.

⇨ Optical methods can detect surface defects. Direct access to the tested surface is required.
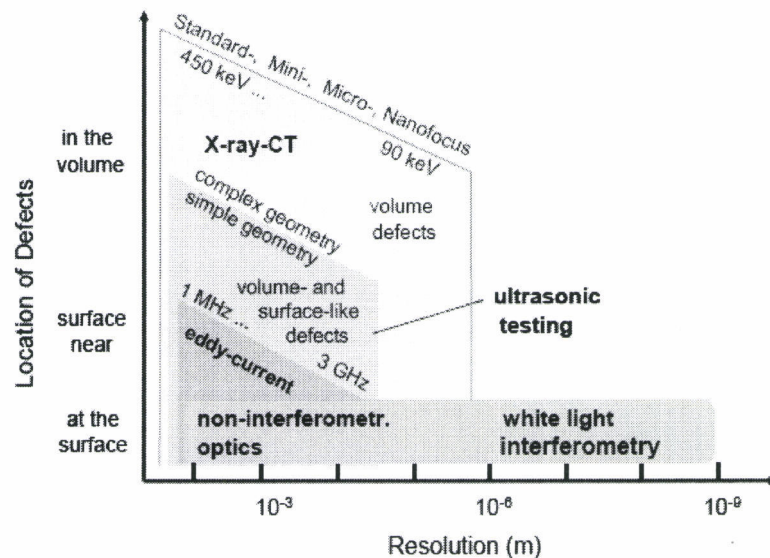
Fig. 45: Comparison of 'X-ray', 'Ultrasound', 'Eddy current' and 'Optical measurement' methods based on the location of the detectable defect and the spatial resolution. As per: Bergmann R.B., Bessler F.T., Bauer W. (2006), "Non-Destructive Testing in the Automotive Supply Industry - Requirements, Trends and Examples Using X-ray CT", 9th European Conference on Non-Destructive Testing, 25-29 Sept., Berlin, Germany. http://www.ndt.net/.

5.4.   **Summary table**

Method \ Criterion	Material	Applicable	Interpretation	Depth	Accessibility	Resolution	Result
Visual	+	+	-	/	/	/	0
Liquid penetrant	+	+	+	-	/	/	0
Permeability	+	-	/	/	/	/	0
Magnetic particle	-	/	/	/	/	/	0
Electromagnetic	-	/	/	/	/	/	0
Thermal	+	+	+	++	+	+	7
Acoustic	+	+	+	+++	++	+	9
Radiation	+	+	+	+++	+++	+	10
Optical	+	+	+	+	+	+	6

Table 3: Selection of methods that are most suitable for the testing objective. The shaded zones represent the selected methods.

The inspection methods selected in Table 3 are thermal infrared testing, acoustic methods (ultrasound and acoustic emission), radiology methods (X-rays, gamma rays) and the optical methods (image analysis). Certain selected methods are complementary; several of these methods may be combined to increase the detection power of the implemented inspection protocol:

- X-rays and gamma rays – Deep inspection without direct access.

- Ultrasound – Deep inspection with direct access.

- Image analysis – Surface inspection with direct access. Only this method is considered since it is not necessary to mechanically apply stress to the tested object. This method is similar to a visual examination; it is however non subjective.

- Thermography – Surface inspection with direct access (the surface must be previously heated).

- Acoustic emission – Passive retrieval and without direct access ⇨ In-flight testing.

6. Experimental methodology

6.1.   Development of test specimens

6.1.1.   Damage tests

The wood species used is the Sitka spruce (*Picea sitchensis*) which is used in the CAP10 spar chords. Each specimen must as far as possible be of straight grain, without knots or defects. The specimens are shaped like a straight prism with a rectangular section, with the following dimensions (height x breadth x length):

-    10 x 40 x 100 mm, 10 x 50 x 100 mm, 10 x 60 x 100 mm

-    10 x 40 x 150 mm, 10 x 50 x 150 mm, 10 x 60 x 150 mm

-    10 x 40 x 200 mm, 10 x 50 x 200 mm, 10 x 60 x 200 mm

-    10 x 40 x 300 mm, 10 x 50 x 300 mm, 10 x 60 x 300 mm

12 methods in total have thus been defined. Each method corresponds to 2 batches of 5 specimens. The specimen axes are directed along the axis of symmetry of the wood; the cross section corresponds to the radial (width) – tangential (height) plane and the length corresponds to the longitudinal axis of the material. This method of cutting is similar to that used for making the CAP10 spar chords. The specimens are previously stored in an environment at temperature of 20°C ± 2°C and 65% ± 5% of relative humidity. The reference humidity is then 12%.
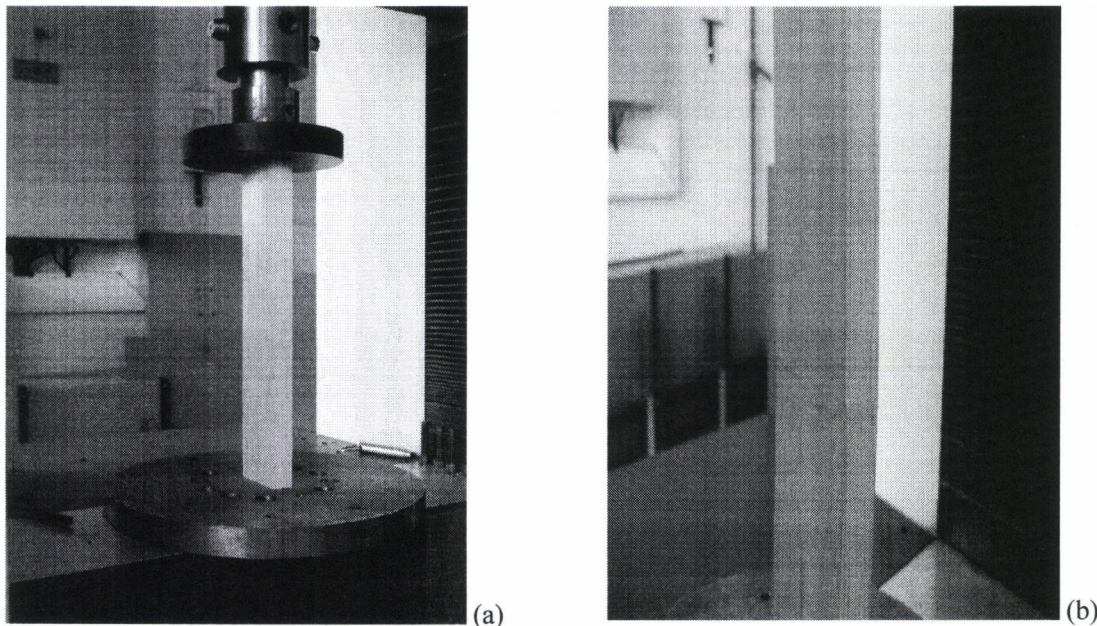
Fig. 46: Axial compression test (a: start and b: appearance of the crack before stoppage).

The specimens of each batch are subjected to an axial compression test as per standard NF B 51-007 (Sept. 1985) so as to artificially create compression cracks without destroying the specimen (Fig. 46). The tests are stopped by the operator as soon as soon as the typical wrinkling feature of compression cracks appears. Five tests specimens were selected to ensure valid sampling. During the tests, 9 specimens out of 55 failed (no crack), i.e. a failure rate of 16%. It is often the end of the specimen bearing the brunt of the stress, which failed, thereby preventing any buckling (Fig. 47).
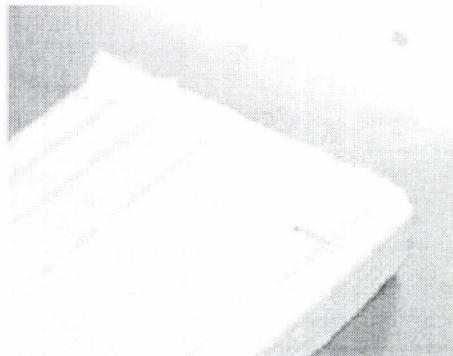
Fig. 47: Example of damage to the end following axial compression test.

The axial compression test is preferred to the bend test bearing in mind the difficulty to artificially create a crack by bending a test specimen. The incipient crack is produced when the specimen buckles. The test is then similar to a bend test; the incipient compression crack is 'guided' so as to promote the appearance of a well-defined damage of the same type as the cracks actually observed.

In the case of a compression test and as per the selected cutting method, the depth of the cracks developed will be in the LT plane (with surface wrinkles in the LR plane). Specimens of the preliminary studies were damaged in the same manner. The same applies to the laminates that make up the spar chords of the CAP10.

6.1.2.   Preparation of test specimens

In the specific case of the CAP10, the spar consists of two chords in Sitka spruce (*Picea sitchensis*) obtained by lengthwise (keyed) joints, transverse joints and by bonding 5 (upper surface) and 3 (lower surface) plies, 12mm thick.

In order to make test specimens that are most representative of the elements of the spar which bears the compression cracks, each specimen of batch 1 is glued to a specimen from batch 2 as shown in Fig. 48.
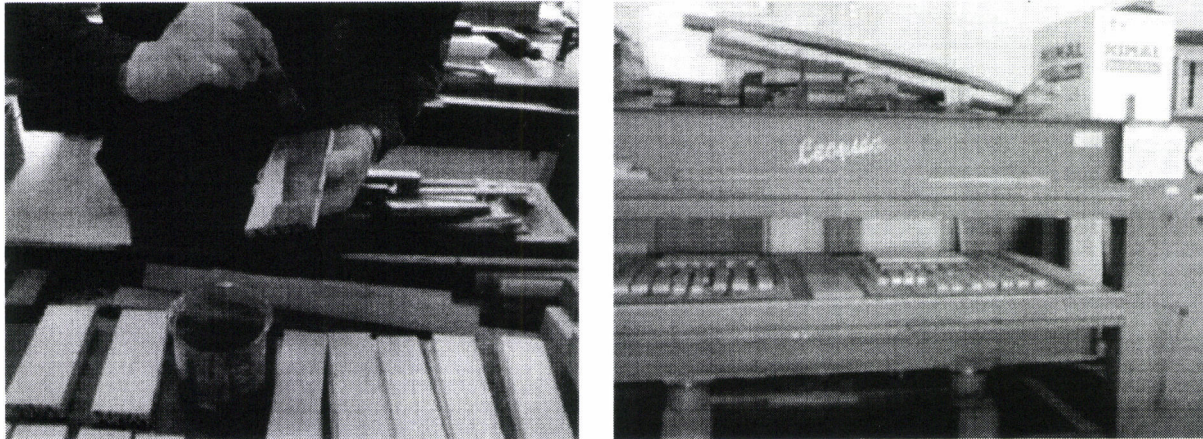
Fig. 48: Pressure-bonding using Sader Marine adhesive.

Bonding is done using a joiner's adhesive called Sader Marine (resorcine-phenol-formol based adhesive manufactured by CECA S.A., Paris). The specimens were then pressed between two plates heated to 40°C for two and half hours (Fig. 48). 51 test specimens were made in total and identified {410, 510, 415...} (Fig. 49 and Table 4). The first digit gives the width and second two the length. The identifier is followed by {/26, /37...}. The first and second digits give the individual number of each specimen before bonding (.../26 signifies that the specimen 2 is bonded to specimen 6). The first digit also refers to the number of the specimen exhibiting one or more cracks.
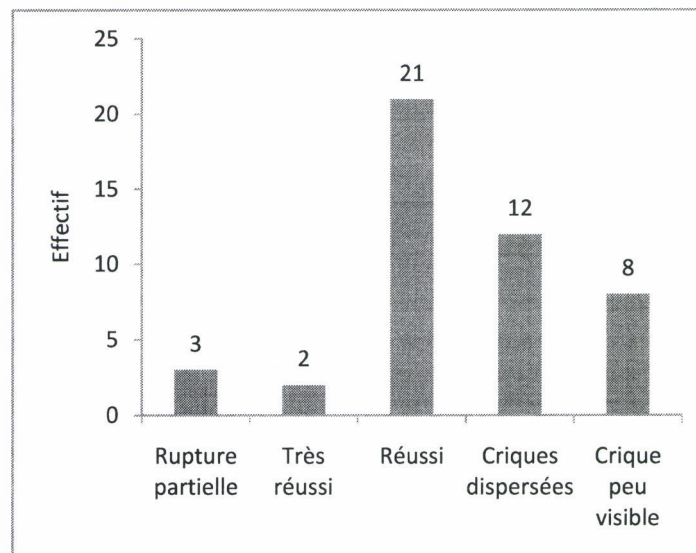
Fig. 49: Distribution of the size of damage (visual examination of the cracks).

Family	Reference	Analysis	Classification	Observations
410	410/26	X-rays	1	Partial failure (very damaged)
	410/37	Thermal infrared	3	Successful
	410/48	Ultrasound- LMA	3	Successful
510	510/24	Ultrasound -EPA	3	Successful
	510/101	Ultrasound- LMA	3	Successful
610	610/48	X-rays	3	Successful
	610/57	Thermal infrared	2	Very successful
	SI=610/16	Thermal infrared	X	Reference without defect
415	415/29	X-rays	3	Successful
	415/38	Thermal infrared	4	Right depth cannot be read
	415/47	Ultrasound-EPA	3	Successful
	415/56	Ultrasound-EPA	3	Successful
515	515/23	Ultrasound-EPA	4	Several dispersed small cracks
	515/48	X-rays	4	Left depth cannot be read on account of knot
	515/610	Ultrasound- LMA	4	Left depth in full knot, very visible
	515/71	Thermal infrared	4	Small knot dead centre
	SII=515/53	X-rays	X	Reference without defect
615	615/73	Thermal infrared	3	Successful
	615/92	Ultrasound- LMA	4	Several dispersed small cracks
	615/101	X-rays	2	Very successful
	SIII=615/64	Ultrasound- LMA	X	Reference without defect
420	420/16	Thermal infrared	3	Successful
	420/27	X-rays	3	Successful
	420/38	Ultrasound-EPA	5	Crack hardly visible
	420/49	Ultrasound-EPA	3	Successful
	420/510	Ultrasound- LMA	5	Crack hardly visible
520	520/110	X-rays	3	Successful
	520/29	Ultrasound- LMA	3	Successful
	520/38	Ultrasound-EPA	4	Several dispersed small cracks
	520/47	Ultrasound-EPA	3	Successful
	520/56	Thermal infrared	4	Several dispersed small cracks
620	620/29	Ultrasound-EPA	5	Crack hardly visible
	620/38	Thermal infrared	3	Successful
	620/47	X-rays	3	Successful
	620/56	Ultrasound-EPA	4	Right depth hardly visible
	SIV=620/110	Ultrasound-EPA	X	Reference without defect
430	430/110	Ultrasound- LMA	5	Crack hardly visible
	430/29	Ultrasound- LMA	5	Crack hardly visible
	430/38	Ultrasound-EPA	4	Right and left depth not visible
	430/47	Ultrasound- LMA	4	Right and left depth not visible
	430/56	Ultrasound-EPA	1	Partial fracture (very damaged)
530	530/16	Ultrasound-EPA	3	Successful
	530/27	Ultrasound- LMA	5	Crack hardly visible
	530/38	Ultrasound- LMA	1	Partial failure (very damaged)
	530/49	Ultrasound- LMA	3	Successful
	530/510	Ultrasound- LMA	5	Crack hardly visible
630	630/28	Ultrasound-EPA	5	Crack hardly visible
	630/37	Ultrasound-EPA	4	Several dispersed small cracks
	630/49	X-rays	3	Successful
	630/510	Thermal infrared	3	Successful
	SV=630/16	Ultrasonic- LMA	X	Reference without defect

Table 4: Listing and characteristics of test specimens.

6.2.   Allocation of research activities

The selected non-destructives methods are: ultrasound, acoustic emission, image analysis, X-rays and/or gamma rays and thermal infrared. The distribution of research activities and organisation is shown in Fig. 50.

These methods require specific and complex skills. CIRAD and the FCBA therefore called for support from associate laboratories, LMA, CNDRI and associate companies, EPA and ThermoConcept, which have undertaken the following research activities:

- FCBA:
    o Machining of sound specimens.
    o Tests on CAP10 spar and wing alongside EPA.

- CIRAD:
    o Manufacture of test specimens.
    o Image analysis on test specimens.
    o Testing the overall research activity.

- LMA:
    o Underwater type ultrasound applied on test specimens in conjunction with CIRAD.
    o Underwater type ultrasound applied on a piece of the CAP10 spar.

- EPA:
    o Elastomer couplant ultrasound on test specimens.
    o Acoustic emission on test specimens in conjunction with CIRAD.
    o Acoustic emission on spar and wing of the CAP10.

- CNDRI:
    o X-rays in transmission on test specimens.
    o X-rays by Compton diffusion on test specimens.

- TC:
    o Thermal infrared on test specimens.

FCBA: Forêt Cellulose Bois-construction Ameublement. (Mécanique des Matériaux).

CIRAD: Centre de coopération Internationale en Recherche Agronomique pour le Développement. (UPR 40 - Bois Tropicaux).

LMA: Laboratoire de Mécanique et d'Acoustique (CNRS UPR-7051).

EPA: Euro Physical Acoustics (http://www.epandt.com/).

CNDRI: Contrôle Non Destructif par Rayonnements Ionisants (INSA – Lyon).

TC°: ThermoConcept (http://www.thermoconcept-sarl.com/).

Machining of specimens: FCBA

Creation of cracks by buckling under compression

Manufacture of test specimens

Image analysis: CIRAD

Underwater ultrasound: LMA

Ultrasound using elastomer couplant: EPA

X-rays: CNDRI

Thermography : ThermoConcept

Destructive tests in axial compression: CIRAD

Tests realised in order to validate

the acoustic emission technique: EPA

Analysis of results on test specimens: CIRAD and FCBA

4-point bending tests on a CAP10 spar and wing: FCBA

Tests realised in order to validate

the acoustic emission and ultrasound techniques: EPA

Analysis of results on CAP10 spar and wing: CIRAD and FCBA

Fig. 50: Sequence of research activities.

7. Image analysis

7.1.   Experimental protocol

After all the specimens were made, they were flat scanned (12 points per mm), the lighting being directed perpendicular to the specimen. The images were then analysed with version 1.36b of the ImageJ software (public domain, available at address http://rsb.info.nih.gov/ij/). ImageJ software was created by the American "National Institutes of Health" (NIH).
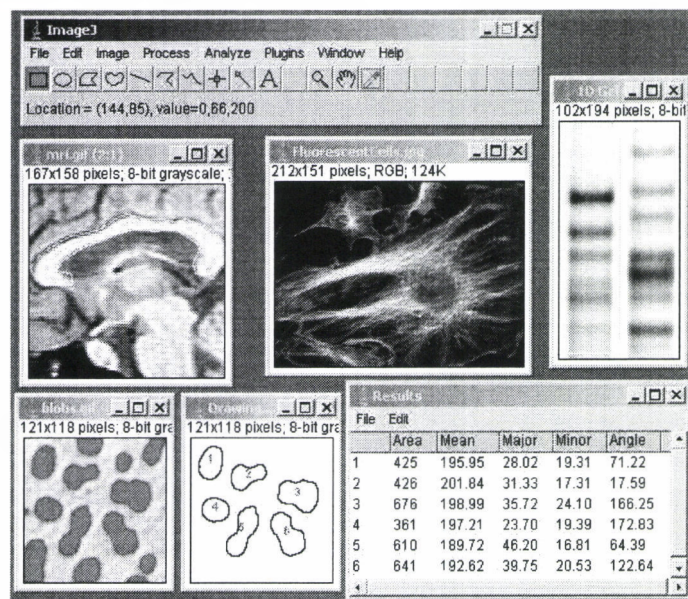
Fig. 51: Example of imageJ user interface available at http://rsb.info.nih.gov/ij/docs/concepts.html.

ImageJ offers several standard image processing functions (Fig. 51): display and adjustment of the grey level histogram, noise suppression, lighting correction, contour detection, direct-inverted Fourier transform, threshold, logical and arithmetic operations between images and in general any other linear transformation by customized mask definition. Processes stemming from mathematical morphology are also available such as erosion – dilatation. ImageJ also helps to count particles, evaluate their aspect ratio, measure different magnitudes (distances, surfaces etc.), and extract contour data for example.

7.2.   Results

The results are presented as per the example of specimen B530/49. The colour image is converted into an 8 bit grey level image. This image is then converted to negative (Fig. 52). Wrinkling, the distinguishing feature of a crack, then becomes clearly visible.

(a)   (b)
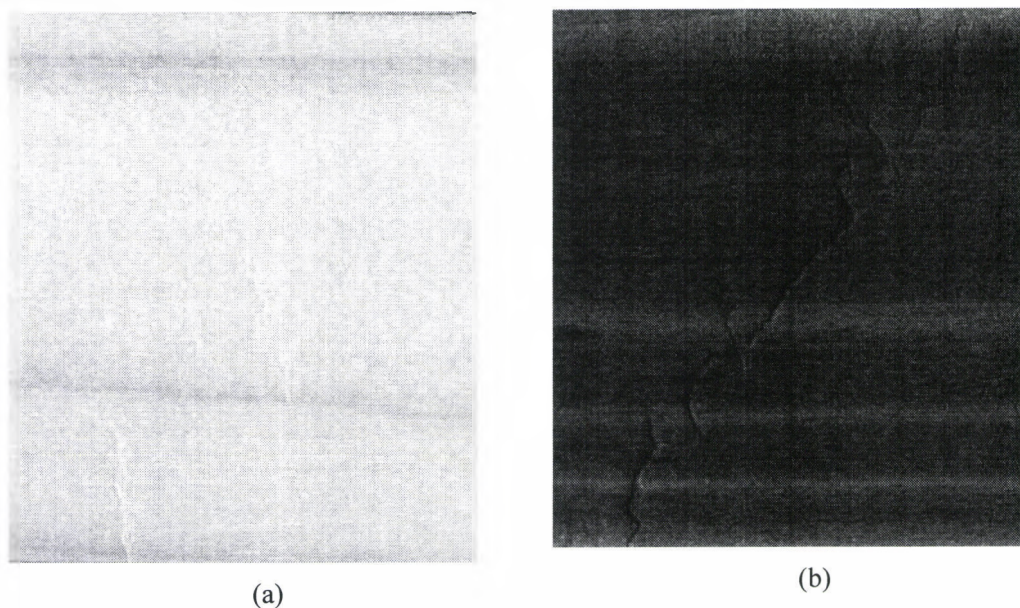
Fig. 52: Conversion of the original image to (a) reversed 8 bit image (b) a grey level image (B530/49).

A threshold is then defined from the grey level histogram for highlighting the crack contour (Fig. 53).

(a)

(b)
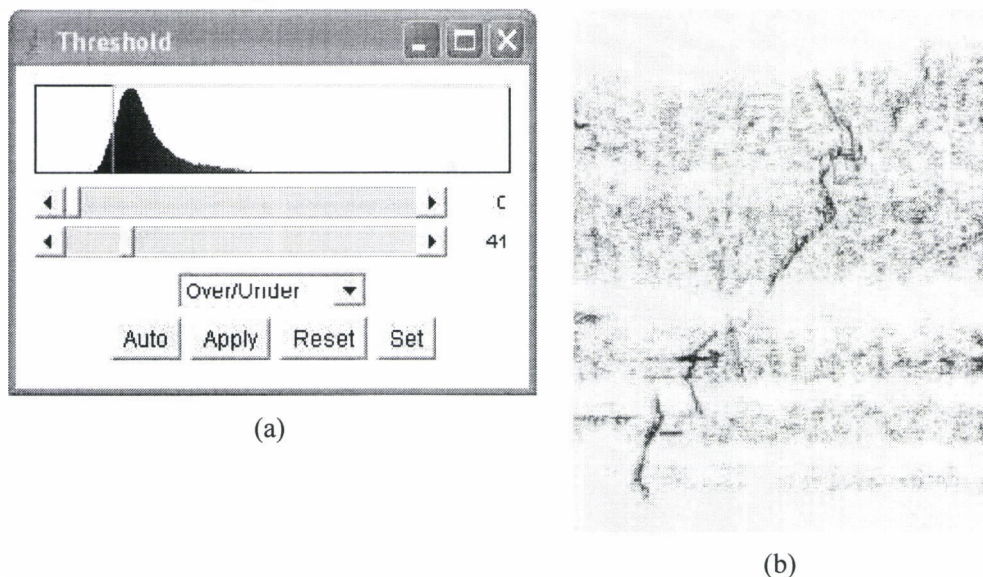
Fig. 53: Threshold adjustment (a) of the reverse 8 bits image (B530/49) and result (b).

This very simple method of image processing was applied to all the specimens to check whether the cracks could be highlighted. In certain cases, the natural texture of the wood completely masked the crack. Using this method for inspection would then be possible if:

- The test is done under various angles of incident light beam.

- The image deformation obtained due to the optics of the imaging system and to the different angles of incidence can be corrected by applying sufficient resolution.

    – The variations in the natural wood texture can be eliminated by appropriate image filtering.

8. Thermal infrared

This study was undertaken by THERMOCONCEPT.

TREFLE ENSAM -Esplanade des Arts et Métiers, 33 405 TALENCE CEDEX

8.1. Experimental methodology of non-destructive testing by thermal infrared

The object of this study is to validate the feasibility of detecting incipient compression failure of wood fibres at the specimen surface (compression cracks). The methodology shown in Fig. 54 has been applied to develop a measuring device for detecting any delamination in composite materials. The test rig (Fig. 54) consists of a thermal imaging system, an excitation source and a processing unit with an image acquisition card.
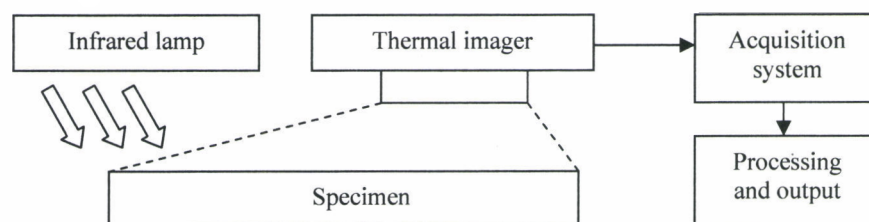
Fig. 54: Schematic diagram of thermal infrared testing.

The excitation source may be for example a simple 500W halogen light or an infrared lamp, with which it is possible to excite the specimen by changing parameters: distance from the specimen, duration of excitation. The advantage of this type of excitation is that it is without contact and positioned in front of the material thereby providing easier handling. It is difficult to quantify the total energy applied to the material. However, the processing methods developed do not take account of the excitation flux of the specimen and it will therefore not have any impact on test results.

The infrared camera collects the thermal data and transmits it to the processing unit. Algorithms enable the use of inexpensive imaging systems, which deliver signals with high noise levels, such as an un-calibrated bolometric type of infrared camera from Raytheon, model PalmIR 250. This type of camera can record 30 images per second, and is a thermal imaging system which does not allow direct access to the absolute temperature field but to a proportional field, sufficient for NDT-related processing.

The processing unit can record and process data from the camera, and provide a result in the form of images and curves describing the evolution of the selected parameters (detection of delamination, inclusion, density estimation, thickness estimation etc.). Image processing is carried out using software developed by THERMOCONCEPT.

(a)   (b)
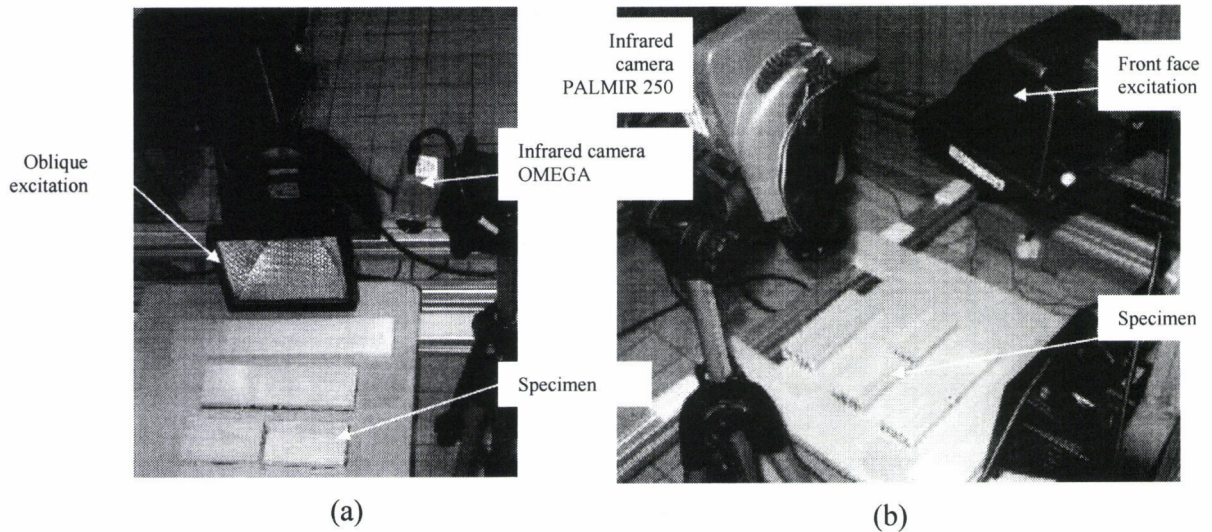
Fig. 55: Photos of the experimental rigs used (a)oblique excitation, (b) front face.

The test technique involves subjecting the specimen to thermal excitation and measuring its temperature response using a thermal image sensor system (Fig. 55). Appropriate processing of the burst of images is done based on the excitation, the nature of the material etc. to locate the defects, if any, on the specimen. This location is carried out on each pixel using a chart drawn using a parameter representing the thermo-physical properties of the material at each pixel. The final image obtained will then show the defects in the specimen. These might be of the resistive type (inclusions, delamination defects), local defects of excess or lack of density.

The objective of the process is twofold: it must on the one hand estimate variations of appropriate parameters for locating the zones of defect and on the other hand eliminate the noise in the signal provided by the thermal imaging system.

The methodology used is first validated on a calibrated specimen in carbon and epoxy resin composite parallelepipedic in shape $70x80x1$ mm^3. Defects are simulated by Teflon inserts placed between two carbon plies. By using this methodology it was demonstrated that closed splits (fissures) as well as other knot like defects could be detected and marked in a pine plank (Fig. 56).

(a)
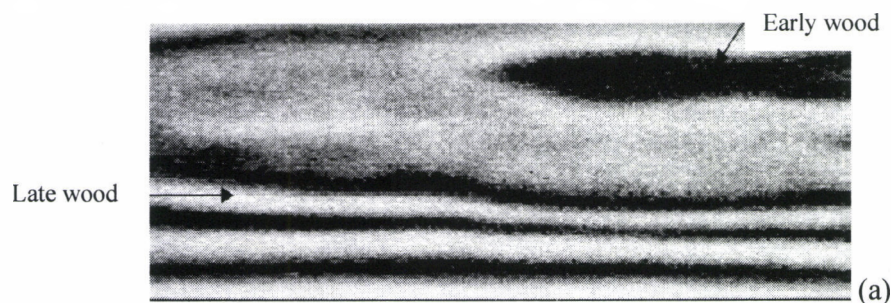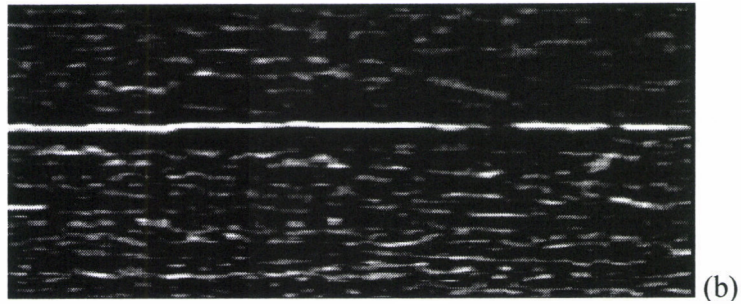
Fig. 56: Diffusivity mapping in a pine plank (a) processed infrared image of wet wood (b).

8.2.   Description of infrared cameras used

Two infrared cameras were used:

1) A ferroelectric camera RAYTHEON PALMIR 250
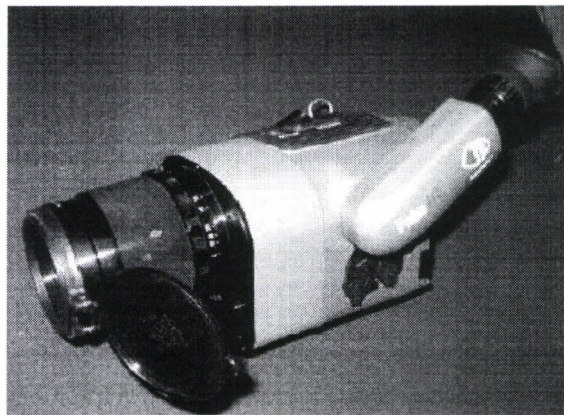
Fig. 57: RAYTHEON PALMIR 250 camera.

- Sensor size: 320x240 pixels.
- Video output: Video (CCIR, RS 170).
- Acquisition method: National Instruments video capture card.
- Type of data: Matrix 320*240 of whole 8 bits.
- Sensor technology: Ferroelectric.
- Frequency: 30 Hz.

2) A bolometric camera INDIGO OMEGA A10

Fig. 58: INDIGO OMEGA A10 camera.

- Sensor size: 160x120 pixels.
- Video output: Digital and analogue.
- Acquisition method: National Instruments (digital or video).
- Type of data: Matrix 160*120 whole 14 bits.
- Sensor technology: Micro bolometre not cooled.
- Frequency: 25 Hz.

8.3.   Results and analysis of thermal infrared testing

Compression crack
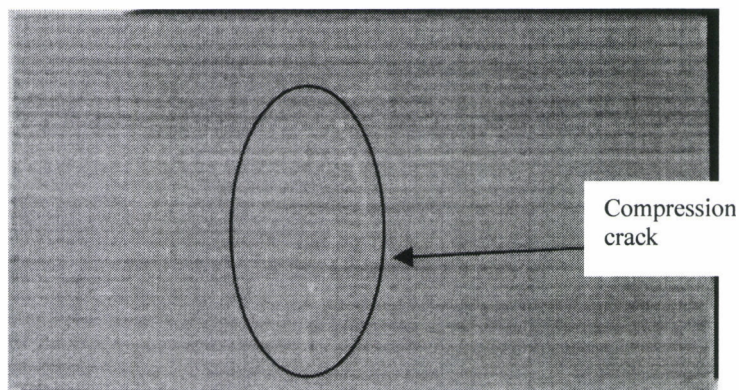
Fig. 59: Specimen no.B610/7 B610/5 subjected to thermal infrared testing.

The tests involved applying a thermal excitation to the specimen surface, on which the camera was focussed. The specimen concerned was No. B610/7 B610/5 (Fig. 59). Different techniques and processes were used to detect the defect:

- "Front face flash" excitation.

- – "Front face step" excitation.

- – Oblique excitation.
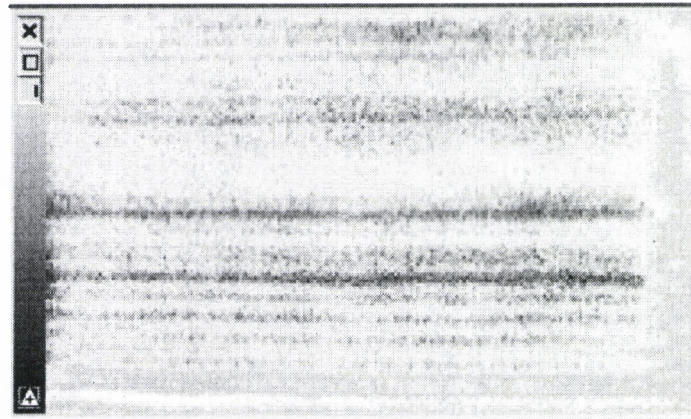
Fig. 60: Example of response time image obtained after processing a burst of infrared images.

Approximately ten tests and associated processing were carried out on the specimen. The defect in Fig. 59 is not highlighted as shown in the example in Fig. 60. In fact, the growth rings are visible and encompass the whole contrast range. Irrespective of the type of excitation or the method used, the defect could not be detected.
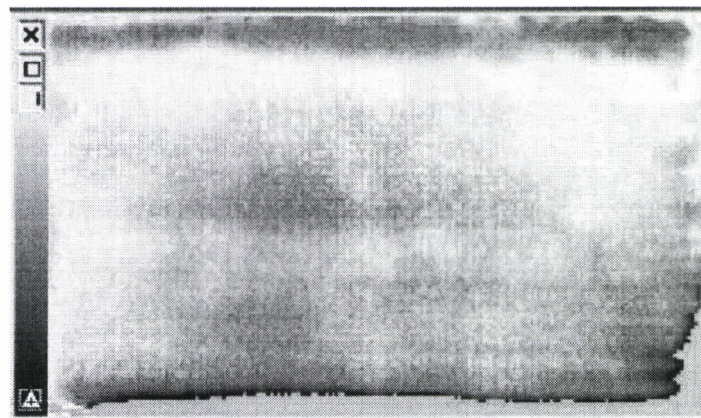
Fig. 61: Example of response time image obtained after processing a burst of infrared images and surface moisture penetration in wood.

Tests were also carried out by dampening the specimen. This technique has already been used effectively for the detection of closed splits at the surface of a pine plank. The presence of water modifies the thermal properties of the winter and summer wood making them more homogeneous. Unfortunately the defect is still not visible in Fig. 61.

This type of defect does not seem to generate significant changes in the thermo-physical properties of wood enabling its detection.

9. X-rays

This study was carried out by the Laboratoire Contrôle Non Destructif par Rayonnements Ionisants (CNDRI) INSA-Lyon.

9.1. Experimental protocol

9.1.1. Imagery by transmission

Imagery by X-ray transmission corresponds to the medical technique of radiography for obtaining an image of the inside of an object. The contrast achieved in the images depends on the variations in attenuation of the object (which stems from the variations of both density and atomic number i.e. the chemical composition) but also on the differences in thickness. The greater the variation (in attenuation and/or thickness) in the direction of the incident beam, the greater the contrast (Fig. 62).
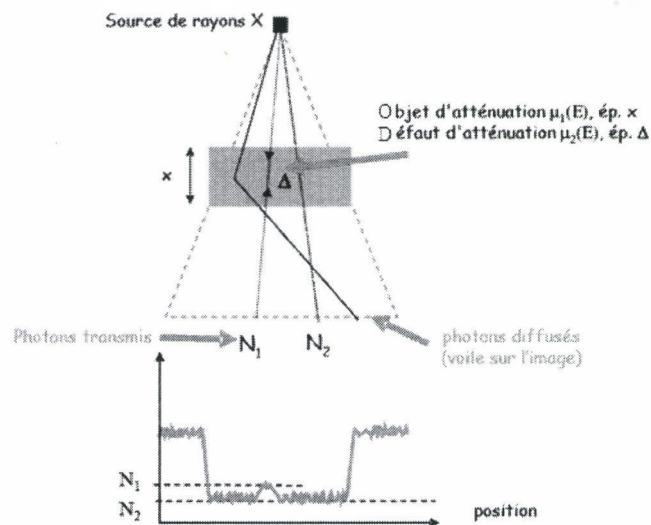
Fig. 62: Schematic diagram for testing by X-ray transmission .

The system used for obtaining the images is a high resolution imagery line, using a micro-focus tube (THALES Hawkeye) and an acquisition sensor specially designed in the laboratory (Fig. 63). The purpose of the micro-focus tube is to provide a high geometric magnification G, while maintaining time an acceptable level of geometric blurring f (the relationship between both the parameters being f = d(G-1) where d is the focal spot size).
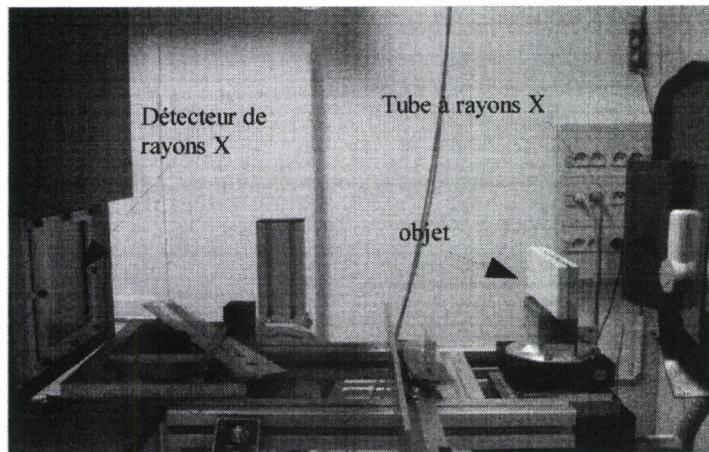
Fig. 63: Photograph of the assembly used for X-ray transmission testing.

The experimental conditions under transmission are given below:

- Voltage: 35 kV.
- Intensity: 400 µA.
- Focus: 20 µm.
- Duration of acquisition: 1 minute.

9.1.2. *Measurement by Compton diffusion*

Diffusion imagery is an inspection technique used by laboratories over many years, but which does not have an equivalent in the medical field since the level of X-rays required for measurement is generally high. Compton diffusion, or diffusion with loss of energy, is one way in which X-rays can interact with matter. During transmission imagery, the diffused radiation is considered as noise since it does not bring in any information on the location of the defect. However, this radiation does hold information if collected at a specific angle so that it does not get combined with the directly transmitted radiation (Fig. 64).
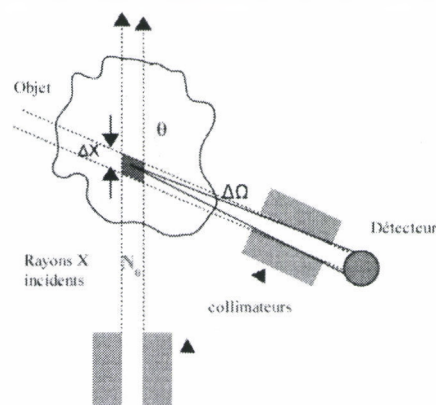
Fig. 64: Schematic diagram of testing with X-rays by Compton diffusion.

The diagram in Fig. 64 shows a configuration for testing by diffusion at an angle θ. The collimation of the beam at input and at output determines the measuring volume. The advantage when compared to transmission testing is that atomic number variations as well as thickness variations can be eliminated.
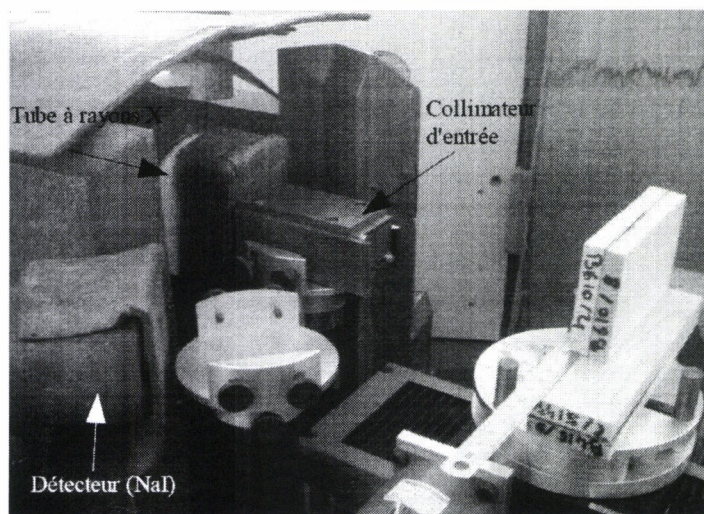
Fig. 65: Experimental measurement rig using Compton X-ray diffusion. The sensor is shielded by lead. The X-ray tube is also surrounded by lead.

Geometric configuration requires access only on one side of the component, which makes it particularly attractive for the inspection of acrobatic aircraft. However it is a slow testing process taking into account the fact that measurement is carried out one point at a time and requires scanning of the component. The sensitivity of the method is also directly linked to the size of the collimators, which is inversely proportional to the quantity of signal received. The experimental measurement rig is shown in Fig. 65.

The experimental conditions under Compton diffusion are as follows:

-   Angle θ: 135°.
-   High voltage: 120 kV.
-   Intensity: 230 µA.
-   Focal point: 20 µm.
-   Sensor: NaI in metering mode.
-   Input collimator: Slit of 80 x 8 x 0.5 mm.
-   Sensor: Opening of 9 mm x 17 mm.

9.2.   Results obtained

9.2.1.   Imagery by transmission X-rays

Fig. 66 gives an example of an image obtained in transmission. The duration of observation is 1 minute and the focal point 20 microns. The magnification used is 2 (pixel of 50 microns at the object level). The compression cracks are visible in Fig. 66 through darker areas. These dark areas indicate the existence of material that is denser than the surrounding material. This local densification of material at the compression crack location can be explained by buckling followed by very local crushing of the fibres. It is nevertheless important to note that there are other areas as dark in Fig. 66. These zones do not necessarily reflect the existence of heterogeneity due to mechanical stresses and stains. These zones could indicate natural heterogeneity present in wood (like knots, growth rings, inclusions).
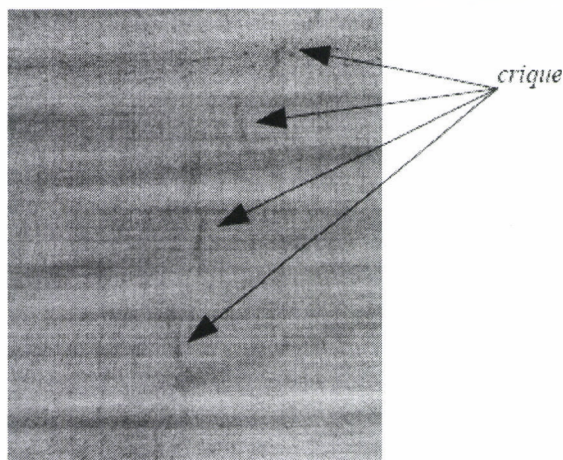
Fig. 66: Image obtained by transmission X-rays on the specimen B415-29 (front image, voltage: 35kV, Intensity: 400µA, big focus, duration: 1minute).

Cracks are sometimes visible in transmission but the contrast depends greatly on the orientation of the beam with respect to the fissure, and it may be necessary to take various views at different inclinations to ensure detection. In fact with respect to the detection of compression cracks, which are plane defects, X-ray imagery sensitivity to this type of defect depends greatly on crack orientation. The crack must be directed along the incident beam direction in order to ensure its detection. Further, the natural heterogeneity of wood can give rise to very strong contrasts on the image, this again depending on their orientation with respect to the beam.

9.2.2. *Measurement by X-ray under Compton diffusion*

The measurement is made under back scattering in order to simulate the on-site practical case. The complexity of the method arises from the fact that a compromise is required between the sharpness of the collimators (which defines its sensitivity to a small defect) and obtaining a sufficiently strong signal at the detector. The number of photons received is a compromise between the rate of diffusion and attenuation.
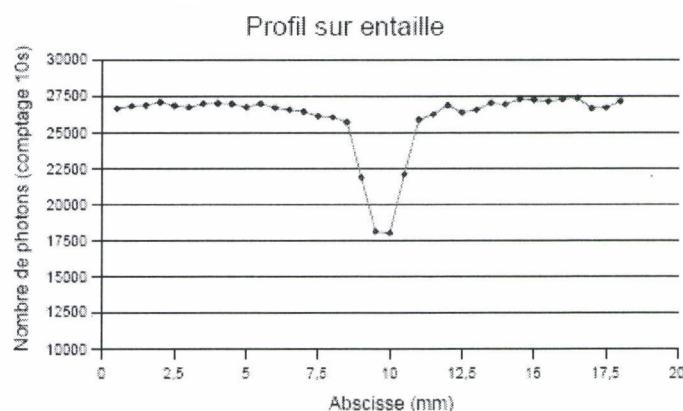
Fig. 67: Pattern of number of photons received under back scattering on a wood piece having a notch with an opening of 2 mm and depth of 5 mm.

B420-47

Scan start at 0 mm

B420-47
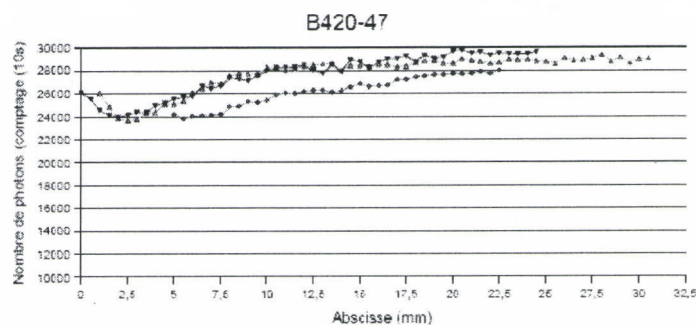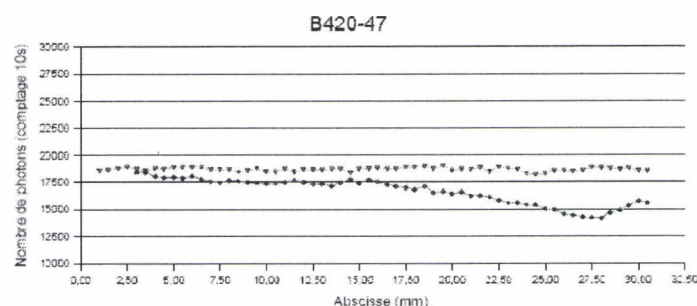
Scan start at 30 mm

Fig. 68: Pattern of number of photons back scattered along a line passing though the crack, on specimen B620-47. Several successive scans are carried out in the same direction and in the reverse direction. The drop in the number of photons at the beginning of the scan is not derived from the object. The crack is located around the 15 mm point.
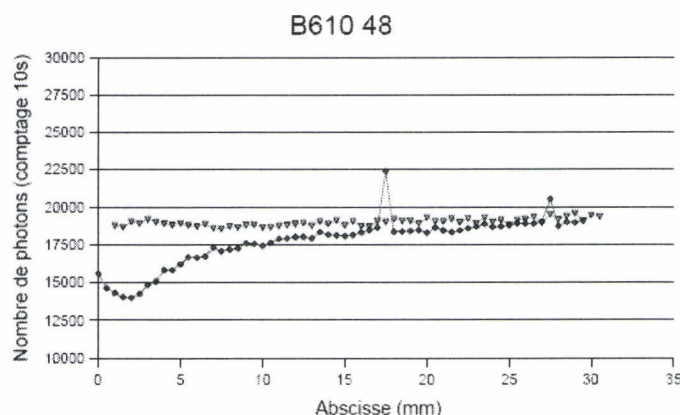
B610 48

Fig. 69: Pattern of the number of photons back scattered along a line passing through the crack on specimen B610-48. Two successive scans were made in the same direction.

Fig. 67 shows the pattern of the number of photons in back scattering on a piece of wood with a notch 2 mm wide and 5 mm deep. The notch is characterized by a drop in the number of photons received at the 10 mm position. This particular case, which does not relate to the specimens under study, is an example of a successful detection using back scattering.

Fig. 68 and Fig. 69 show the pattern of the number of photons back scattered along a line passing through the crack on specimen B620-47 and specimen B610-

48. The signal given by the wood is very weak. The sensitivity necessary to detect the existence of cracks was not reached. No significant fluctuation on the number of photons received is detected at the crack location.

A collimator with a finer output would allow the definition of a smaller measuring volume but the power currently available from the laboratory tube does not provide a strong enough signal. A more powerful tube would be required. A greater variation in the number of photons is also visible on several successive scans of the same component. This variation could be due to the tube itself (variation in focus position for example since the adjustment of the collimator in front of the tube is very critical) or due to the sensor. It therefore seems necessary (1) to be able to increase signal strength so as to increase sensitivity to a smaller variation in the number of photons, (2) to stabilise the measurement thereby ensuring good repeatability.

10. Ultrasound

10.1. Laboratory ultrasound testing with water as couplant

Study carried out by Laboratoire de Mécanique et d'Acoustique.

Laboratoire de Mécanique et d'Acoustique (LMA), CNRS, UPR-7051, 31 chemin Joseph-Aiguier, 13402 Marseille Cedex 20 (*http://www.lma.cnrs-mrs.fr/*).

10.1.1. Experimental protocol

An ultrasound scanner (Fig. 70) has been used so as to provide a variety of possibilities of examination in ideal laboratory conditions. Water is the couplant medium. The scanner consists of:

- A mechanical robot for handling ultrasonic waves (transducers) with 8 degrees of freedom (2 linear displacements in X, Y, Z and 2 probe/object concentric rotations).

- An electronic control bay for the robot movements.

- An acoustic signal emission, transmission and processing system.

- A computer for the synchronisation of displacements and acquisitions.
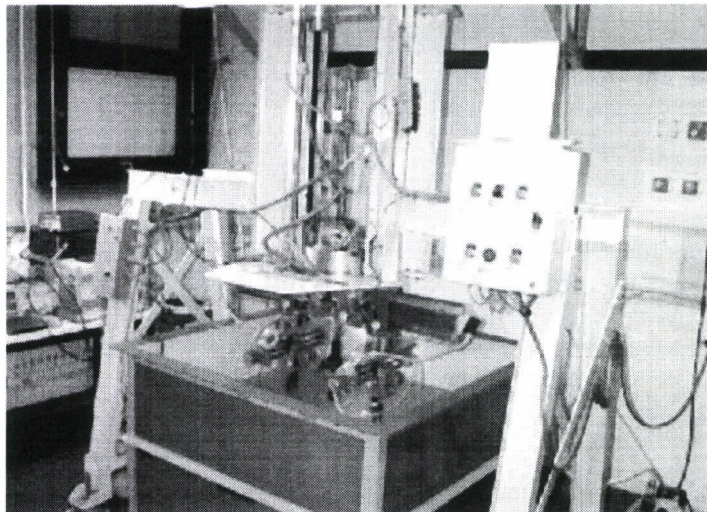
Fig. 70: View of ultrasound scanner at LMA (photos LMA).

The acquisition and processing system consists of the UTC-100 acquisition card (from EuroSonic) controlled by its EuroScan v3.04 software. This card is capable of accessing two transducers that can operate either in transmission or in reflection. It is also possible to connect a transmitter-receiver transducer working under reflection. The EuroScan software allows acquisitions and display in A, B and C-Scan.

10.1.1.1. *Normal reflection tests on specimens*

The orientation of the transducer (incident ultrasonic beam) makes an angle of 90° with the surface of the tested specimen (Fig. 71 and Fig. 72). Only one transducer is used, which operates simultaneously in transmission and reception.

The transducer used operates at 1 MHz and focuses at 90 mm. The associated wavelength is of the order of 1 to 5mm in wood (average wave velocity of 1500 m/s). The size of the cracks to be found varies between 3 and 5 mm deep. The wavelength used corresponds to the order of magnitude of the size of defect sought.
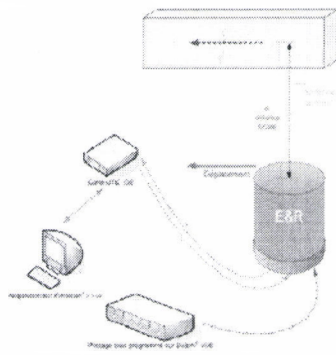
Fig. 71: Principle of ultrasound testing under normal reflection.
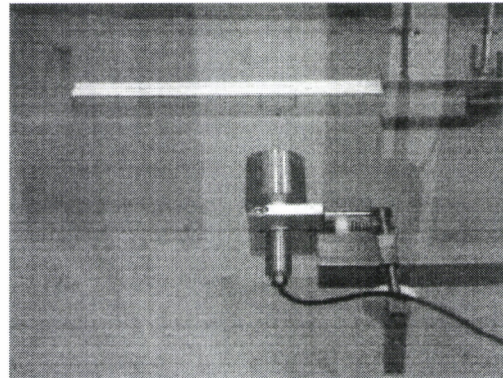
Fig. 72: Detail of an ultrasound test under normal reflection with water as couplant.

The test conditions are given below:

- Transmission frequency: 1 MHz.
- Sampling frequency: 20 MHz.
- Number of specimens: 1024.
- Resolution: 8 bits.

10.1.1.2. *Testing with variable incidence on a spar element*
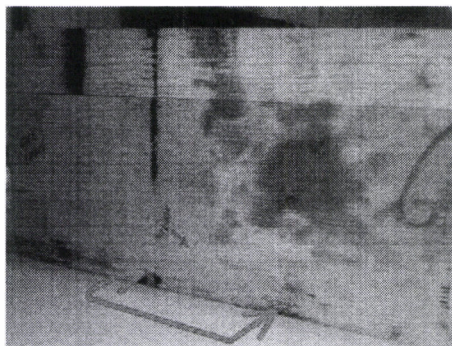
Fig. 73: Spar element of CAP10 tested through underwater type ultrasound (L x l x h = 312 x 156 x 60 mm). The red arrows show the inspected area.
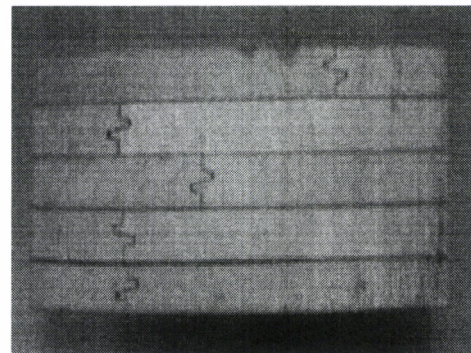
The spar element (Fig. 73) has been tested under normal incidence (Fig. 71) and oblique incidence of +20° and -20° with respect to the specimen surface (Fig. 74). Specimen scanning follows a linear trajectory of 120 mm on both sides of the crack zone.
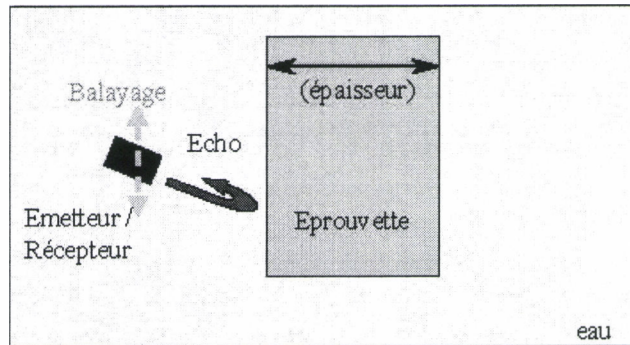
Fig. 74: Schematic diagram for oblique incidence ultrasonic acquisitions (+20° and -20°).

10.1.2. **Results of normal reflection on specimens**

10.1.2.1. *Interpretation of a normal reflection test in A-Scan*

In A-Scan representation, the amplitude of the ultrasonic signal received is displayed graphically as a function of time (Fig. 75).
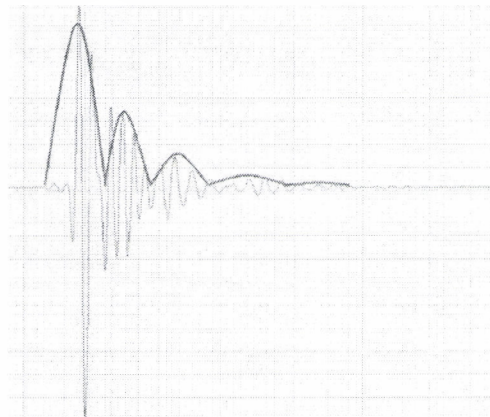
Fig. 75: Representation of ultrasound test in A-Scan (B 615/5).

In the example in Fig. 75, the received signal lasts for approximately 17μs, equivalent to an inspected depth of approximately 13 mm. The rear interface of the specimen, the wood-water interface, is then not discernable. Neither are the interfaces of the bonding planes distinguished in A-Scan. Five wave packets are visible in the example in Fig. 75, with an average duration of around 4μs (i.e. 3 mm). These packets seem to correspond to the reflections induced by the growth rings, the thickness of which varies between 2 and 3 mm (Fig. 76).
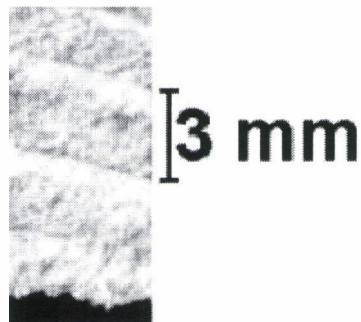
Fig. 76: Specimen B615/5 across the grain.

10.1.2.2. *Interpretation of a Normal Reflection test in B-Scan*

Fig. 77 shows the result obtained by a normal reflection test in B-Scan. In this figure, time is shown on the ordinate axis (equivalent to the sounding depth). The time elapsed during the test is shown on the abscissa axis (equivalent to the depth examined under the specimen surface). The amplitude of the signal received is represented in levels of grey (signals are not rectified).
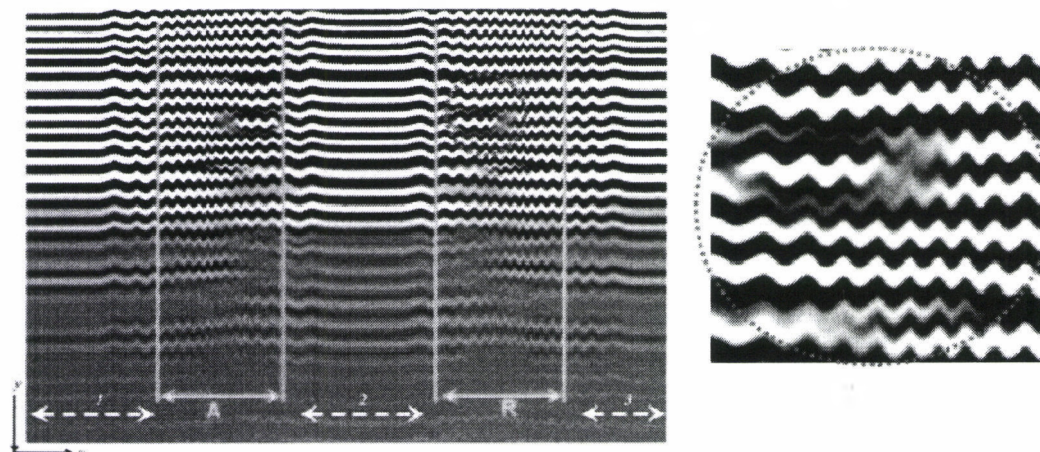
Fig. 77: Example of a to and fro B-Scan representation on a crack zone.

Zones A and R in Fig. 77 represent the to and fro movement around the crack zone. Zone 1 corresponds to the initialisation of the test where motor vibration (acceleration and displacement) is shown by the oscillations. Zone 2 corresponds to the transition or the pause between the to and fro paths. There is no sensor movement . Zone 3 corresponds to the slowing down and the end of the test. The variations viewed in the form of waves correspond to the acceleration of the motor shown here by the vibration of the specimen and or the sensor itself.

The blue colour zone in Fig. 77, which represents an anomaly (acoustic impedance failure) is a zone with a structural defect; namely a compression crack in this example. Since ultrasound propagation velocity in wood is known, it is possible to evaluate the depth corresponding to the defect (4 mm deep in this case, Fig. 78).
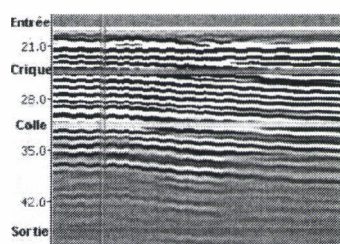
Fig. 78: Time-depth equivalence for normal reflection test in B-Scan.

10.1.2.3. *Summary of results obtained under normal reflection*

In total, 8 specimens exhibiting a crack (A415/6, B430/110, B430/47, B530/27, B530/49, B520/29, B620/29 and B615/92) and 2 undamaged specimens (SIV and SV) were tested. Analysis of specimen B520/29 is shown here as example. The image of this specimen is shown in Fig. 79.

It is important to mention that image analysis of this specimen did not show the existence of a crack, since it was too fine to be viewed by the scanner.
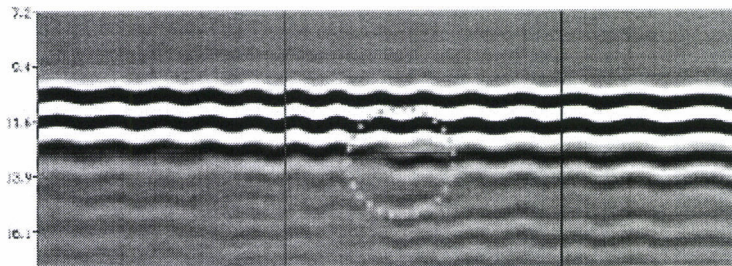
Fig. 80: B-Scan mapping of specimen B520/29.
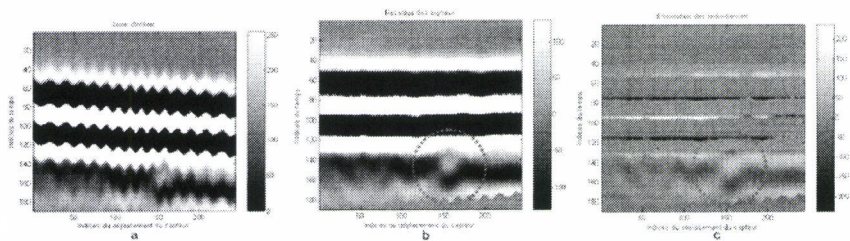
Fig. 81: Display of the B-Scan zone chosen (a), signal resetting (b) and elimination of redundancies (B520/29).

The B-Scan cartography of the specimen B520/29 is shown in Fig. 80. The crack, circled here by a dotted line, shows a break in the image pattern at a depth of 2.23 mm. The depth of the crack observed visually on the sides of the specimen is 2mm to the left and 4 mm to the right. Fig. 81 shows the stages of B-Scan image processing to highlight the pattern break; the redundancy elimination algorithm still needs to be improved (Fig. 81, c).

Fig. 79: Digital image of specimen B520/29.

For each specimen, crack depth has been noted visually on the side faces (as far as possible from the digital images). Crack depth could be estimated from the analysis of B-Scan images obtained in normal reflection. Fig. 82 shows the reported depths for each specimen. The depths obtained in B-Scan imagery are consistent with the depths measured directly on the specimens.

Comparatif des profondeurs mesurées à vue de profil et expérimentalement
en BScan
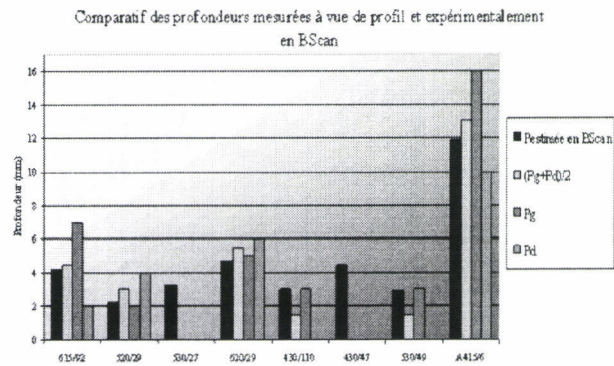
Fig. 82: Comparison of depths measured visually on each face and by analysis of the B-Scan images (Pg: left component, Pd: right component).

10.1.3. Results under variable incidence on a spar element

Fig. 83 shows the B-Scan mapping obtained with signal saturation. The zone defined by the red arrows (zone from +10 to -25 mm) shows a break in the B-Scan image with respect to the crack free zone that appears more uniform. Most probably, this modification of the echo (highly visible particularly at position -20mm in Fig. 84) reflects the existence of a significant modification of the surface condition of the tested element.
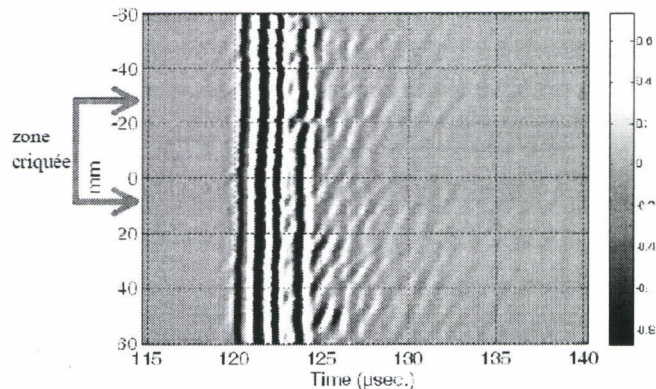
Fig. 83: B-Scan mapping of the spar element obtained under normal reflection with saturation.
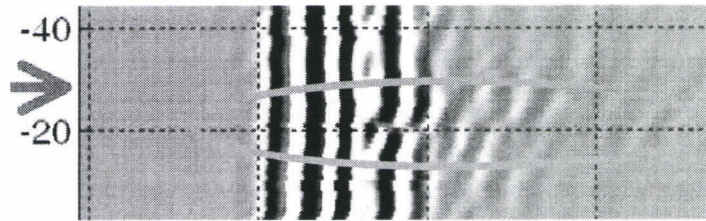
Fig. 84: Detail of a break in the B-Scan image of Fig. 83.

Fig. 85 and Fig. 86 show the B-Scan mapping obtained in reflection under oblique incidences (+20° and -20°) without saturation. Taking into account the angle of incidence given to the probe, the crack zone is no longer at the origin of the scan. As in the previous test (Fig. 83), the zones marked with arrows (±20 to ±40 mm) show a variation of the B-Scan image (intensification of the dynamic of colour coding). It is possible that the modification of the echo (absence of specular echoes thus echoes related to propagation in the test specimen, surface wave, or guided wave), indicates a greater modification in thickness and has a relationship with the crack observed in the same zone. Optimal measurements could be obtained by successive scans using a range of incidence angles.
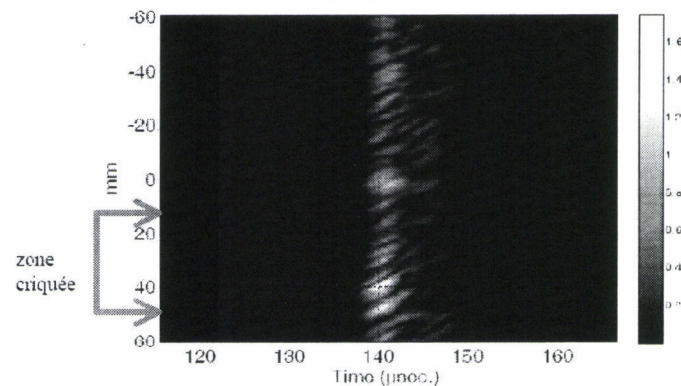
Fig. 85: B-Scan mapping of the spar element obtained in reflection under oblique incidence (+20°) without saturation.
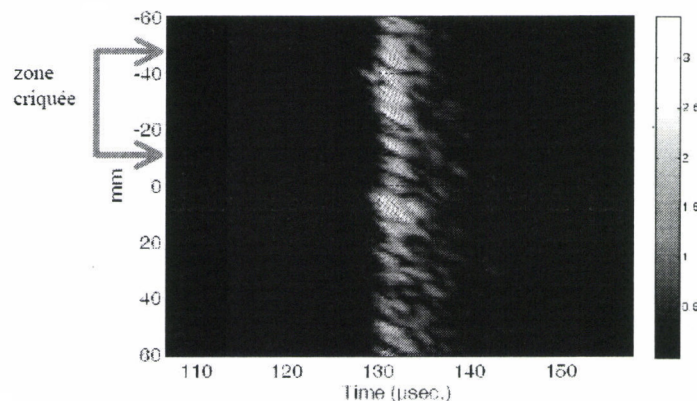
Fig. 86: B-Scan mapping of the spar element obtained in reflection under oblique incidence (-20°) without saturation.

At the current state of the laboratory study, ultrasonic analysis can provide important elements in the non-destructive testing of spar-type composite structures. Although not yet capable of providing a definitive answer or to be of use in a more industrial context (prototyping), the ultrasound analysis carried out shows advantages in the detection of compression cracks. At 1 MHz, in B-Scan imagery (impedance contrast image), detection appears possible in a water bath.

Consideration must now be given to a more complete and systematic approach to ultrasound compression crack detection, which would combine significant studies at the wood component level as well as on bonded laminated structures, as well as tests to be implemented in an industrial context. This preliminary work will have to extend to more in-depth studies so that serious consideration can be given to the industrial use of an ultrasound protocol. At the present state of knowledge, it would be dangerous to develop an industrial prototype or even tests based on these results alone whether they are academic or industrial. This danger arises from the adaptability as well as the reproducibility of the protocol, and the ultimate risk of an inaccurate check.

10.2. Ultrasound testing with elastomer couplant

Study carried out by EURO PHYSICAL ACOUSTICS.

EURO PHYSICAL ACOUSTICS SA -27, rue Magellan -ZAC des Portes de Sucy -F 94373 SUCY-EN-BRIE CEDEX - Site internet: www.epandt.com

10.2.1. Experimental protocol

10.2.1.1. Description and characteristics of the ultrasound equipment

The acquisition chain consists of sensors, preamplifiers and the acquisition system. This chain is incorporated in a portable reference system "Pocket AU" (Fig. 87, a). The "Pocket AU" has the advantage of integrating an ultrasound generator capable of transmitting a train of square waves programmable in fixed or wobbulated frequency thereby making available a source of significant power.
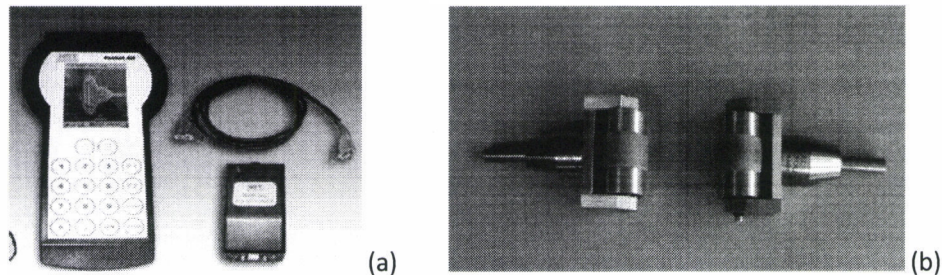
Fig. 87: View of ultrasound transducers RS30 (a) and" Pocket AU" the portable system used (b).

The E/R ultrasound transducers are cylindrical in shape and are incorporated in a hand-held manipulator. The transducers are fitted with a couplant which ensures impedance matching between the wood structure and the piezoelectric elements (Fig. 87, b). This couplant consists of an elastomer. The appropriate frequency range for wood and the couplant lies between 200 kHz and 400 kHz.

Details of equipment setting and characteristics are given below:

—	Acquisition system:	Pocket AU
—	Number of channels used:	2 channels (transmission and reception).
—	Type of sensors:	RS30.
—	Resonance frequency (kHz):	200 – 400.
—	Preamplifiers:	Internal amplification with variable gain.
—	Preamplifier filters (kHz):	20 – 1200.
—	Ultrasound generators:	Sinusoidal waveform, 20V CC.

10.2.1.2.   Measuring method

The operator sweeps the scanner manually across the specimen and views in real time the A-SCAN signal on the screen of the "Pocket AU". This scanner is fitted with 2 x RS30-UT sensors and the measurement is made in tandem mode (transmitter and receiver) on the same side of the specimen (Fig. 88). If the ultrasonic propagation path is disrupted by a defect, the signal form will be modified.
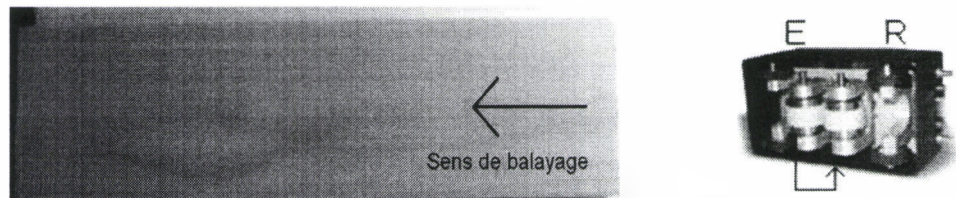
Fig. 88: Schematic diagram of the ultrasound testing and details of manual scanner.

10.2.2.   Results

10.2.2.1.   Signal display in A-SCAN mode

Fig. 89 gives an A-SCAN representation of the transmitted signal for specimen 620_10. The ultrasound signal propagates in the material without any significant attenuation. The intrinsic characteristics of elastomer type sensors explain the signal form that is relatively less dampened. 5 to 6 successive lobes can be seen on this A-SCAN over the 400 µs of propagation of the ultrasound signal.
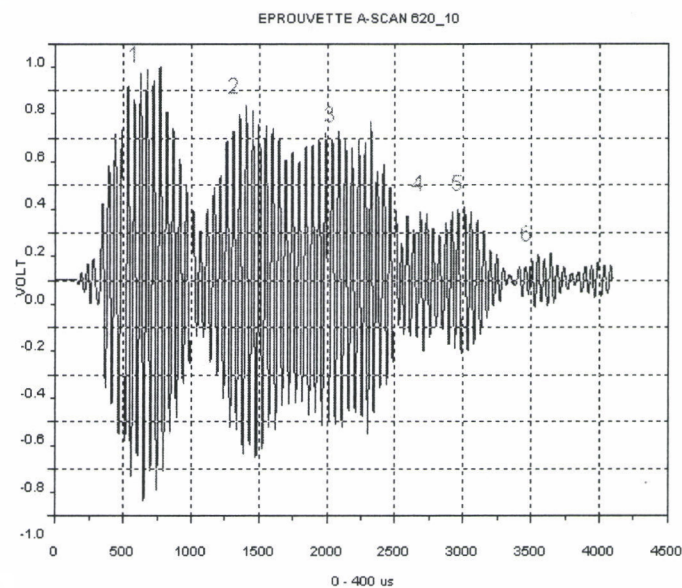
Fig. 89: A-SCAN ultrasound signal obtained on a wood specimen (reference 620/10).

The transducers are held on the surface with a constant pressure and the gain is adjusted automatically for each specimen. The specimens are theoretically considered to have the same characteristics but a comparison of the A-SCAN signals obtained highlights significant differences in the signal at the level of the last lobes.

The natural heterogeneity of wood (knots, density variation etc.) is reflected in the variations of the A-SCAN signal for the same specimen (based on the inspected zone). Signal attenuation is not constant for each specimen, which imposes different gain settings for each reference.

It therefore seems difficult to define a reference gauge block for this study. A B-scan type representation also appears to be necessary in order to facilitate result interpretation.

10.2.2.2.   _Signal viewing in B-scan mode_

The Pocket AU generates C-scan maps for a specimen but the geometrical form of the specimens and the overall dimension of the scanner do not allow this type of 2D mapping. To obtain a B-scan, a full scan of the specimen is required as well as the storage of each A-SCAN (manual operation) as and when the scanner advances. The files stored in memory are then compiled and traced so as to obtain a concatenation of all the A-SCANS (Fig. 90).

-A-SCAN no. 20-   -Concatenation of 55 A-SCAN-
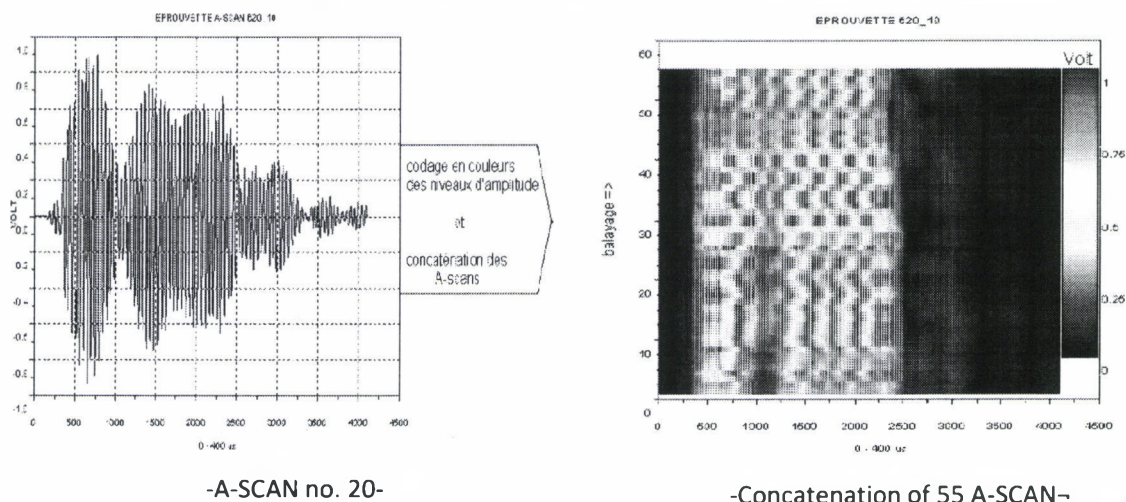
Fig. 90: Principle for obtaining a B-scan map for specimen 620/10.

Each horizontal line of the resultant B-scan (Fig. 90) thus corresponds to an A-SCAN, the amplitudes of which are colour-coded. The abscissa axis of the B-scan corresponds to the length of the A-SCAN recorded (400 μs) and the ordinate axis to the chronological storage order of the A-SCANS. Fig. 90 shows a B-scan carried out on specimen 620/10 by recording 55 successive A-SCANs. The signal amplitudes are colour coded (from blue to red for minimum and maximum).

A total of 15 specimens were mapped in B-Scan. One specimen did not contain any damage and was tested on both faces. The other specimens all showed significant compression cracks at various positions. Fig. 91 shows the mapping of the defect free specimen 620/1. Fig. 92 shows the detection of a defect on the specimen 530/1. All the maps obtained however show different patterns and the interpretation of B-Scan mapping is very difficult.
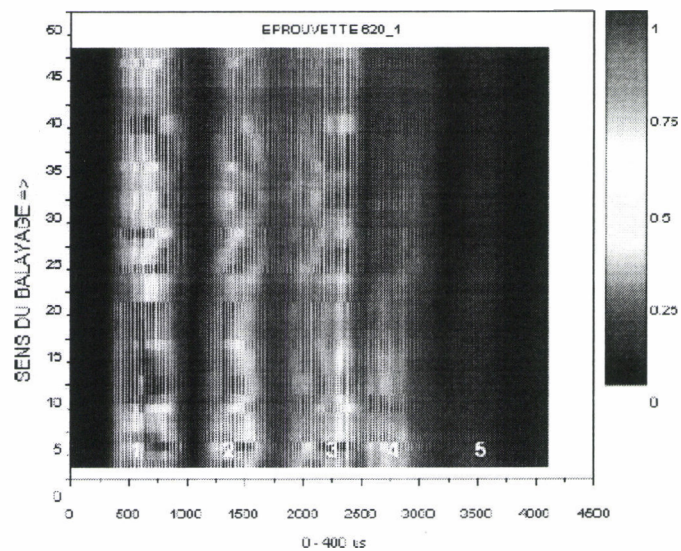
Fig. 91: B-scan mapping of the test specimen 620/1.
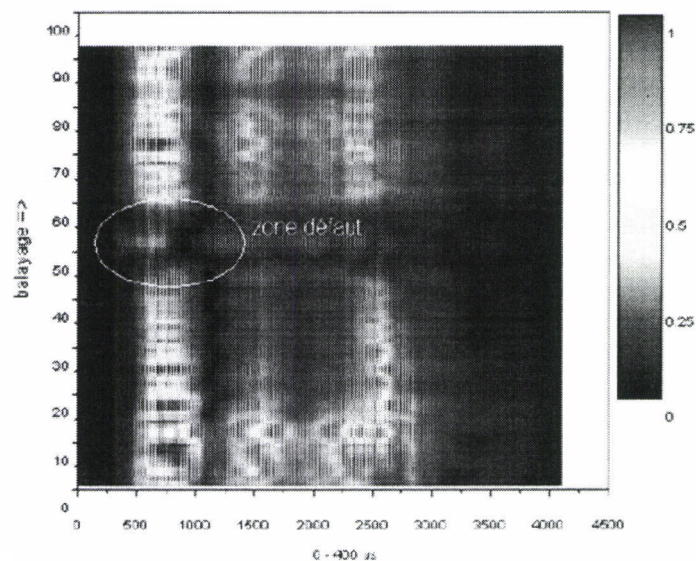
Fig. 92: B-scan mapping of the specimen 530/1.

Specimen reference	Defects visible at the surface	Detection by ultrasound
620/1	no	no
620/1 (other face)	no	no
520/4	yes (large size)	no
520/3	yes (large size)	yes
415/4	yes (distributed)	no
415/5	yes (distributed)	no
512/2	yes (average size)	no
530/1	yes (distributed)	yes
620/2	yes (small size)	no
420/4	yes (distributed)	no
420/3	yes (small size)	no
620/5	yes (distributed)	yes
430/6	yes (distributed)	no
430/3	yes (distributed)	yes
630/2	yes (small size)	no
630/3	yes (distributed)	no

Table 5: Summary of results obtained by ultrasound testing with elastomer couplant.

Table 5 gives the detection results obtained on the 15 specimens tested using the elastomer couplant ultrasound method with the Pocket AU system (observation of B-Scan maps). Out of 16 tests, 4 detections were possible and no detection was made on the reference specimen. None of the successful detections concerned small size cracks. One large size crack was not detected. The results obtained do not warrant full validation for the method with respect to problems of interpretation of the ultrasound signal associated with the heterogeneity of wood.

On account of the significant variations of the amplitude of the recorded signal with the same amplification, on different specimens, no reference specimen can be defined, as is done in most NDT applications. The structure of wood (knots, annual growth rings etc.) greatly disturbs the A-SCAN signal and has made the identification of defects on B-scan maps impossible in some cases.

However, it would certainly be interesting to obtain a B-scan map on the same wood specimen for three mechanical conditions: non-compressed, compressed without damage and compressed with damage. In fact, by comparing these 3 maps, an evaluation can be made on the one hand about the influence of the compression operation (material history) on ultrasound signal and on the other, the possibility of testing these assemblies even without absolute references.

10.3. Ultrasound testing of a CAP10 wing during 4 point bend test

Study undertaken by EURO PHYSICAL ACOUSTICS.

EURO PHYSICAL ACOUSTICS SA -27, rue Magellan -ZAC des Portes de Sucy -F 94373 SUCY-EN-BRIE CEDEX - Site internet: www.epandt.com

10.3.1. Experimental protocol

10.3.1.1. Description and characteristics of the ultrasound equipment

Ultrasound testing of a static test on a CAP10 wing was carried out in addition to testing using acoustic emission (p. 87). The ultrasound measurements did not interfere with acoustic emission testing. Ultrasound testing was carried out periodically during the course of the static test – after each relaxation on the structure at rest - and five ultrasound signatures were recorded until wing failure:

- – AU0: Reference shot on a wing at rest.
- – AU1: Increase in 3 successive plateaus up to 2700 N followed by relaxation.
- – AU2: Rapid increase to 6000 N followed by relaxation.
- – AU3: plateau at 2700 N and rapid increase to 12000 N followed by relaxation.
- – AU4: plateau at 2700 N and rapid increase to 18000 N followed by relaxation.
- – AU5: plateau at 2700 N and rapid increase to 24000 N followed by relaxation.

The ultrasound detection system used can be divided into two parts: one component identical to the acoustic emission system and a second component consisting of an ultrasound transmitter. The acoustic emission component consists of sensors with integrated preamplifiers and a multi-channel acquisition system (PCI-8 card). The sensors are coupled to the structure by grease and are held by adhesive tape. The ultrasound component consists of an arbitrary signal generation card (card ARB14150). The advantage of this device is its high transmission power and its ability to generate a selected input signal. This card also provides a useful synchronisation output (TTL) for recording the time that the generator fires.
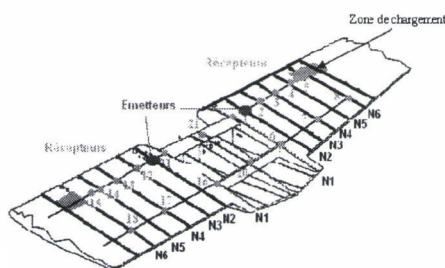
Fig. 93: Location diagram of ultrasonic sensors transmitters and receivers.
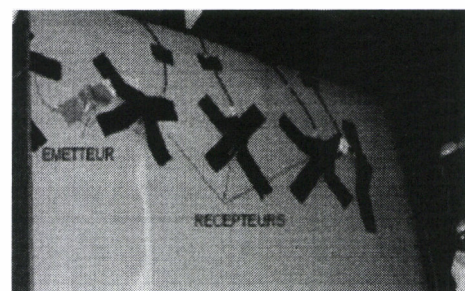
Fig. 94: View of ultrasound transmission and reception sensors fixed on the wing.

The reception sensors are placed on the skin at the joints between the ribs and spars in order to have continuity between the different propagation media (Fig. 93 and Fig. 94). Both low frequency sources are positioned on the skin adjacent to ribs N2 for the 2 wing elements. In this case, the sensors used for ultrasound testing are the same as those used for acoustic emission testing. The wave speed in the material is evaluated at 2500 m/s. The setting details and characteristics of the equipment are given below:

Transmission

–	Ultrasound generator:	Card ARB 14- 150
–	Transmitter transducers – Number:	R15 (150 kHz) - 2 transmitters
–	Type of transmission:	Sinusoidal 150 kHz (10V)

Reception

–	Acquisition system – N. channels:	SAMOS – 64
–	Number of channels used:	18
–	Type of sensors – Number:	R6I – 12 and R15I – 6
–	Resonance frequency (kHz):	60kHz (R6I) and 150kHz (R15I)
–	System filters (kHz):	20 – 400
–	Preamplifiers (model):	Integrated with Gain (dB): 40
–	Acquisition threshold (dB_{EA}: Ref. 1 µVolt/Sensor):	40

10.3.1.2. *Measuring method*

The ultrasound testing method is based on the transmission and reception of a low frequency ultrasonic wave in a structure. This technique can be considered as a local or global method depending on the protocol chosen:

- Local method: the transmitter and receiver couple is displaced automatically or manually on the surface of the structure. This inspection method has been used with the Pocket AU system for carrying out tests on test specimens.
- Global method: the transmission and the reception take place with one or more transducers based on the signal attenuation and the geometry of the structure. The transmitters and receivers connected to the structure, remain fixed for the tests.

The process consists in following the evolution of the ultrasonic waveform in the structure during its propagation (Fig. 95).

This testing can be carried out in the standard manner with respect to the time of propagation but also with respect to the energy.
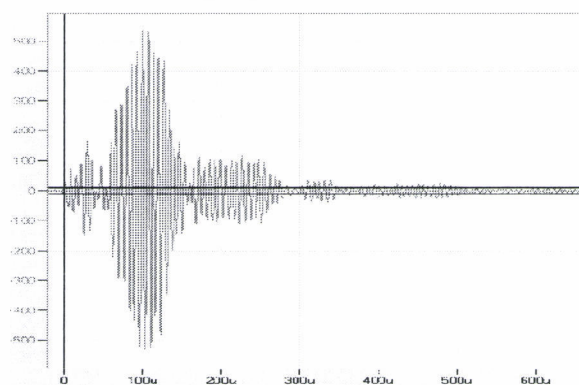
Fig. 95: Waveform obtained by ultrasound testing.

10.3.2.   Results
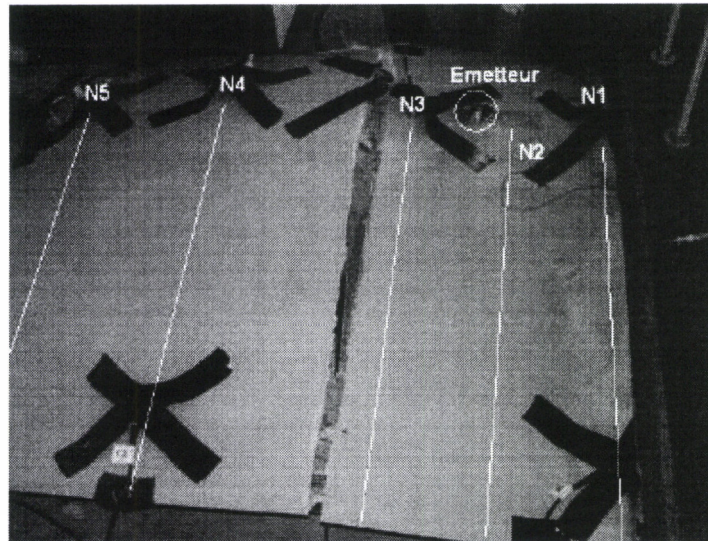
Fig. 96: View of the left wing after failure.

The failure of the left wing (Fig. 96) occurred during the last AU5 load. The evolution of the propagation time between the transmitter and the receivers, coupled on the ribs, after each load had not shown any significant variation during the test.

From an analysis of the parameters extracted during testing, it was possible to identify the energy of the waveform as a parameter discriminating the various ultrasound shots. The levels of energy recorded during the shots, after failure of the wing (with reference to AU5) are not representative since sensor coupling is no longer validated after failure.
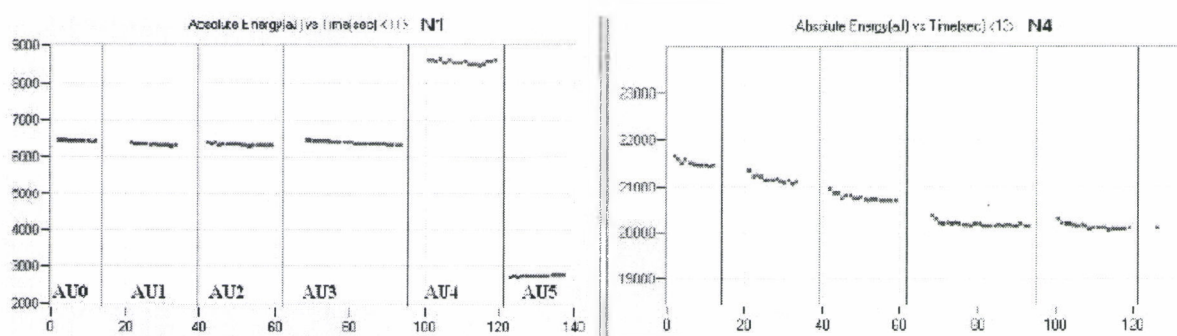
Fig. 97: Energy of signals measured during the static test for the left wing.
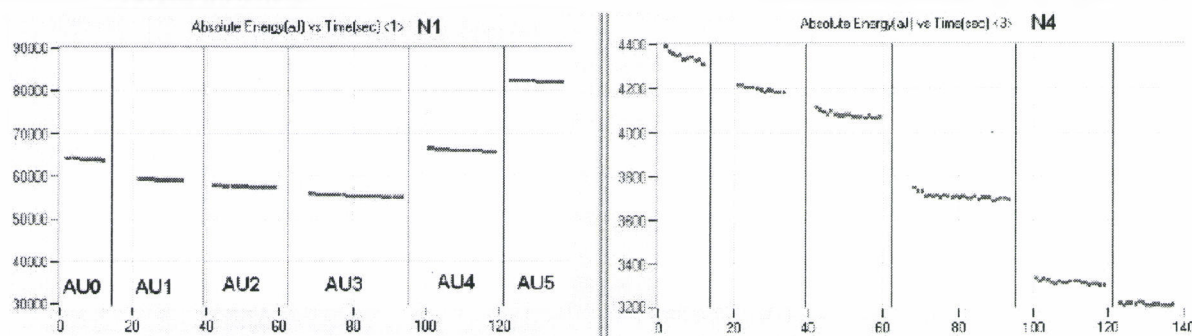
Fig. 98: Energy of signals measured during the static test for the right wing.

The analysis was made on ribs 1 to 5 for both parts of the wing. Only the results obtained with receivers N1 and N4 are shown (Fig. 97 and Fig. 98) and these show a break in the evolution of energy between times AU3 - AU4 for N1 and AU2 – AU3 for N4. This break, according to the receivers N1, is reflected by a sudden increase while the tendency had been decreasing and, for receivers N4, it is reflected by a sudden jump during energy decrease. It is however impossible to determine the location of failure on the wing. Thus ultrasound transmitters - receivers coupled to the wing skin - would enable the detection of a structural modification to the skin but not to the spar.

11. Acoustic emission

Studies carried out by EURO PHYSICAL ACOUSTICS.

EURO PHYSICAL ACOUSTICS SA -27, rue Magellan -ZAC des Portes de Sucy -F 94373 SUCY-EN-BRIE CEDEX - Site internet: www.epandt.com

11.1. Testing by acoustic emission for testing axial compression on wood specimens

11.1.1. Experimental protocol

11.1.1.1. Axial compression test

A total of 34 test specimens were tested in axial compression until failure (NF B 51-007, Sept. 1985). The test rig is shown in Fig. 99. The characteristics of each test specimen are described in Table 6. The location of the cracks in this table is obtained by visual observation and can only be used to subsequently compare the location of the initial cracks with respect to the final failure. The letters A, B, C, D and E refer to the division of the length into five zones (Fig. 100).
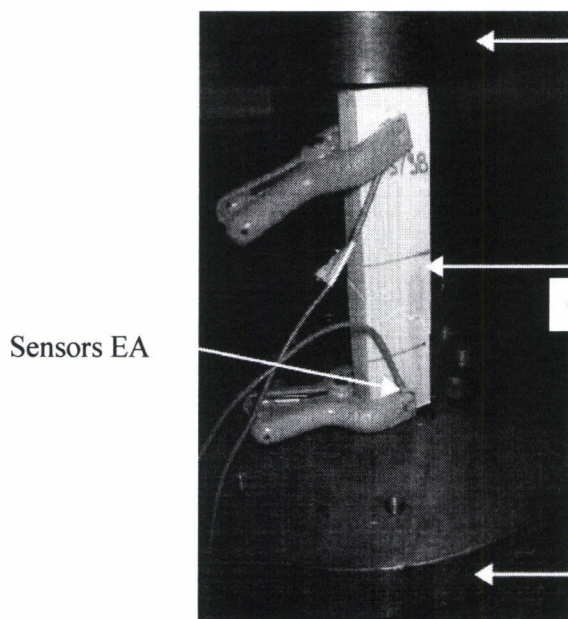
Fig. 99: Axial compression test tested by Acoustic Emission.
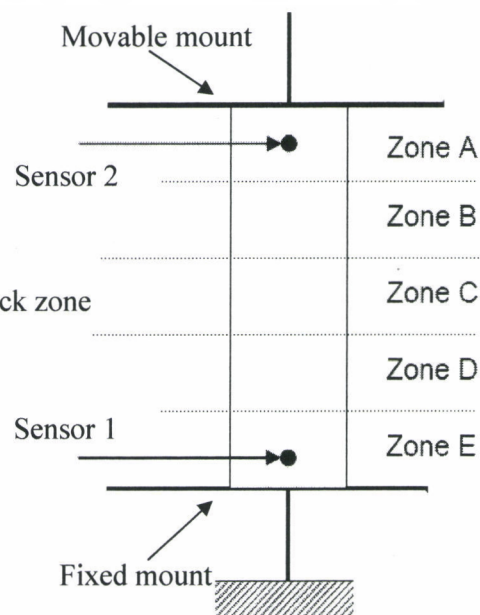
Fig. 100: Location zones on the specimens.

Batch no.	Test specimen no.	Crack location before compression
1	B410 / 37	A-B border
	B510 / 27	E
	B610 / 57	C
	S1	Sound test specimen
2	B415 / 38	D
	B415 / 47	D
	B415 / 56	C-D border
3	B515 / 23	C-D border
	B515 / 71	C
4	B615 / 73	B-C border
	B615 / 92	B-C border
	S3	Sound test specimen
5	B420 / 16	C
	B420 / 38	B-C border
6	B520 / 29	B-C border
	B520 / 47	B-C-D (skewed crack)
	B520 / 56	C
7	B620 / 29	2 cracks: C+D
	B620 / 38	2 cracks: C+B
	B620 / 56	C + B-C border (skewed crack)
	S4	Sound test specimen
8	B430 / 29	C
	B430 / 38	C
	B430 / 47	2 cracks: C+B
	B430 / 56	C
	B430 / 110	C
9	B530 / 16	C
	B530 / 27	C
	B530 / 38	No crack but delamination (D+C+B)
	B530 / 49	C
	B530 / 510	C
10	B630 / 37	C
	B630 / 510	C
	S5	Sound test specimen

Table 6: Specimen characteristics.

11.1.1.2. *Equipment used in Acoustic Emission*

A PCI-2 acquisition card in a micro-chassis driven by a portable computer was used for these tests. The sensors were chosen based on the experience acquired by EPA in the field of damage testing for structures in wood and composites. The acquisition chain consisted of sensors, preamplifiers and the acquisition system. Real time acquisition and analysis was provided by AEWIN software PCI-2 v.3.20. The sensors were coupled to the test specimens with grease and held in place using clamps.

The sensors were placed at the ends of the test specimens on the side of the pre-damaged specimen so that the testing zone was as large as possible. All specimens showed cracks except S1, S3, S4 and S5, which were declared as sound but which might display natural heterogeneity. Sensor 2 was always located on the side of the upper mobile mount. Sensor coupling was validated by the source Hsu-Nielsen (NF EN 1330-9) (2H Ø 0.5 mm pencil lead fracture) at 20 mm from each sensor. Coupling was considered to be optimal when the standard deviation of the different amplitudes detected by each sensor was no greater than 3 dB_{EA}. The speed of the wave in the material was also evaluated with the help of the Hsu-Nielsen source. The speeds measured varied from 5900 m/s to 6300 m/s with most being around 6000 m/s. The wave velocity for each test specimen was subsequently set at 6000 m/s.

The experimental conditions under Acoustic Emission are given below:

- Acquisition system-Number of channels: chassis and card PCI-2–2
- Number of channels used for the test: 2
- Type of sensors – Number: Nano 30 – 2
- Resonance frequency (kHz):   300
- System filters (kHz):   1 – 3000
- Preamplifiers (standard):   2/4/6 with Gain (dB): 40
- Frequency range (kHz):   20 – 1200
- Acquisition threshold (dB_{EA}: Ref. 1 µVolt/Sensor):   30

11.1.2. Results

11.1.2.1. *Testing of compression testing by Acoustic Emission*

A testing example is given in Fig. 101 for specimen B410/37 of batch 1. For this specimen, the distance between the sensors was 75 mm. In order to filter ambient noise, the results take into account only bursts with amplitudes greater than 40 dB_{EA}.
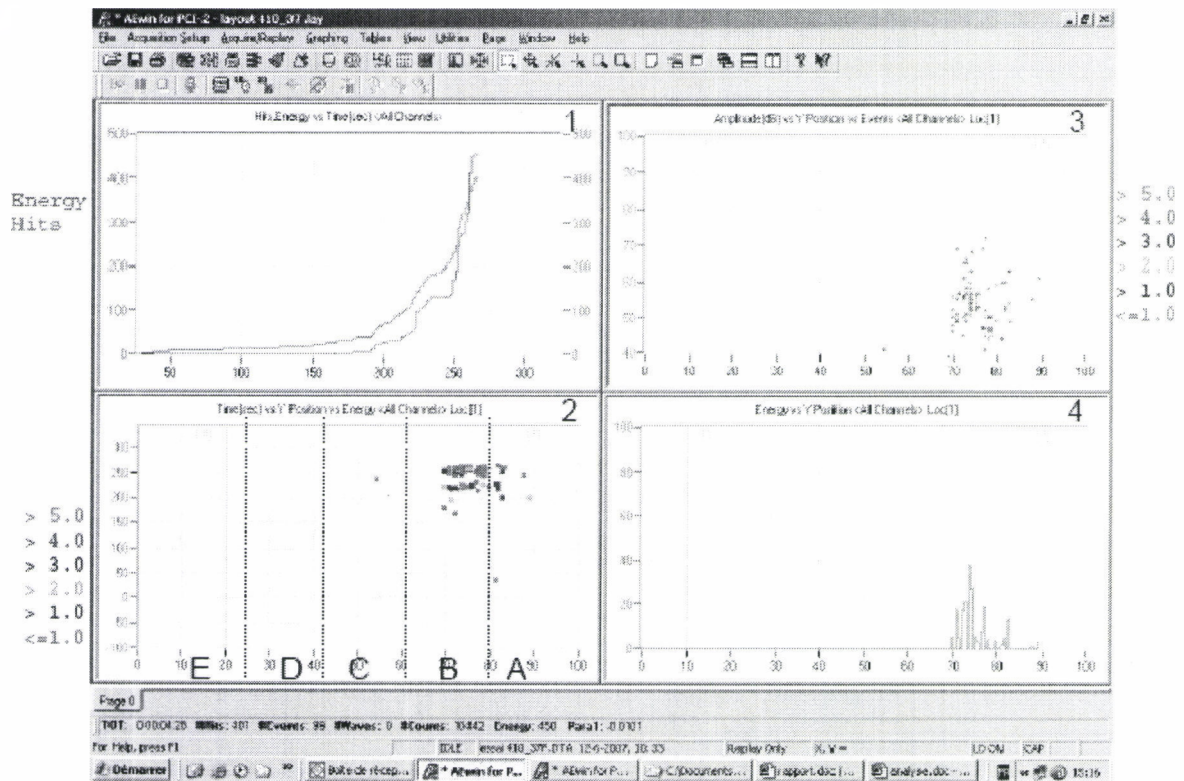
Fig. 101: AE activity and location of events-test specimen B410/37.

Fig. 101 is divided into 4 parts:

- Component 1: Shows the emissivity in the test specimen. The red curve represents the activity, i.e. the number of cumulative bursts and the green curve represents the intensity, i.e. the cumulated energy. This relative energy has no dimension.

- Component 2: Shows the position of events as a function of time (ordinate axis). The two sensors are represented by their number in green at the top of the graph. The colour scale represents the energy of bursts.

- Component 3: Shows the distribution of the amplitude of the events located between two sensors. The colour scale represents the number of events.

- Component 4: Shows the distribution of the cumulated energy located between the two sensors.

In this example, there is average acoustic activity with a few bursts right from the beginning of the test. The intensity shows a first point of inflexion after approximately 160 s of testing followed by a second at around 250 s. Very few events are located before 200 s and the events are concentrated in zones A and B, which corresponds to the location of the initial crack and that of the failure in the test specimen.

The results obtained are summarised in Table 7. The letters A, B, C, D and E refer to locations shown in Fig. 100. The failure is located in most cases at the level of the crack initiated during specimen manufacture. The cracks thus formed are hence truly areas of mechanical weakness (failure initiation). In most cases, the damage is correctly located. In fact, out of the 34 tests, 5 locations failed. Three failures were due to a collapse of the specimen on one edge; this type of breakage must not be taken into account for analysis.

Batch	Test specimen	Position of cracks before compression	Observation of failure	Location of damage by EA	Remarks
1	B410 / 37	A-B border	Along initial crack (A-B border)	A-B border	Nothing found
	B510 / 24	E	Along initial crack + small side detachment (zone C)	E→C	Nothing found
	B610 / 57	C	Along initial crack (C)	C + B→A	2 zones of damage: -C (rupture) –displacement of events from C towards A
	S1	Sound	A	A	Very few events located on account of continuous emission
2	B415 / 38	D	Along initial crack (D)	D→E	Nothing found
	B415 / 47	D	Double buckling (B + D)	D + B + E	Nothing found
	B415 / 56	C-D border	Along initial crack (C-D border)	C-D border	Nothing found
3	B515 / 23	C-D border	Skewed fracture along knot (A)	B + A + C→D	Nothing found
	B515 / 71	C	Following initial crack (C)	C	Nothing found
4	B615 / 73	B-C border	Following initial crack (B-C border)		No location on account of continuous emission
	B615 / 92	B-C border	Collapse of edges (A)	B	Low location since the EA sources were located outside the array
	S3	Undamaged	Collapse of edges (A + E)	Diffuse	Low location since the EA sources were located outside the array

5	B420 / 16	C	Following initial crack (C)	C	Nothing found
	B420 / 38	B-C border	Following initial crack (B-C border)	B-C border	Nothing found
6	B520 / 29	B-C border	Following initial crack (B-C border)	B-C border	Nothing found
	B520 / 47	B-C-D (skewed crack)	Following initial crack (B-C-D)	C + B + D	Nothing found
	B520 / 56	C	Following initial crack (C)	C + E + A	Good location of the crack + location of events close to the sensors
7	B620 / 29	2 cracks C+D	Along one of the initial cracks (C)	C + E	Bad location due to continuous emission
	B620 / 38	2 cracks C+B	Along the two initial cracks (C + B)	C + D + B	Nothing found
	B620 / 56	C + B-C border (skewed crack)	Following initial crack (C + B-C border)	C + B-C border + A	Good location of the crack + location of events close to sensor 2
	S4	Sound	Collapse of edges (A)	A-B border	Low location since the EA sources were located outside the array
8	B430 / 29	C	Fracture opposite side (A-B border)	A + B	Nothing found
	B430 / 38	C	Following initial crack (C)	C + B-C border	Nothing found
	B430 / 47	2 cracks B + C	Fracture opposite side (A + B) + small fracture (C)	A→B→C	Nothing found
	B430 / 56	C	Following initial crack (C)	C	Nothing found
	B430 / 110	C	Following initial crack (C)	C	Nothing found
9	B530 / 16	C	Following initial crack (C)	C	Nothing found
	B530 / 27	C	Following initial crack (C)	C + C-D border	Nothing found

	B530 / 38	No crack but delamination (D+C+B)	Fracture opposite side (C)	C + B-C border	Nothing found
	B530 / 49	C	Following initial crack (C)	E + C	Good location of the crack + location of events close to sensor 1
	B530 / 510	C	Following initial crack (C)	C	Nothing found
10	B630 / 37	C	Following initial crack (C)	C	Nothing found
	B630 / 510	C	Following initial crack (C)	C	Nothing found
	S5	Sound	C-D border	C-D border	Nothing found

Table 7: Summary of axial compression tests by Acoustic Emission.

11.1.2.2. *Estimation of the damage and failure by Acoustic Emission*

Fig. 102 shows a typical curve showing stress as a function of time during an axial compression test. Fig. 103 shows the acoustic activity.
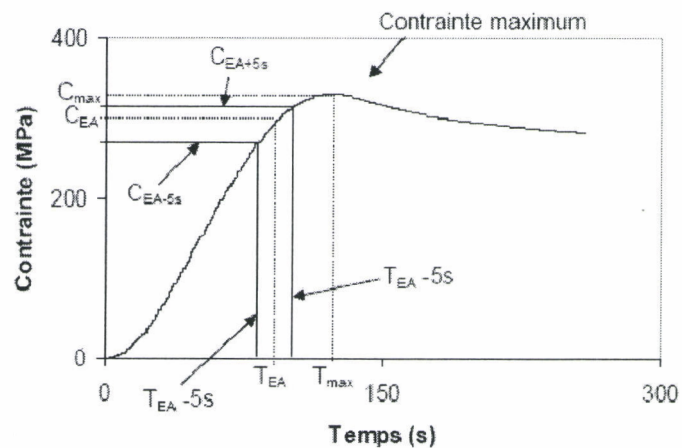
Fig. 102: Diagram of the evolution of stress as a function of time during the course of axial compression testing.
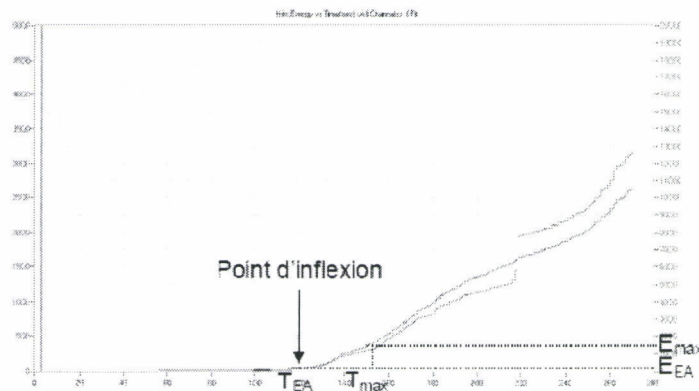
Fig. 103: Example of acoustic activity curve.

The curve in Fig. 102 passes through a maximum (coordinates C_{max} and T_{max}) and this defines the failure point of the specimen. The point of inflexion of the cumulated energy, coordinates $\{E_{EA}$ and $T_{EA}\}$, shown in Fig. 103 is chosen as a criterion for the onset of damage to the test specimen. These four coordinates are used in order to calculate the C_{max} / C_{EA} ratio. The values C_{EA}-5s and C_{EA}+5s are calculated by respectively decreasing and increasing T_{EA} by 5s and by carrying over the values onto curves similar to those shown in Fig. 102 to evaluate the synchronisation error.

The results for each test specimen, except for B415 / 38 of batch 2 (where the data does not show any maximum value) are given in Table 8. The fact that there are no values in columns C_{max}/C_{EA}-5s and C_{max}/C_{EA}-5s signifies that T_{EA}-5 or T_{EA}+5 are greater than T_{max}.

Taking the 34 analysed test specimens, it appears that acoustic emission detects the onset of damage before specimen failure at an average of 95% of maximum stress (Table 8). The cumulated energy at maximum stress is highly variable: from 1 to 12200. It is therefore difficult to define a criterion based on the energy for finding out the status of damage since this depends on the size of the test specimen, its geometry and damage location.
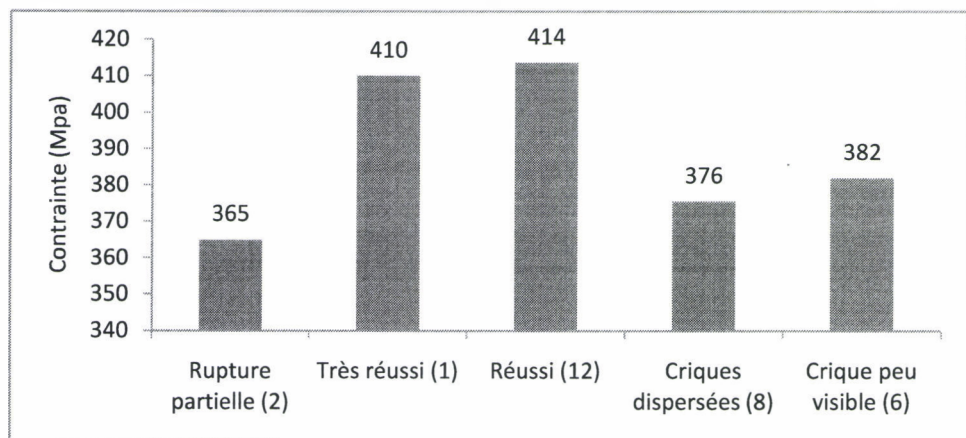
Fig. 104: Comparison between the visual classification of cracks and average failure stress (total number per visual class in brackets).

Fig. 104 shows the comparison between visual classification of cracks (classification given in Fig. 49 and Table 4) and the failure stress average per visual class. This Fig. shows the absence of a relationship between the subjective visual estimation and the severity of the mechanical damage associated with the crack. If a relationship existed, the failure stress would be very low in the case of a partial failure and would then increase up to a maximum in the case of a less visible crack.

Batch no.	Test specimen no.	Maximum stress Cmax (MPa)	Cmax/CEA (%)	Cmax/CEA -5s (%)	Cmax/CEA + 5s (%)	Cumulated energy at maximum stress Emax
1	B410 / 37	417	99.0	97.8	99.8	1
	B510 / 27	330	98.8	97.6	99.7	500
	B610 / 57	410	96.6	94.4	98.3	3150
	S1	446	96.0	94.0	97.3	16
2	B415 / 47	357	89.6	86.6	92.4	2000
	B415 / 56	384	99.5	97.4	99.7	860
3	B515 / 23	333	99.4	91.9	97.3	630
	B515 / 71	343	95.6	93.3	97.7	1750
4	B615 / 73	499	82.6	79.4	85.4	2100
	B615 / 92	354	94.1	92.4	96.3	530
	S3	407	94.8	92.9	96.3	182
5	B420 / 16	420	92.4	89.5	95.0	3100
	B420 / 38	317	94.3	91,5	96.5	160
6	B520 / 29	451	96.5	94.9	97.6	2200
	B520 / 47	461	98.9	97.4	99.8	77
	B520 / 56	492	91.3	89.0	93.1	15000
7	B620 / 29	438	92.0	90.0	93.8	3100
	B620 / 38	469	99.6	98.7	99.8	470
	B620 / 56	452	79.6	75.7	83.4	620
	S4	452	84.8	81.3	87.5	200
8	B430 / 29	348	99.1	98.0	99.7	7
	B430 / 38	348	100.0	99.1		1050
	B430 / 47	293	89.1	86.7	90.8	35
	B430 / 56	370	99.5	97.3	99.7	10
	B430 / 110	423	93.9	92.2	95.5	64
9	B530 / 16	401	98.8	97.5	99.7	1200
	B530 / 27	359				0
	B530 / 38	360	92.8	90.8	95.0	12200
	B530 / 49	348	99.1	98.3	99.7	283
	B530 / 510	407	93.9	92.1	95.8	40
10	B630 / 37	389	100.0	99.4		3
	B630 / 510	427	88.1	85.5	90.2	1370
	S5	392	98.5	97.4	99.0	5

Table 8: Relationship between Acoustic Emission and failure stress data.

11.2. Testing by Acoustic emission of a CAP10 spar during a 4 point bending test

11.2.1. Experimental protocol

11.2.1.1. 4 point bending test

The spar section on which the bend test was carried out came from a damaged wing. This spar showed cracks close to the two Acoustic Emission sensors (Fig. 105). The bending test was a 4 point test. The supports represented the anchor points at fuselage level and the load points were associated with the stress applied in flight (negative load factor). The forces applied to the structure are shown in Fig. 106. The test consisted of three increases in loading, each having a plateau.
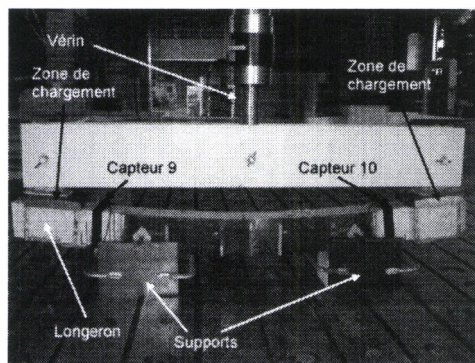
Fig. 105: 4 point bend test on a section of a CAP10 spar. Tested using Acoustic Emission (sensors 9 and10).
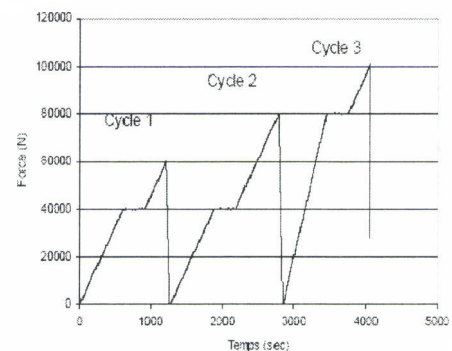
Fig. 106: Loading cycles on the spar during the 4 point bending test.

11.2.1.2. Equipment used in Acoustic Emission

The acquisition chain consisted of two sensors with integrated preamplifiers and the acquisition system SAMOS 64 (Euro Physical Acoustics). The sensors were coupled to the structure with grease and were held in position using adhesive tape. Sensor coupling was validated by the source Hsu-Nielsen (NF EN 1330-9) (2H Ø 0.5 mm lead pencil fracture) at 50 mm from each sensor. Coupling was considered to be satisfactory when the standard deviation of the different amplitudes detected by each sensor was no greater than 3 dB_{EA}. The wave velocity in the material was evaluated with the help of the source Hsu-Nielsen. The average wave velocity measured in the spar was 3500 m/s.

The settings and characteristics of the equipment are given below:

- Acquisition system- Number of channels: SAMOS – 64
- Number of channels used for the test: 2
- Type of sensors – Number: R15I – 2
- Resonance frequency (kHz):   150kHz

- System filters(kHz):   1 – 400
- Preamplifiers (standard): Integrated with Gain (dB): 40
- Acquisition threshold (dB$_{EA}$: Ref. 1 μVolt/Sensor):   45

11.2.2.   Results

Fig. 107 shows that at the very first loading, large amplitudes were detected by sensor 9; however emission became correctly stabilized at a plateau. During the second loading cycle (from 0 to 80000 N), emission resumed at around 43000 N, i.e. before reaching 60000 N (the load reached during the first cycle). This tends to show that the structure was damaged since the Kaiser effect was no longer followed. During the last cycle (from 0 to 100000 N), the first bursts were once again detected starting from 43000 N while the load previously attained was 80000 N. During the plateau at 80000 N, there was no stabilisation of emissions suggesting significant damage to the structure.

Fig. 108 shows the acoustic activity and intensity per channel. Sensor 9 detected many more events than sensor 10 particularly during the first cycle.

Fig. 109 shows perfectly the existence of three sources S1, S2 and S3. Source S1 was the most energetic.

Fig. 110 shows the appearance and the evolution of sources with time. S1 and S2 appeared on the very first loading cycle while S3 appeared during the second cycle. S1 and S3 correspond to the position of the cracks identified.

With respect to the results obtained by laboratory compression of the specimens, and taking into account the few bursts detected during the test, the criterion of failure in real time could not be determined. Furthermore it appears that the cracks were not involved in the failure in this case; instead it was due to a failure of the web - chord joint; the two zones located between the load point and the support were in fact subject to very high shear stress. Thus only the first component of the test is representative of crack evolution.
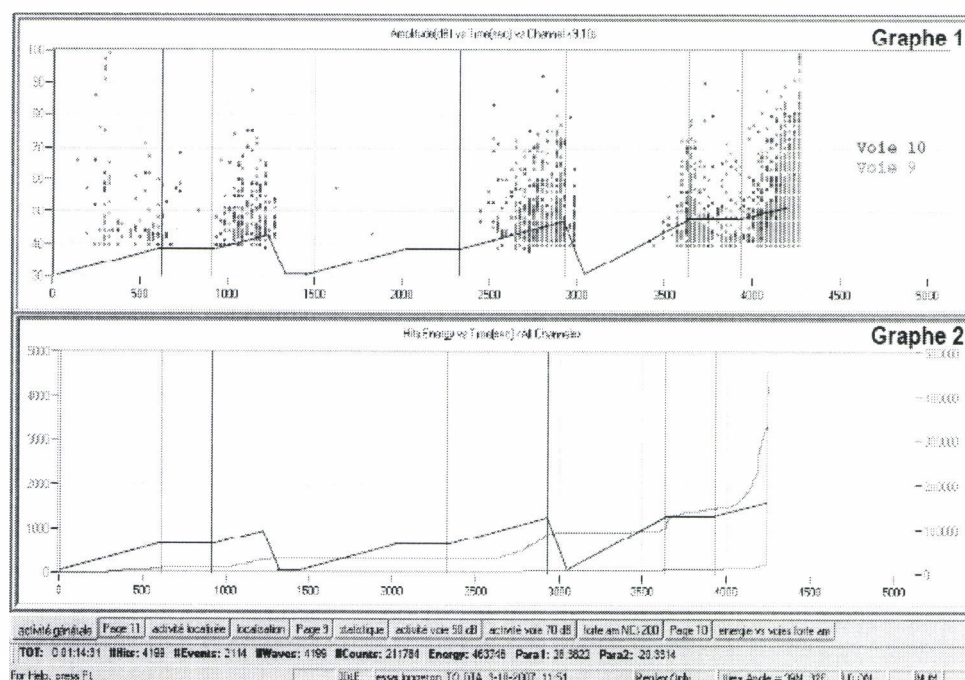
Fig. 107: General Acoustic Emission activity. Component 1: Amplitude of bursts as a function of time with display of loading cycle. Component 2: Number of bursts cumulated (in red) and cumulated energy (in green) as a function of time with display of load cycle.
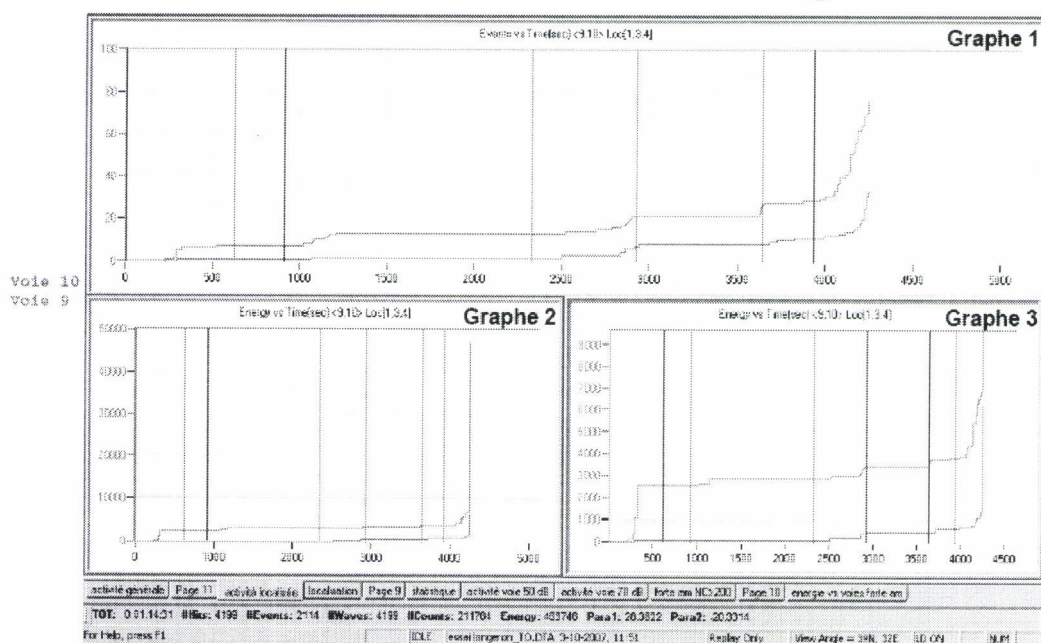
Fig. 108: Acoustic Emission activity and intensity per channel. Component 1: Number of events cumulated per channel as a function of time. Component 2: Energy cumulated per channel as a function of time. Component 3: Enlargement of component 2.

L. Brancheriau (CIRAD), J-D. Lanvin (FCBA)
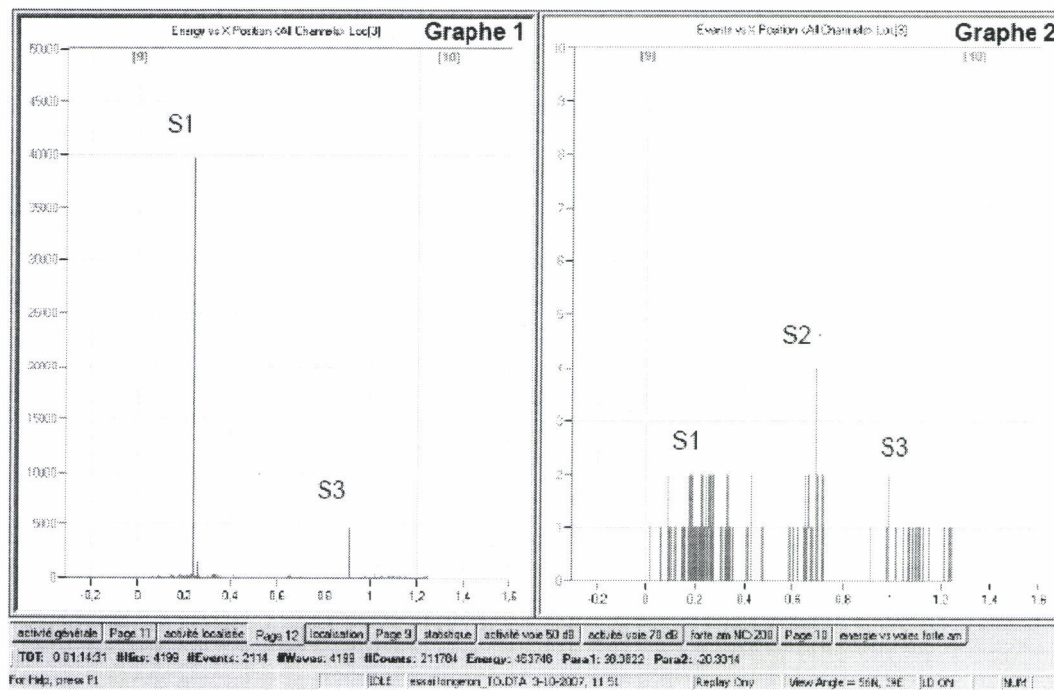
Fig. 109: Linear location of energy (1), linear location of events (2).
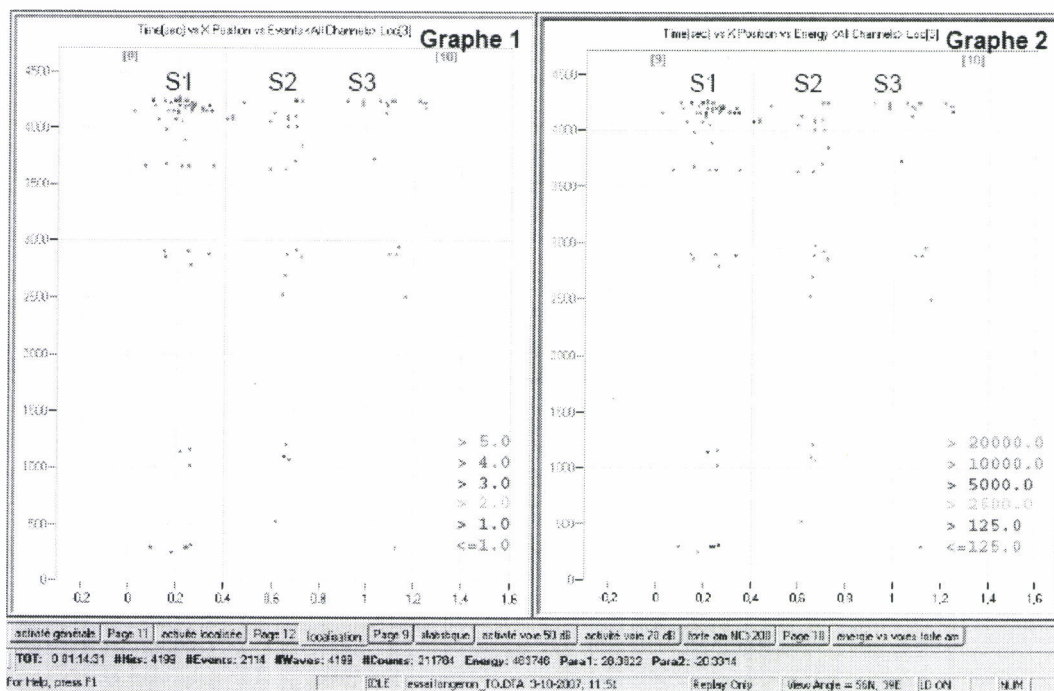
Fig. 110: Linear location of events a function of time (ordinate axis) (1), linear location of energy as a function of time (ordinate axis) (2).

11.3.   Testing by Acoustic Emission of a CAP10 wing during 4 point bend test

11.3.1.   Experimental Protocol

11.3.1.1.   4 point bending test

A rejected wing was subjected to the bend test. The drawing of a wing half is shown in Fig. 111. The load was symmetrical on the right and left wings. The load jig is shown in Fig. 112. The attachment of the wing to the jig was similar to the attachment of the wing to the fuselage.
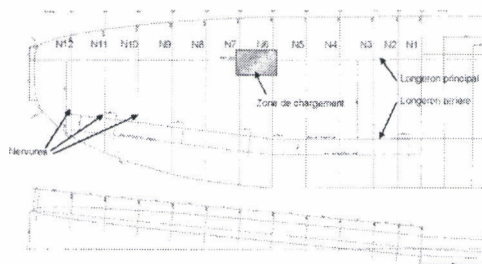
Fig. 111: Drawing of left wing of the CAP 10 and load point.
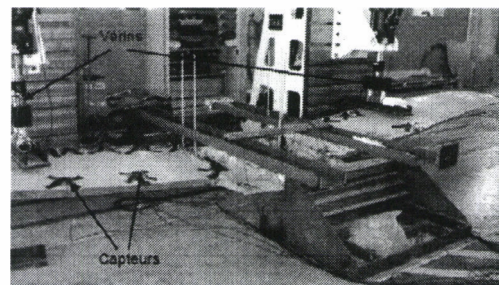
Fig. 112: Photograph of the wing in the load jig.

Two types of forces were applied on the structure. The first was the application of a static force for 10 minutes at 5400 N, i.e. 2700 N to each wing, which corresponds to an aircraft mass of 540 kg (empty weight), to provide structural stabilisation. The second was the application of an increasing load to progressively damage the structure. The complete load cycle is shown in Fig. 113.
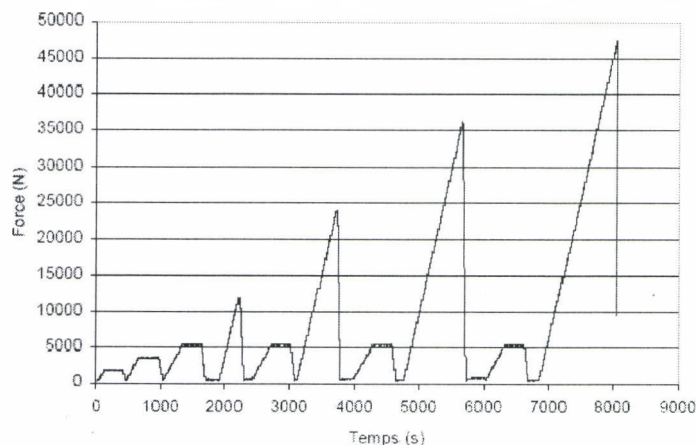
Fig. 113: Wing stress cycles during the 4 point bend test.

11.3.1.2. *Equipment used in Acoustic Emission*

SAMOS Acquisition system

The acquisition chain consisted of sensors with integrated preamplifiers and the SAMOS 64 Acquisition system (Euro Physical Acoustics). The sensors were coupled to the structure using grease and held in position using adhesive tape. Sensor coupling was validated by the source Hsu-Nielsen (NF EN 1330-9) (2H Ø 0.5 mm lead pencil fracture) at 50 mm from each sensor. The coupling was considered satisfactory when the standard deviation of the various amplitudes detected by each sensor was no greater than 3 dB_{EA}.

The sensors were placed at the rib and spar joint; at the rear limit of the spar (Fig. 114). The waves coming from the spar therefore pass through the ribs and the skin and are detected by the sensor. The wave velocity in the structure is also evaluated using the Hsu-Nielsen source. The average velocity was measured at 2500 m/s.
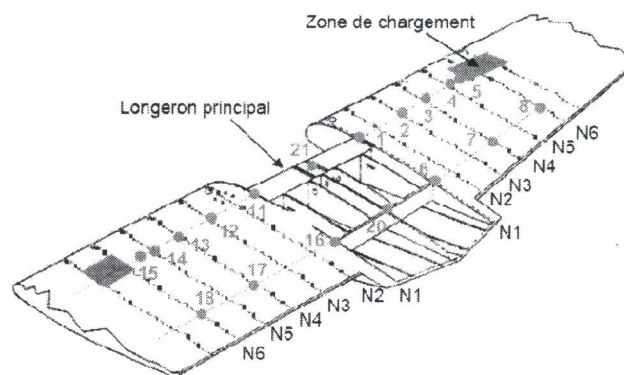
Fig. 114: Positioning of Acoustic Emission sensors on the wing.

Attenuation was measured to determine the effective radius of the sensors. The attenuation curve is shown in Fig. 115. The attenuation curve was derived using a Hsu-Nielsen source (NF EN 1330-9) (2H Ø 0.5 mm lead pencil fracture) on the wing skin. The acquisition threshold was fixed at 40 dB_{EA} bearing in mind the results obtained at CIRAD (axial compression testing on specimens). The range of a sensor is therefore 1.2 m for the Hsu-Nielsen source.
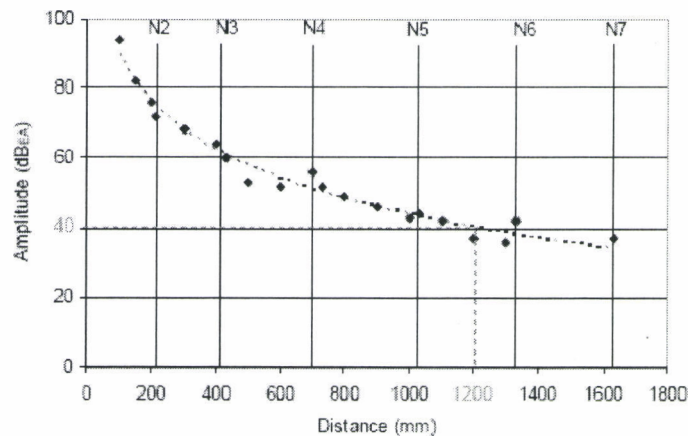
Fig. 115: Attenuation curve.

The purpose of this test was to monitor the behaviour of the two spars. Sensors were therefore positioned at the joint of the wing ribs and spars. Maximum sensor spacing was then clearly less than 900 mm, which enabled the location of events to isolate the events originating from the spars from other possible sources of damage.

The settings and characteristics of the equipment are given below:

- Acquisition system- Number of channels: SAMOS – 64
- Number of channels used for the test: 18
- Type of sensors – Number: R6I – 12

    (Sensors 1, 2, 3, 4, 6, 7, 11, 12, 13, 14, 16 and 17)

    R15I – 6

    (Sensors 5, 8, 15, 18, 20 and 21)

- Resonance frequency (kHz):   60kHz (R6I)

    150 kHz (R15I)

- System filters (kHz):   20 - 400
- Preamplifiers (standard): Integrated with Gain (dB): 40
- Acquisition threshold (dB$_{EA}$: Ref. 1 μVolt/Sensor):   40

Pocket EA Acquisition system

The aircraft wing had also been tested using another EA Acquisition system, the Pocket EA-2 (Euro Physical Acoustics). This system consisted of two acquisition channels and was portable. Two sensors had been installed and coupled to the spar with grease and held in position by adhesive (Fig. 116). The sensor coupling was validated by the Hsu-Nielsen source (NF EN 1330-9) (2H Ø 0.5 mm lead pencil fracture) at 50 mm from each sensor. The coupling was

considered satisfactory when the standard deviation of the different amplitudes detected by each sensor was no greater than 3 dB_{EA}.
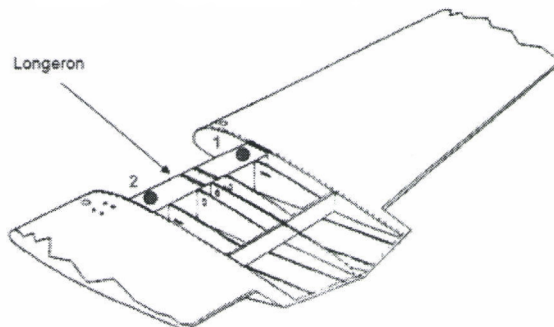
Fig. 116: Positioning of Acoustic Emission sensors (Pocket EA).

The settings and characteristics of the equipment are given below:

- Acquisition system- Number of channels: Pocket EA-2 - 2
- Number of channels used for the test: 2
- Type of sensors – Number: R15α - 2
- Resonance frequency (kHz):   150kHz
- System filters (kHz):   20 - 300
- Preamplifiers (standard): Integrated to the system with Gain (dB): 26
- Acquisition threshold (dB_{EA}: Ref. 1 μVolt/Sensor):   40

11.3.2.   *Results*

The EA data recorded during the static cycles and the data recorded during the damage cycles was dissociated for better real time analysis of the results.

11.3.2.1.   *SAMOS acquisition system*

Results obtained during the static tests

The loading cycle consisted of six load plateaus (Fig. 113). The first three were carried out with the sole aim of checking the behaviour of the structure under small loads. The next three plateaus at 5400 N were preceded by a load increase greater than 5400 N, with the aim of achieving structural damage.

Fig. 117: General activity during static tests (SAMOS). Component 1: Amplitude of the bursts as a function of time with visualisation of the load cycle. The colour scale represents the number of bursts cumulated. Component 2: Number of bursts cumulated (in red) and energy cumulated (in green) as a function of time with visualisation of the load cycle.

Fig. 117 shows that the bursts were detected naturally while ascending to the second and third plateau, with emissions stabilising quite rapidly at plateaus. At plateau 4, preceded by a load of 12000 N, only a few small amplitude bursts were detected. Despite a load increase to 24000 N before plateau 5 and 36000 N before plateau 6, larger amplitude bursts were nevertheless detected during these phases, refuting the Kaiser effect and indicating the existence of structural damage.

Results obtained during the damage tests

Fig. 118 shows that bursts were detected during all loading phases. The first bursts of very large amplitudes appeared from the second load onwards. The Kaiser effect stipulates that no bursts should be detected before reaching the maximum force previously applied. This Kaiser effect was not fully respected during the third and last loading as the first bursts were detected at 22000 N (previous plateau: 24000 N) and 33000 N (previous plateau: 36000 N) respectively. The fact that the Kaiser effect was not followed shows that the structure was damaged.

Fig. 119 shows the existence of five sources S1, S2, S3, S4 and S5 localised during the test. For the right wing, the main source, S1, was located at the level of rib 1. The other sources are all located on the left wing. Sources S2, S3, S4 and S5 were located on ribs N1, N2, N4 and N5 respectively (close to the application point of the force).
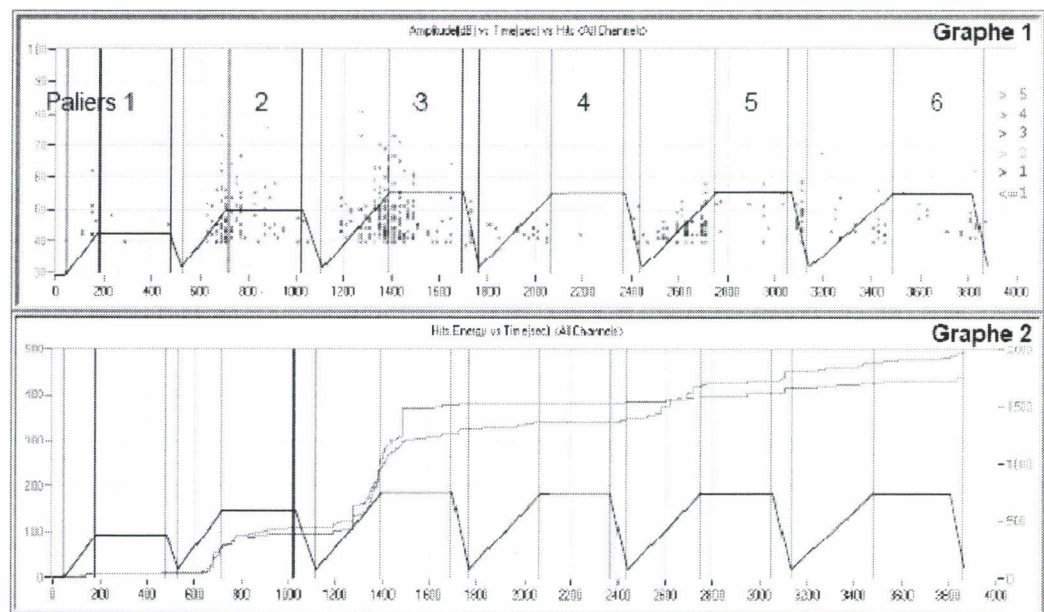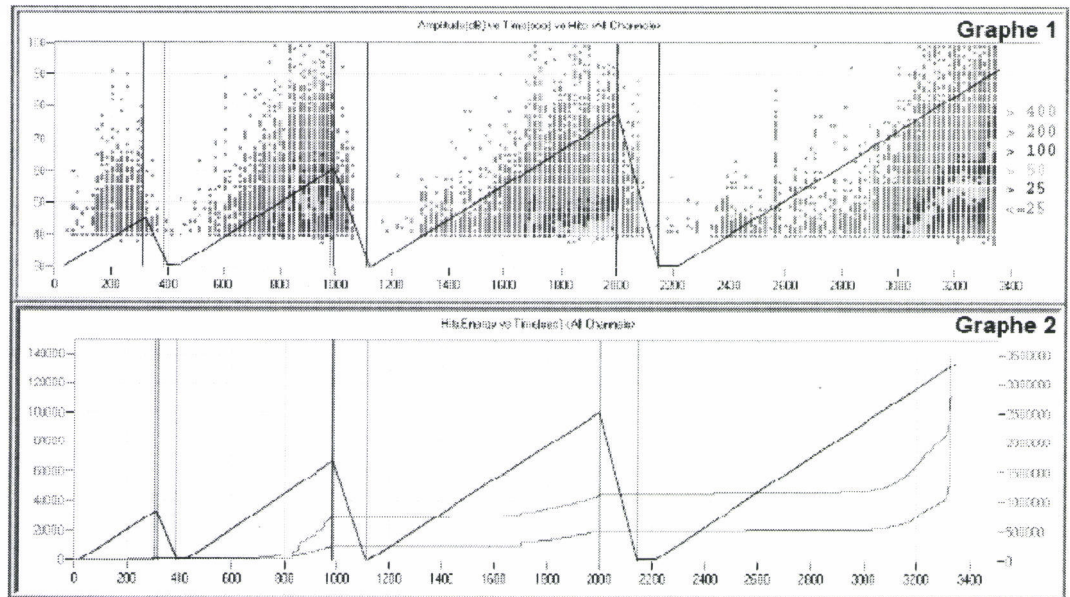
Fig. 118: General activity during the damage test (SAMOS). Component 1: Amplitude of bursts as a function of time with display of the loading cycle. The colour scale represents the density of bursts. Component 2: Number of bursts cumulated (in red) and energy cumulated (in green) as a function of time with display of the loading cycle.
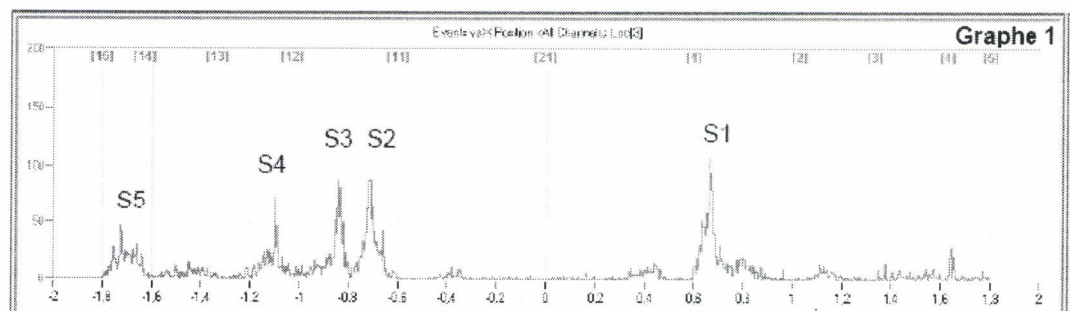
Fig. 119: Linear location of events on the spar during the damage tests (SAMOS).

Analysis of sources helps to characterise the damage pattern as a function of force. To obtain the Felicity curves, the parameter of cylinder displacement was chosen, as the force signal was very noisy (Fig. 120, Fig. 121, Fig. 122, Fig. 123 and Fig. 124).
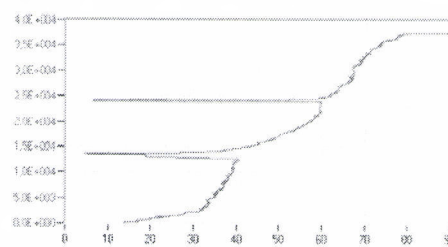
Fig. 120: Energy of events of source S1 as a function of displacement (Felicity curve).
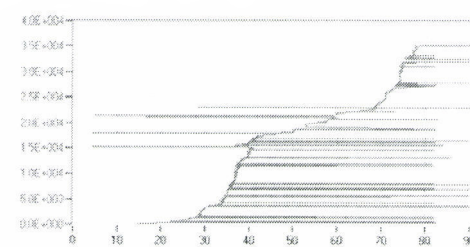
Fig. 121: Felicity curve of source S2.
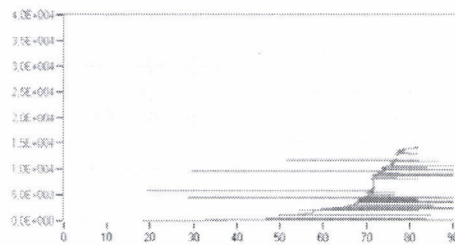
Fig. 122: Felicity curve of source S3.
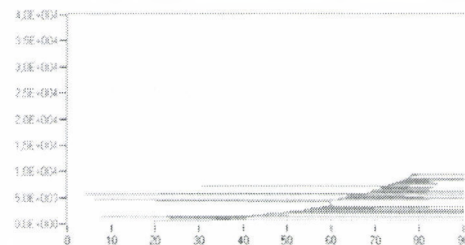
Fig. 123: Felicity curve of source S4.
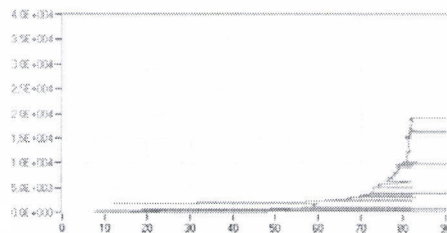
Fig. 124: Felicity curve of source S5.

In the S1 case (Fig. 120), emissivity was reached very rapidly with a point of inflexion at approximately 30 mm of displacement, equivalent to a force of approximately 17000 N. The curve then had a linear tendency. It did not result in failure.

The S2 Felicity curve (Fig. 121) shows several points of inflexion at around 25 mm, 40 mm and 65 mm, equivalent to forces of 13000 N, 23000 N and 39000 N respectively. The curve first increased rapidly, followed by a linear tendency. S2 did not result in failure.

The growth of the S3 Felicity curve (Fig. 122) started late (final cycle). It had a point of inflexion at around 55 mm displacement equivalent to a force of approximately 33000 N. The curve had an exponential tendency.

The S4 Felicity curve (Fig. 123) had a point of inflexion at around 30 mm displacement, equivalent to a force of approximately 17000 N.

The S5 Felicity curve (Fig. 124) had a point of inflexion at around 65 mm of cylinder displacement. The curve had an exponential tendency and was a precursor of failure.

11.3.2.2. *Pocket EA Acquisition system*

Unlike what was done earlier, data originating from static forces and from damage cycles were recorded in the same file.

Fig. 125 gives real time results that are similar to the results previously obtained: burst detection mainly during loading to 12000 N, 24000 N, 36000 N and until failure. Bursts were also detected during plateaus following loading to 24000 N and 36000 N.

Fig. 126 also corroborates the results obtained previously by showing that sensor 1 (right wing) detected the bursts of highest amplitude up to 24000 N then

from the time of load increase to 36000 N, it is sensor 2 (left wing) which detects the highest energy bursts. Early detection of very high energy bursts during the second or third damage cycle could be used as a criterion for damage.

The final loading was not recorded to its completion because of memory overflow in the Pocket EA.
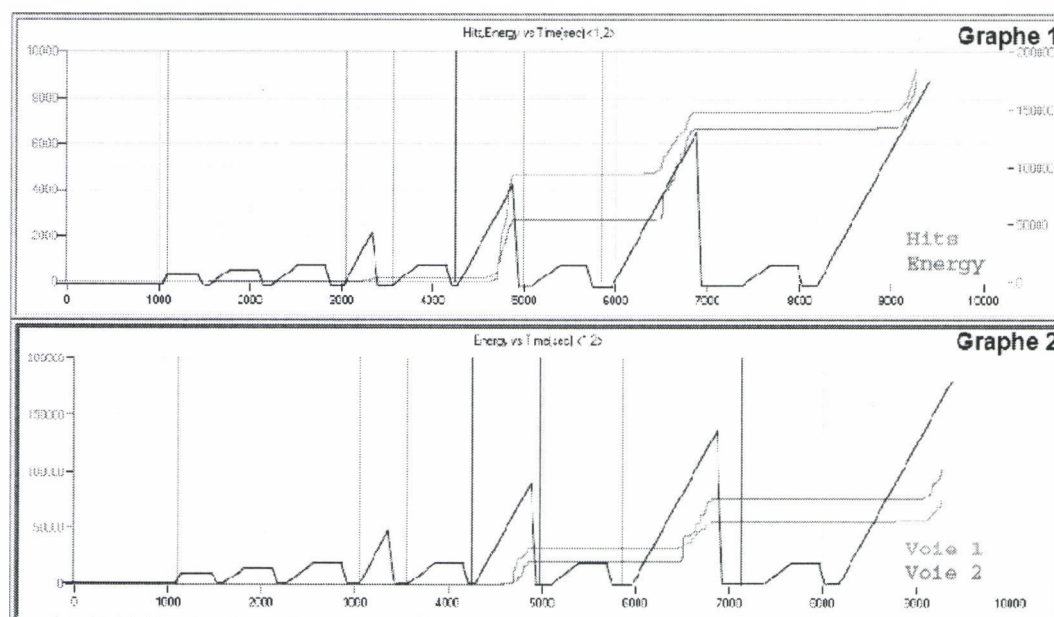
Fig. 125: General activity (Pocket EA). Component 1: Amplitude of bursts as a function of time with display of the load cycle. The colour scale represents the number of bursts cumulated. Component 2: Number of bursts cumulated (in red) and energy cumulated (in green) as a function of time with display of the load cycle.


Fig. 126: Reception of bursts per channel (Pocket EA). Component 1: Amplitude of bursts as a function of time with display of the load cycle. Component 2: Energy of bursts as a function of time with display of the load cycle.

12. Conclusions

12.1. Types of cracks and the inspection problem

Observations made on the spars of the CAP10 have helped to define the inspection problem. The cracks are located on both the upper and lower surfaces of the wing. There are zones which favour crack formation. These zones are located close to the wing/fus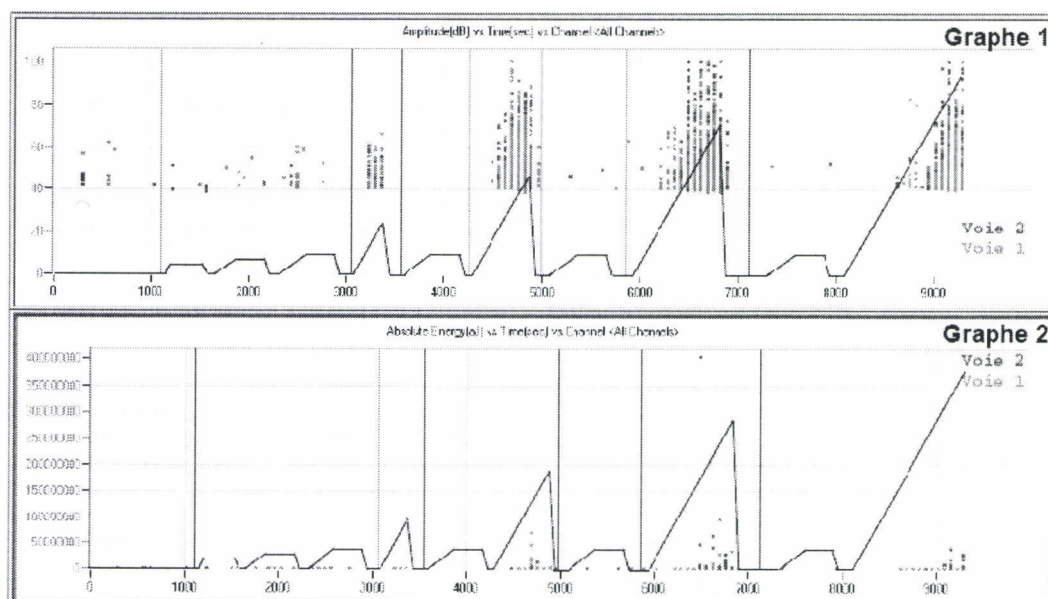elage joint and extend to the landing gear attachments: i.e. 0.5 m approximately. The whole spar must however lend itself to inspection. All aircraft are inspected periodically. These inspections are mainly visual and external. Other checks like "major checks" or "general overhauls" are more in-depth and require dismantling of some elements of the aircraft. Opening up the wing skin for inspection is a particularly challenging operation. Unintentional nicks induced by this operation will develop into cracks. The examination however remains visual and subjective. Certain parts of the aircraft are more difficult to access and hence more difficult to inspect. Cracks can also appear under the chords of the rib and spar joints and are impossible to detect visually.

Inspection is first and foremost necessary to ensure airworthiness testing for all aircraft made of wood. The inspection of in-service aircraft implies the promotion of inspection methods capable of investigating structural elements which lack direct access (presence of a skin component). Direct access testing of the structure should be considered in case indirect access testing is not possible. The aim of this inspection is firstly to detect the existence of cracks in spars of aircraft of type CAP10: do cracks exist? Where are they located? The size of the crack is of secondary importance (surface area as well as depth).

12.2. Selected inspection methods

Certain selected methods are complementary; the detection power of the inspection protocol used can be increased by combining several of these methods:

Image analysis – Surface inspection with direct access. This is the only optical method considered since application of mechanical stress to the inspected object is not required. This method is similar to visual examination; it is however not subjective.

Thermal infrared – Surface inspection with direct access (the surface must be previously heated).

X-rays – Deep inspection without direct access.

Ultrasound – Deep inspection with direct access.

Acoustic Emission– Passive listening and location without direct access – In-service testing.

12.3. Image analysis on test specimens

The specimens were flat scanned (12 points per mm), with lighting directed perpendicular to the specimen. A very simple image processing method was applied to all the specimens to check whether cracks could be highlighted. In

many cases, the natural texture of the wood completely masked the crack, or the direction of lighting did not allow its detection. The use of this method for inspection would therefore be possible only if the testing was performed under several angles of incidence of the light, if the image deformation obtained due to the optics of the imaging system and the different angles of incidence could be corrected by generating sufficient resolution and if the variations in the natural texture of wood could be removed by appropriate image filtering.

12.4. Thermal infrared on test specimens

The tests consisted in thermally exciting the surface of the specimen on which a camera is focussed. Different techniques and processes were used to detect the defect: "flash" excitation, step excitation and oblique excitation. Tests were also performed after dampening the specimen, with the presence of water modifying the thermal properties of wood making it more homogeneous. Irrespective of the type of excitation or the method used, the crack could not be detected. This type of defect does not seem to bring about any significant modification in the thermo – physical properties of wood for its detection by thermal infrared.

12.5. X-rays on test specimens

12.5.1. Transmission imagery (35 kV, 400 μA, 20 μm)

In transmission, cracks are visible as darker zones which indicate the existence of material that is denser than its surroundings. Cracks are sometimes visible in transmission but contrast depends significantly on the orientation of the beam with respect to the fissure, and it would be necessary to take several views at different inclinations to ensure detection (the time for one shot is one minute). In fact as regards the detection of compression cracks, which are plane defects, sensitivity of X-ray imagery to this type of defect depends largely on the orientation of the crack. For the crack to be detected, it must be oriented along the incident beam. Further, the natural heterogeneity of wood can give very high contrasts on the image, again based on their orientation with respect to the beam.

12.5.2. Compton Diffusion (120 kV, 230 μA, 20 μm)

The advantage when compared with transmission testing is that thickness variations do not come into play. The geometric configuration of the test requires access to only one side of the component, which is more suitable for inspection. The signal given by wood is very weak. The sensitivity required to detect the existence of a crack has not been achieved. No significant fluctuations on the number of photons received can be seen at the crack location.

A collimator with sharper output could define a finer measuring volume but as at present the power available on the laboratory tube does not provide an adequate signal. A more powerful tube is required. A fairly significant variation of the number of photons was also found on several successive scans of the same component. This variation could be due to the tube itself (variation of the focus position for example since collimator setting in front of the tube is very critical), or the sensor. There is therefore a need (1) to augment the signal to achieve increased sensitivity to smaller variations in the number of photons, (2) to

stabilise the measurement so that good repeatability can be achieved.

12.6. Ultrasound

12.6.1. Normal reflection by coupling with water on test specimens

In B-Scan mapping at 1 MHz, compression cracks could be detected by the existence of anomalies (acoustic impedance failure). For each specimen, the crack depth was recorded visually on the side faces (from digital images). Analysis of B-Scan images obtained under normal reflection helped to estimate the depth of cracks. The depths recorded in B-Scan imagery were consistent with the depths directly measured on the specimens.

12.6.2. Variable incidence by coupling with water on spar element

The spar element has been tested under normal incidence and oblique incidence of +20° and -20° with respect to the specimen surface. The transducer used operates at 1 MHz. Under oblique incidence as under normal incidence, the presence of the crack results in a variation of the B-Scan image. An optimised scan could be obtained through successive scans under various angles of incidence.

In the present state of the laboratory study, ultrasound analysis helps to highlight important elements in the non-destructive testing of spar-type composite structures. Without being in a position to draw final conclusions or to recommend a more industrial application (prototyping), the ultrasound analysis carried out has demonstrated its use in the detection of compression cracks. At 1 MHz, in B-Scan imagery (impedance contrast image), underwater type ultrasound detection appears possible.

A more complete and systematic approach to ultrasound compression crack detection should perhaps be considered; this would incorporate significant studies at the wood structure level as well as into bonded laminated structures, and include tests to be carried out in an industrial context. This preliminary work would have to include more in-depth studies in order to seriously consider using an ultrasound protocol industrially. At the present state of the art, it would be dangerous to develop an industrial prototype or even tests based on these results alone whether they are academic or industrial. This danger arises from the adaptability as well as the reproducibility of the protocol, and the ultimate risk of an inaccurate check.

12.6.3. Ultrasound testing with elastomer couplant on test specimens

The acquisition chain is integrated to an industrial portable system Pocket AU. The transducers are fitted with a couplant made of elastomer material. The appropriate frequency range for wood and the couplant lies between 200 kHz and 400 kHz. The natural heterogeneity of wood (knots, density variation etc.) if reflected in the variations of the A-Scan signal for the same test specimen (based

on the inspected zone). Signal attenuation is not constant for each specimen, which imposes different gain settings for each reference. It therefore seems difficult to define a standard gauge block for this study. The B-Scan maps obtained all have different patterns making interpretation difficult. Out of 16 tests, 4 detections were possible and no detection was made on the reference specimen. None of the successful detections related to small cracks. One large crack was not detected. The results obtained do not grant full validation for the method with respect to problems of interpretation of the ultrasound signal associated to the heterogeneity of wood.

However, it would certainly be interesting to carry out B-scan mapping on the same wood specimen for three mechanical conditions: non-compressed, compressed without damage and compressed with damage. In fact, by comparing these 3 maps, an evaluation could be made on the influence of the compression operation (material history) on ultrasound signal on the one hand, and on the other, the possibility of testing these assemblies even without absolute references.

12.6.4. Ultrasound testing of a CAP10 wing during 4 point bend test

Ultrasound testing of a static test on a CAP10 wing was carried out in addition to testing through acoustic emission. The ultrasound acquisition chain was made up of sensors with integrated preamplifiers (used in acoustic emission) and a multi-channel acquisition system (SAMOS - 64). The signals were generated by an ARB14150 card (2 sources). The tests were performed periodically during the static test after each relaxation of the structure at rest.

The evolution of the propagation time between the transmitter and the receivers, coupled on the ribs, after each loading did not show any significant variation during the test. An analysis of parameters extracted during testing was however able to identify the energy of the waveforms as a distinguishing parameter between the different ultrasound shots. It was however impossible to determine the location of the wing failure. The coupling of the ultrasound transmitters - receivers on the wing skin would enable the detection of a structural modification of the skin but not of the spar.

12.7. Acoustic Emission

12.7.1. Acoustic Emission on test specimens

Thirty four specimens were tested using Acoustic Emission (PCI-2 card). Acoustic activity as well as linear locations were performed and provided good results when the damage was located between the two sensors. It appears that the Acoustic Emission detected the start of damage before specimen failure at an average of 95% of the maximum stress based on the point of inflexion of the acoustic activity curve. The cumulated energy at maximum stress varied greatly. It was therefore difficult to define an energy based criterion to determine the damage state. A test without adhesive joint and with a failure of the glued joint would also be interesting to check the emissivity of the adhesive joint and to characterise the damage.

12.7.2.   *Acoustic Emission on a piece of the CAP10 spar*

In the light of the results obtained by laboratory compression of the specimens, and taking into account the very few bursts detected during the test, the criterion for failure in real time could not be determined. Furthermore it appears that the cracks were not involved in the failure in this case but that is was due to a failure of the web - chord joint; the two zones located between the load point and the support are in fact subject to high shear stress.

12.7.3.   *Acoustic Emission on CAP10 wing*

A CAP 10 wing was subjected to a load test. Increasing load cycles were interspersed with reduced load cycles to initiate damage. Static load cycles were applied to detect any existing damage even at reduced load. The purpose of these tests was to check the feasibility of Acoustic Emission for detecting damage early and to characterise the failure process of the structure.

Testing the wing by Acoustic Emission highlighted the existence of five sources. These sources were all positioned along the main spar. Only one of these sources was located on the right wing, close to the wing/fuselage joint. On the left wing, one of the sources was also located close to the wing/fuselage joint. These two sources appeared very rapidly on the initial load cycle at 12000 N (25% of the breaking load). It is very strongly advised to inspect these two areas of the fuselage/wing joint. The other sources appeared later and corresponded to a failure of the spar and the skin, failure which does not seem to be the result of in-service cracks.

Static load cycles at low loading, 5400 N (11% of the breaking load), particularly after loading to 24000 N (51% of the breaking load), helped to detect existing damage to the zones of the fuselage/wing joint and the location of the spar failure.

During the same series of tests on the wing, another portable and self contained Pocket EA acquisition system, was connected to two sensors independent from those used previously. The results obtained with the Pocket EA did not enable accurate location of the damage. On the other hand, by positioning the sensors close to the wing/fuselage joint, it was possible to determine a criterion for damage. The configuration parameters of the Pocket EA can be optimised for long duration acquisitions, by only detecting the signals that correspond to the criteria for damage.

13. Recommendations

It must be remembered that the major component of damages on mechanical parts or structures that occur in-service are failures due to fatigue and they originate from the cyclic loading of critical zones where stresses are concentrated. In these zones, progressive damage to the material appears in the form of micro-fissures, which appear more or less rapidly, depending on the nature of the material and the size of the load applied. After this crack initiation period, one or more of these fissures will get propagated throughout the entire thickness of the component until sudden failure occurs.

Inspection is therefore inevitable irrespective of the material used to manufacture a spar (wood or composite material). The appearance of cracks in the spar represents a stage in the normal aging process of the spar.

From reference to the conclusions obtained for each inspection method tested:

Image analysis – this method could find application. For a visual examination, this method has the advantage of not being subjective. Image analysis can at best be as efficient as a well-informed human eye. Cracks may appear in areas that are inaccessible to visual inspection. The relationship between the visual observation of the cracks (subjectively classified by order of importance) and tensile stress could not be proved. It is dangerous to affirm through visual observation that the existence of a crack will provoke the imminent failure of the spar.

Thermal infrared – The thermal infrared tests carried out did not prove the effectiveness of this method for crack detection.

X-rays – The effectiveness of this method could not be proved with certainty in the laboratory. Using this method for crack detection does not seem conceivable on account of the constraints involved during experimental implementation.

Ultrasound – Laboratory tests have shown the importance of this method for crack detection. However, the tests performed using industrial testing equipment showed that considerable research and development remains to be done.

Acoustic Emission– The application of acoustic emission is conceivable for determining the level of damage to the spar. Based on the chosen configuration, this method, through passive listening, can detect the appearance of damage and locate it throughout the in-service life of the aircraft.

The inspection process requires the use of several non-destructive testing methods for effectiveness. Opening up the wing skin is a very delicate operation and can lead to crack formation. The opening operation must be performed at the end of the testing process. It would then be judicious to design the inspection process by the combined use of a load factor recording accelerometer, a record of the total weight of the equipment before each take-off and a real time embedded testing device employing acoustic emission to assess the level of structural damage. During the course of the in-service life of the aircraft and based on the data collected by all the embedded testing devices, the decision to open the wing skin can be taken during a routine overhaul. A visual inspection can then be carried out, with its conclusions being validated by ultrasound inspection to accurately locate the defective area in case this zone is accessible. The spar can then either be repaired or the whole wing replaced.

14. Contact information of the authors

Loïc Brancheriau

CIRAD, UPR 40, Production and valorisation des bois tropicaux

TA B-40/16, Avenue Agropolis

34398 Montpellier Cedex 5

loic.brancheriau@cirad.fr

Jean Denis Lanvin

Forêt Cellulose Bois-construction Ameublement

Allée de Boutaut, BP 227

33028 Bordeaux Cedex

Jean-Denis.Lanvin@fcba.fr

15. Bibliography

- Bariska, M., Kucera, L.J. (1985) "On the fracture morphology in wood. Component 2", Wood Science and Technology, Vol. 19, pp. 19-34.

- Bodner, J., Schlag, M.G., Grüll, G., (1997) "Fracture initiation and progress in wood specimens stressed in tension; component II", Holzforschung, Vol. 51, pp. 571-576.

- Bray, DE., McBride, D. (1992), "Nondestructive testing techniques", John Wiley & Sons (Ed.), pp. 15-24.

- Bruce Hoadley R. (2000), "Understanding Wood: A Craftsman's Guide to Wood Technology", Taunton (Ed.), pp. 99-100.

- Brun, G. (2006), " Quand la lumière rencontre la matière; intérêt de l'optique and la photonique pour l'instrumentation and le contrôle", Contrôles Essais Mesures, Vol.16, pp. 121-124.

- Choi, D., Thorpe, J.L., Côté, W.A., Hanna, R.B., (1996) " Quantification of compression failure propagation in wood using digital image pattern recognition", Forest Products Journal, Vol.46, pp.87-93.

- Clorius, C.O., Pedersen, M.U., Hoffmeyer, P., Damkilde, L. (2000), " Compressive fatigue in wood", Wood Science and Technology, Vol. 34, pp. 21-37.

- Diederichs, R., Ginzel, E., Grosse, C. (AE) (2006), " Introduction to Optical Holographic NDT", Nondestructive Testing Encyclopedia, http://www.ndt.net/article/az/other/hndt.htm.

- Ellis, S., Steiner, P. (2002), " The behaviour of five wood species in compression", IAWA Journal, Vol. 23 (2), pp. 201-211.

- Ettemeyer, A. (2004), "Material and component validation by speckle interferometry and correlation methods", 16th WCNDT 2004 - World Conference on NDT, Aug 30 - Sep 3, Montreal, Canada. http://www.ndt.net/.

- Fournier, N., Brousset, C. (2006), "ShapeView - A Portable Shape Measurement System", 9th European Conference on No-Destructive Testing, 25-29 sept., Berlin, Allemagne. http://www.ndt.net/.

- Gong, M., Smith, I. (2004), "Effect of load type on failure mechanisms of spruce in compression parallel to grain", Wood Sci Technol, Vol.37, pp. 435-445.

- Guitard, D. (1987), "Mécanique du matériau bois and composites", Cépaduès-Editions, pp. 36-61.

- Hellier, CJ. (2001), "Handbook of nondestructive evaluation", McGraw – Hill (Ed.), p. 603.

- Huber, R., Berger, R., (2006), "Shearography as an Industrial Application Including 3D Result Mapping", 9th European Conference on No-Destructive Testing, 25-29 sept., Berlin. http://www.ndt.net/.

– Kerguignas, M., Caignaert, G. (1977), "Résistance des matériaux", Dunod, pp. 225-271.

– Klinka, JM. (1988), "Conception de structures en composite bois - carbone", Association Aéronautique and Astronautique de France, Colloque matériaux, structures and aviation légère.

– Kollmann, FFP., Côté, WA. (1968), "Principles of wood science and technology", Springer-Verlag, pp. 324-363.

– Kouzoubachian C. (2006), "Les principales méthodes utilisées en END, intérêts dans l'industrie", Contrôles – Essais - Mesures, Hors série n°1, pp. 15-19.

– Pluvinage, G. (1992), "La rupture du bois and de ses composites", Cépaduès-Editions, pp. 33-62.

– Racher, P. and al. (1996), "Structures en bois aux états limites", SEDIBOIS/Union Nationale Française de charpente, menuiserie, parquets, Chapitre III-1-1.

– Shull, PJ. (2002), "Nondestructive evaluation – Theory, techniques, and applications", Marcel Dekker (Ed.), p. 848.

– Sonderegger, W., Niemz, P. (2004), "The influence of compression failure on the bending, impact bending and tensile strength of spruce wood and the evaluation of no-destructive methods for early detection", Holz Roh Werkst, Vol. 62, pp. 335-342.

– USDA (1961), "Detection of compression failures in wood", USDA, Report N°1588, p. 13.

– Vallat, P. (1945), "Résistance des matériaux appliqués à l'aviation", Ménard Editeurs, pp. 297-310.

જ⊷૭